FROM VAN DER WAALS TO COULOMBIC HETEROSTRUCTURES: UNDERSTANDING CHARGE TRANSFER IN 2D MATERIALS

Adam Haas Woomer

A dissertation submitted to the faculty at the University of North Carolina at Chapel Hill in partial fulfillment of the requirements for the degree of Doctor of Philosophy in the Department of Chemistry.

Chapel Hill
2018

Approved by:

Scott C. Warren

James F. Cahoon

Wei You

Joanna M. Atkin

Theo Dingemans

ABSTRACT

Adam Haas Woomer: From van der Waals to Coulombic Heterostructures: Understanding Charge Transfer in 2D Materials
(Under the direction of Scott C. Warren)

Innovations in semiconductor technologies, such as transistors, photovoltaics, and light-emitting diodes, require materials with highly designed properties. Zero-dimensional quantum dots and one-dimensional conjugated polymers are ideal building blocks for engineered three-dimensional materials because of their size-dependent quantum-confined optoelectronic properties, however, two-dimensional materials have been largely unexplored. Here I show that reassembled films of 2D semiconductors retain their quantum-confined properties due to turbostratic disorder and interlayer contaminants, yet are still electrically conductive. I designed uniaxially pressure and temperature-dependent van der Pauw conductivity measurements to determine that charge transport proceeds *via* hopping, with an activation energy expected for nanoparticle systems. In this manner, we can design 3D materials with virtually any optoelectronic propertie with the appropriate choice of 2D material and thickness.

I next introduce a new class of materials, called Coulombic heterostructures. As opposed to the familiar van der Waals heterostructures, in which van der Waals forces dominate the interlayer space of stacked 2D materials, Coulombic heterostructures exhibit massive charge transfer and Coulombic forces between layers. These materials take advantage of the ultra-low work function and anionic electron gas of electrenes to form quasi-bonds between adjacent flakes. With interlayer distances smaller than van der Waals bonds yet larger than ionic and

covalent bonds, Coloumbic heterostructures fall within the van der Waals gap, a largely unexplored region of materials. I then highlight the exciting new properties that can result from the assembly of Coulombic heterostructures, including superlubricity, defect free doping, formation of electron-donor adducts, and tuning of intercalation voltages for battery applications.

To my friends and family, I don’t know where I would be without your support and I couldn’t have done this without you.

ACKNOWLEDGEMENTS

First, I would like to thank Professor Scott Warren for his guidance and support during my time in his laboratory. He has been a role model for the kind scientist I would like to be as I move forward in my career, and has taught me to think critically and question everything.

I would also like to thank Dan Druffel and Tyler Farnsworth, who I worked the closest with during this journey. Your stimulating discussions, aid with experiments, and coffee trips have kept me motivated and excited about our research. I am looking forward to reading about the contributions to science that each of you will produce in the future. After all of our experiences together, I can confidently say that your future colleagues and collaborators will be lucky to be working with such great scientists.

I am so proud to have been a member of the Warren lab, and I couldn't have imagined a greater group to have been a part of. From cake making parties to board games to eating out on Franklin Street, thank you to everyone for making graduate school a little less stressful and for putting up with my shenanigans along the way. I hope that I have been able to make you smile, laugh, or even feel a little less overwhelmed, as you have done for me every day.

I would also like thank to my wife, Claire, who has continued to believe in me, unfalteringly, since the first day we arrived in North Carolina. She inspires me to be a better man and I can't imagine anyone more supportive and understanding to be with. I'm looking forward to our future lives together and having you by my side for every adventure.

TABLE OF CONTENTS

LIST OF TABLES

LIST OF FIGURES

LIST OF ABBREVIATIONS

1D	One-dimensional
2D	Two-dimensional
2DM(s)	Two-dimensional Material(s)
3D	Three dimensional
AFM	Atomic force microscopy
BFGS	Broyden-Fletcher-Goldfarb-Shanno
CASTEP	Cambridge Serial Total Energy Package
CCD	Charge-coupled device
CVD	Chemical Vapor Deposition
DFT	Density Functional Theory
DFT-D	Density Functional Theory with Dispersion forces
DMPU	1,3-dimethyl-3,4,5,6-tetrahydro-2(1H)-pyrimidinone
DP	Diffraction pattern
e-BN	electrene-boron nitride heterostructure
e-C	electrene-graphene heterostructure
e-P	electrene-phosphorene heterostructure
e-ZrS_2	electrene-zirconium disulfide heterostructure
EBE	Exciton binding energy
EDD	Electron density difference
EDFT	Ensemble density functional theory
FETT	Field effect tunneling transistor
FFT	Fast fourier transform

FT-IR	Fourier transform-infrared
GGA	Generalized-gradient approximation
hBN	hexagonal Boron Nitride
HF	Hartree-fock
HRTEM	high-resolution transmission electron microscopy
HSE	Heyd-Scuseria-Ernzerhof
ICP-MS	Inductively coupled plasma-mass spectroscopy
IPA	Isopropanol
JEMS	Java electron microscopy simulation
LB	Langmuir-Blodgett
LDA	Local density approximation
nBuLi	n-butyllithium
NMP	*N*-methyl-2-pyrrolidone
PBE	Perdew-Burke-Ernzerhof
PL	Photoluminescence
PTFE	Polytetrafluoroethylene
PVDF	Polyvinylidene Fluoride
RCF	Rotational centrifugal force
RPM	Rotations per minute
SDC	Small digital controller
SIMS	Secondary ion mass spectroscopy
SEM	Scanning electron microsopy
TEM	Transmission electron microscopy

TMD	Transition Metal Dichalcogenides
UV-vis-nIR	Ultraviolet-visible-near infrared
vdP	van der Pauw
vdW	van der Waals
VF	Vacuum filtered
XPS	X-ray photoelectron spectroscopy
XRD	X-ray diffraction

CHAPTER ONE – INTRODUCTION

1.1 Engineered 3D materials with quantum confined properties

Thin and thick films with tunable optoelectronic properties are essential for the design of many technologies, including photovoltaics, transistors, and light emitting diodes. As such, there have been investigations into designing three-dimensional materials from zero-dimensional and one-dimensional building blocks, that retain their highly tunable quantum-confined properties. Quantum dots[1] have attracted broad interest because of their size-dependent electronic structure and controllable physical properties[2-5]. Colloidal quantum dots can be deposited from solution as films[6-7] that retain their quantum-confined optical properties despite electronic coupling and effective charge transport between nanoparticles[8-10]. These materials have been described as 'confined-yet-coupled' systems, in which the electrical transport properties and optical properties can be finely tuned with nanoparticle size and ligand length. Long ligands result in low mobilities and well-defined emission profiles, while no ligands yield high mobilities at the cost of the quantum confined optical properties and extreme spectral broadening. The analogous system, 1D conjugated polymers, also show tunable electronic and optical properties with structure[11]; these polymers can be processed with simple techniques like dip-coating or spin-coating to prepare 3D solids with designed properties[12]. In this regard, the development of 3D, bulk-like materials that retain their quantum confined properties has enabled significant advances in numerous optoelectronic devices[13]. It remains to be seen, however, if quantum-confined 3D materials can be built from 2D materials.

1.2 2D Materials as building blocks

Two-dimensional materials (2DM) have emerged as an important class of nanomaterials with applications in energy conversion[14] and information technology[15-16]. Individual 2D flakes can function as building blocks for engineered 3D materials, and often possess unique optical, electrical, and physical properties due to quantum confinement. As the first exfoliated 2DM, graphene has been shown to have a high carrier mobility of 100,000 $cm^2\ V^{-1}\ s^{-1}$, yet has low optical absorption and is a quasi-metal with no band gap[17]. While the lack of band gap has limited some of the applications of graphene, 2D transition metal dichalcogenides (TMDs) such as molybdenum disulfide (MoS_2) and tungsten diselenide (WSe_2) offered new alternatives to designing semiconducting materials. MoS_2 has a thickness dependent band gap that transitions from 1.2 to 1.8 eV as the materially is thinned, and is direct in the completely quantum confined case of a single layer[18]. The isoelectric equivalent of graphene, 2D hexagonal boron nitride (hBN), is an insulator with a band gap of 5.9 eV.

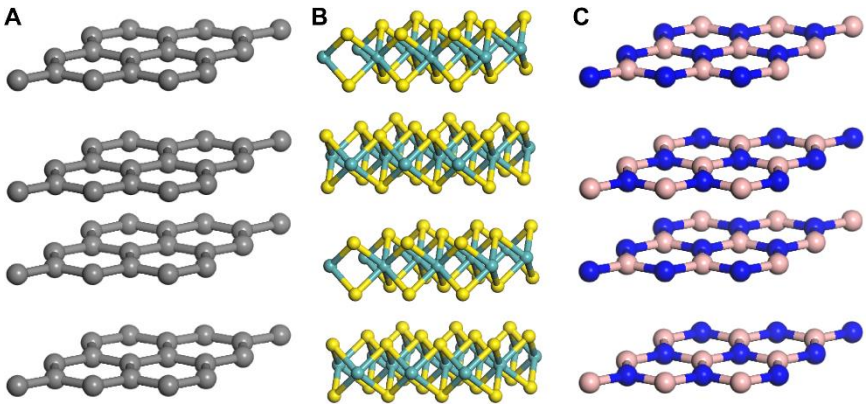

Figure 1-1. Layered van der Waals solids for 2D Materials: (A) Graphite **(B)** Transition Metal Dichalcogendies (Teal: Mo, W, Zr, Ti; Yellow: S, Se, Te) **(C)** hexagonal Boron Nitride (Pink: Boron; Blue: Nitrogen)

Graphene, hBN, and the transition metal dichalcogenides (TMDs) span a large range of optoelectronic properties and can be thought of as the iconic pillars for designing 2DM architectures. Applications in spintronics, photovoltaics, and transistors, however, require materials with increasingly specific magnetic, optical, and electronic properties. Appropriately, the library of 2DMs is constantly expanding from both experimental observation and computational prediction to meet these needs. Elemental 2DMs beyond graphene now include silicene[19-21], phosphorene[22-23], antimonene[24-25], arsenene[25], and borophene[26-27], which possess quantum-confined optical properties or topological Dirac states. Ferromagnetic layered materials, such as $Cr_2Ge_2Te_6$[28-29] and Gd_2C[30], and their exfoliation to monolayers would push the field of 2DM nanoelectronics into advanced magnetic and spintronic applications. One of the most interesting new additions to the 2DM family are the electrenes. Prepared from the exfoliation of layered electrides, the electrenes consist of $[M_2X]^+$ ionic slabs and an anionic electron gas occupying the interlayer space to maintain charge neutrality[31-32]. Electrenes can be prepared from pnictogenides (X=N, P M= Ca, Sr, Ba) and carbides (X=C, M=Y, Gd, Sc, Ho) and offer an opportunity for fundamental investigations of interlayer interactions in 2DM heterostructures.

In addition to expanding the breadth of physical and optoelectronic properties that exist for 2DMs, these materials must also be easily prepared with pristine quality to ensure that heterostructures can be designed with high precision and control. To this end, mechanical and liquid exfoliation[33-37] have been used as top-down approaches to prepare 2DMs from layered materials. Scotch tape and Nitto tape can cleave the weak van der Waals forces of layered materials to produce up to $1mm^2$ flakes of 2DMs, and the resulting materials can be easily transferred and assembled with thermal stamps. Alternatively, liquid phase exfoliation in

appropriate solvents can produce large quantities of ultrathin flakes. An exceptional example of this is the intercalation of MoS_2 with n-butyllithium, which can then be exfoliated in water for a large yield of monolayer flakes[38-40]. Chemical-vapor deposition is the leading technique for bottom-up syntheses of 2DMs and affords precise control over flake thickness, orientation, and composition[41-44]. Additionally, CVD can be used as a direct synthetic route to epitaxially grow 2DM assemblies, and thus avoiding the tedious lift-off and transfer steps required for mechanically exfoliated samples.

1.2.1 Weak interlayer interactions in 2DM architectures: van der Waals forces

The planar morphology and library of 2DMs has enabled their use as structural components in highly designed nanoarchitectures, known as van der Waals heterostructures[45]. These materials can be thought of as the physisorption of 2DMs into an assembled structure; the weak interlayer van der Waals forces and large interlayer distances do not usually cause a profound change in the electronic structure or interlayer bonding of the material. In fact, most 2DM assemblies retain their intrinsic electronic properties, or even have their properties enhanced. For example, the assembly of a hBN/graphene heterostructure has resulted in an unprecedented mobility of up to 500,000 $cm^2 V^{-1} s^{-1}$ at low temperatures, because of an increased dielectric screening for charge transport and preservation of the Dirac cone[17]. In van der Waals heterostructures of MoS_2 and WS_2, individual components retain their electronic structure because of weak interlayer coupling, allowing precise band engineering in atomically thin materials; these materials form nanometer thick Type II semiconductor junctions with spatially separated electrons and holes and a direct band gap[46]. A final example of the importance of weak interlayer interactions in 2DM assemblies is the field-effect tunneling transistor (FETT). In a typical FETT, graphene electrodes are separated by few-layer thick flakes of MoS_2, WS_2, or

hBN. Because of the weak interlayer interactions, the insulating 2DM behaves purely as a tunneling barrier with length equivalent to the thickness of the flake. FETTs have fast transfer kinetics due to tunneling, nanometer scale morphology appropriate for advanced technological applications, and an on/off ratio of 10^6 at room temperature[47-48].

While these assemblies and devices take advantage of large interlayer distances and weak interlayer coupling, there are opportunities for strong coupling as well. Perhaps the systems that have the greatest potential for interlayer coupling are heterostructures consisting of a single type of 2DM (e.g. stacked MoS_2 monolayers). Previous studies on MoS_2 heterostructures have shown that electronic coupling and interlayer distance between independent flakes can be controlled with rotational disorder and result in a reemergence of quantum-confined properties at larger separations[49-54]. Black phosphorus, a layered material of puckered sheets of phosphorus with interdigitated p_z orbitals, exhibits a similar dependence on rotational disorder: a rotated bilayer flake of phosphorene has larger interlayer distances and a similar electronic structure to that of a monolayer phosphorene. Because of the potential for a 2DM to electronically couple with itself and lose its quantum-confined properties, it remains an unanswered question whether large-scale assemblies can be included in the 'confined-yet-coupled' class of materials.

1.2.2 Strong interactions in 2DM architectures: bonding and charge transfer

In contrast to physisorption, the chemisorption of 2DMs can alter the electronic structure of individual components due to charge transfer or interlayer quasi-bonding. Hydrogen bonds are the second weakest intermolecular force, compared to van der Waals, and require the chemical modification of 2DMs to include hydroxyl functionalities. These functionalized sheets can then be crosslinked with molecules, such as water[55] or borate[56] to increase the mechanical strength of 2DM assemblies at the cost of the intrinsic electronic structure. A similar trade-off between

stronger interlayer interactions and electronic structure can be observed for coordinative bonding (i.e. crosslinking with metal oxide molecules) or covalent bonding (i.e. direct interlayer bonding due to defects)[57].

An alternative approach to increasing the strength of interlayer interactions is by introducing an electrostatic force *via* charge transfer. One such example is the pairing of n-type MoO_3 with graphene[58-61]. Band bending and charge transfer will dope graphene p-type and shift the fermi level down 0.25 eV. Despite this charge transfer, the strength of the interaction is still relatively weak, thereby maintaining the integrity of the Dirac cone and the electrical transport properties of graphene. In this regard, the electrenes are exciting prospective materials as components for 2DM heterostructures. With ultra-low workfunctions of *ca.* 2.8 eV, they are ideal candidates for massive charge transfer and strong electrostatic forces between layers. For a $Ca_2N/MoTe_2$ heterostructure, Sera Kim *et al.* found a transferred charge density of 10^{14} cm^{-2} and a structural lattice rearrangement from semiconducting 2H to metallic 1T' phase[62]. However, this has been the only experimental study of an electrene/2DM heterostructure using thick bulk-like flakes and warrants fundamental investigations, both computational and experimental, on strong interlayer interactions in electrene/2DM heterostructures. It remains to be seen if the modularity of van der Waals heterostructures with highly designed architectures, can also be applied to 2DM assemblies exhibiting strong charge transfer and interlayer interactions.

1.3 Research Overview

In this dissertation, I introduce phosphorene as a new 2DM that can be prepared from the liquid exfoliation of black phosphorus (Chapter Three). I identified monolayer phosphorene using transmission electron microscopy and electron diffraction simulation. We found that phosphorene has a thickness dependent band gap of 2.0 eV and 0.33 eV for 2D and bulklike

flakes, respectively. This range is unprecedented for a 2D material and even surpasses that of many quantum dots[63], making it an exciting new building block for the design of 3D architectures.

I then performed fundamental investigations on the assembly of phosphorene, as well as other semiconducting 2DMs such as MoS_2 and WSe_2, into 3D films (Chapter Four). We found that 2DM materials retain their quantum confined properties using photoluminescence and Raman spectroscopy, despite electronic coupling between adjacent flakes. I determined that electrical transport proceeds via hopping and measured an activation energy of 0.250 to 1.2 eV, depending on the thickness of the 2DM building block. We conclude that 2DM films can be described as confined-yet-coupled systems, making them an exciting material to explore for applications requiring highly designed semiconductors.

Finally, I explore the applications of electrenes as a building block for designing a new class of materials, called Coulombic heterostructures, in which electrostatic forces dominate the interlayer gap (Chapter Five). Here I show computationally that there is a massive charge transfer between 2D electrides and 2DMs, resulting in quasi-bond formation. Coulombic heterostructures show drastically modified properties compared to their starting materials, including defect-free doping, low work functions, ultralow sliding energies, and tunable voltages for ion intercalation.

REFERENCES

1. Rossetti, R.; Nakahara, S.; Brus, L. E., Quantum size effects in the redox potentials, resonance Raman spectra, and electronic spectra of CdS crystallites in aqueous solution. *The Journal of Chemical Physics* **1983,** *79* (2), 1086-1088.

2. Brus, L., Electronic wave functions in semiconductor clusters: experiment and theory. *The Journal of Physical Chemistry* **1986,** *90* (12), 2555-2560.

3. Dannhauser, T.; O'neil, M.; Johansson, K.; Whitten, D.; McLendon, G., Photophysics of quantized colloidal semiconductors. Dramatic luminescence enhancement by binding of simple amines. *The Journal of Physical Chemistry* **1986,** *90* (23), 6074-6076.

4. Reed, M.; Randall, J.; Aggarwal, R.; Matyi, R.; Moore, T.; Wetsel, A., Observation of discrete electronic states in a zero-dimensional semiconductor nanostructure. *Physical Review Letters* **1988,** *60* (6), 535.

5. Rossetti, R.; Hull, R.; Gibson, J.; Brus, L. E., Excited electronic states and optical spectra of ZnS and CdS crystallites in the≅ 15 to 50 Å size range: Evolution from molecular to bulk semiconducting properties. *The Journal of chemical physics* **1985,** *82* (1), 552-559.

6. Lin, X.; Jaeger, H.; Sorensen, C.; Klabunde, K., Formation of long-range-ordered nanocrystal superlattices on silicon nitride substrates. *The Journal of Physical Chemistry B* **2001,** *105* (17), 3353-3357.

7. Murray, C.; Kagan, C.; Bawendi, M., Self-organization of CdSe nanocrystallites into three-dimensional quantum dot superlattices. *Science* **1995,** *270* (5240), 1335-1338.

8. Baumgardner, W. J.; Whitham, K.; Hanrath, T., Confined-but-connected quantum solids via controlled ligand displacement. *Nano letters* **2013,** *13* (7), 3225-3231.

9. Choi, J.-H.; Fafarman, A. T.; Oh, S. J.; Ko, D.-K.; Kim, D. K.; Diroll, B. T.; Muramoto, S.; Gillen, J. G.; Murray, C. B.; Kagan, C. R., Bandlike transport in strongly coupled and doped quantum dot solids: a route to high-performance thin-film electronics. *Nano letters* **2012,** *12* (5), 2631-2638.

10. Talgorn, E.; Gao, Y.; Aerts, M.; Kunneman, L. T.; Schins, J. M.; Savenije, T.; Van Huis, M. A.; Van Der Zant, H. S.; Houtepen, A. J.; Siebbeles, L. D., Unity quantum yield of photogenerated charges and band-like transport in quantum-dot solids. *Nature nanotechnology* **2011,** *6* (11), 733.

11. Shirakawa, H.; Louis, E. J.; MacDiarmid, A. G.; Chiang, C. K.; Heeger, A. J., Synthesis of electrically conducting organic polymers: halogen derivatives of polyacetylene,(CH) x. *Journal of the Chemical Society, Chemical Communications* **1977,** (16), 578-580.

12. Gustafsson, G.; Cao, Y.; Treacy, G.; Klavetter, F.; Colaneri, N.; Heeger, A., Flexible light-emitting diodes made from soluble conducting polymers. *Nature* **1992,** *357* (6378), 477.

13. Talapin, D. V.; Lee, J.-S.; Kovalenko, M. V.; Shevchenko, E. V., Prospects of colloidal nanocrystals for electronic and optoelectronic applications. *Chemical reviews* **2009,** *110* (1), 389-458.

14. Jaramillo, T. F.; Jørgensen, K. P.; Bonde, J.; Nielsen, J. H.; Horch, S.; Chorkendorff, I., Identification of active edge sites for electrochemical H2 evolution from MoS2 nanocatalysts. *science* **2007,** *317* (5834), 100-102.

15. Dean, C. R.; Young, A. F.; Meric, I.; Lee, C.; Wang, L.; Sorgenfrei, S.; Watanabe, K.; Taniguchi, T.; Kim, P.; Shepard, K. L., Boron nitride substrates for high-quality graphene electronics. *Nature nanotechnology* **2010,** *5* (10), 722.

16. Radisavljevic, B.; Radenovic, A.; Brivio, J.; Giacometti, i. V.; Kis, A., Single-layer MoS 2 transistors. *Nature nanotechnology* **2011,** *6* (3), 147.

17. Mayorov, A. S.; Gorbachev, R. V.; Morozov, S. V.; Britnell, L.; Jalil, R.; Ponomarenko, L. A.; Blake, P.; Novoselov, K. S.; Watanabe, K.; Taniguchi, T., Micrometer-scale ballistic transport in encapsulated graphene at room temperature. *Nano letters* **2011,** *11* (6), 2396-2399.

18. Mak, K. F.; Lee, C.; Hone, J.; Shan, J.; Heinz, T. F., Atomically Thin MoS2. A New Direct-Gap Semiconductor. *Phys. Rev. Lett.* **2010,** *105* (13), 136805/1-136805/4.

19. Fleurence, A.; Friedlein, R.; Ozaki, T.; Kawai, H.; Wang, Y.; Yamada-Takamura, Y., Experimental evidence for epitaxial silicene on diboride thin films. *Physical review letters* **2012,** *108* (24), 245501.

20. Liu, C.-C.; Feng, W.; Yao, Y., Quantum spin Hall effect in silicene and two-dimensional germanium. *Physical review letters* **2011,** *107* (7), 076802.

21. Vogt, P.; De Padova, P.; Quaresima, C.; Avila, J.; Frantzeskakis, E.; Asensio, M. C.; Resta, A.; Ealet, B.; Le Lay, G., Silicene: compelling experimental evidence for graphenelike two-dimensional silicon. *Physical review letters* **2012,** *108* (15), 155501.

22. Liu, H.; Neal, A. T.; Zhu, Z.; Luo, Z.; Xu, X.; Tománek, D.; Ye, P. D., Phosphorene: an unexplored 2D semiconductor with a high hole mobility. *ACS nano* **2014,** *8* (4), 4033-4041.

23. Woomer, A. H.; Farnsworth, T. W.; Hu, J.; Wells, R. A.; Donley, C. L.; Warren, S. C., Phosphorene: synthesis, scale-up, and quantitative optical spectroscopy. *ACS nano* **2015,** *9* (9), 8869-8884.

24. Ji, J.; Song, X.; Liu, J.; Yan, Z.; Huo, C.; Zhang, S.; Su, M.; Liao, L.; Wang, W.; Ni, Z., Two-dimensional antimonene single crystals grown by van der Waals epitaxy. *Nature communications* **2016,** *7*, 13352.

25. Zhang, S.; Yan, Z.; Li, Y.; Chen, Z.; Zeng, H., Atomically thin arsenene and antimonene: semimetal–semiconductor and indirect–direct band-gap transitions. *Angewandte Chemie* **2015,** *127* (10), 3155-3158.

26. Li, W.-L.; Chen, Q.; Tian, W.-J.; Bai, H.; Zhao, Y.-F.; Hu, H.-S.; Li, J.; Zhai, H.-J.; Li, S.-D.; Wang, L.-S., The B35 cluster with a double-hexagonal vacancy: a new and more flexible structural motif for borophene. *Journal of the American Chemical Society* **2014,** *136* (35), 12257-12260.

27. Peng, B.; Zhang, H.; Shao, H.; Xu, Y.; Zhang, R.; Zhu, H., The electronic, optical, and thermodynamic properties of borophene from first-principles calculations. *Journal of Materials Chemistry C* **2016,** *4* (16), 3592-3598.

28. Carteaux, V.; Brunet, D.; Ouvrard, G.; Andre, G., Crystallographic, magnetic and electronic structures of a new layered ferromagnetic compound Cr2Ge2Te6. *Journal of Physics: Condensed Matter* **1995,** *7* (1), 69.

29. Xing, W.; Chen, Y.; Odenthal, P. M.; Zhang, X.; Yuan, W.; Su, T.; Song, Q.; Wang, T.; Zhong, J.; Jia, S., Electric field effect in multilayer Cr2Ge2Te6: a ferromagnetic 2D material. *2D Materials* **2017,** *4* (2), 024009.

30. Mudryk, Y.; Paudyal, D.; Pecharsky, V.; Gschneidner, K., Magnetic properties of Gd2C: Experiment and first principles calculations. *Journal of applied physics* **2011,** *109* (7), 07A924.

31. Druffel, D. L.; Kuntz, K. L.; Woomer, A. H.; Alcorn, F. M.; Hu, J.; Donley, C. L.; Warren, S. C., Experimental Demonstration of an Electride as a 2D Material. *Journal of the American Chemical Society* **2016,** *138* (49), 16089-16094.

32. Druffel, D. L.; Woomer, A. H.; Kuntz, K. L.; Pawlik, J. T.; Warren, S. C., Electrons on the surface of 2D materials: from layered electrides to 2D electrenes. *Journal of Materials Chemistry C* **2017,** *5* (43), 11196-11213.

33. Coleman, J. N.; Lotya, M.; O'Neill, A.; Bergin, S. D.; King, P. J.; Khan, U.; Young, K.; Gaucher, A.; De, S.; Smith, R. J.; Shvets, I. V.; Arora, S. K.; Stanton, G.; Kim, H. Y.; Lee, K.; Kim, G. T.; Duesberg, G. S.; Hallam, T.; Boland, J. J.; Wang, J. J.; Donegan, J. F.; Grunlan, J. C.; Moriarty, G.; Shmeliov, A.; Nicholls, R. J.; Perkins, J. M.; Grieveson, E. M.; Theuwissen, K.; McComb, D. W.; Nellist, P. D.; Nicolosi, V., Two-dimensional nanosheets produced by liquid exfoliation of layered materials. *Science* **2011,** *331* (6017), 568-71.

34. Cunningham, G.; Lotya, M.; Cucinotta, C. S.; Sanvito, S.; Bergin, S. D.; Menzel, R.; Shaffer, M. S.; Coleman, J. N., Solvent exfoliation of transition metal dichalcogenides: dispersibility of exfoliated nanosheets varies only weakly between compounds. *ACS nano* **2012,** *6* (4), 3468-3480.

35. Hernandez, Y.; Nicolosi, V.; Lotya, M.; Blighe, F. M.; Sun, Z.; De, S.; McGovern, I.; Holland, B.; Byrne, M.; Gun'Ko, Y. K., High-yield production of graphene by liquid-phase exfoliation of graphite. *Nature nanotechnology* **2008,** *3* (9), 563.

36. Nicolosi, V.; Chhowalla, M.; Kanatzidis, M. G.; Strano, M. S.; Coleman, J. N., Liquid exfoliation of layered materials. *Science* **2013,** *340* (6139), 1226419.

37. O'Neill, A.; Khan, U.; Coleman, J. N., Preparation of High Concentration Dispersions of Exfoliated MoS2with Increased Flake Size. *Chemistry of Materials* **2012,** *24* (12), 2414-2421.

38. Cao, B.; Li, T., Interlayer Electronic Coupling in Arbitrarily Stacked MoS2Bilayers Controlled by Interlayer S–S Interaction. *The Journal of Physical Chemistry C* **2015,** *119* (2), 1247-1252.

39. Wang, Z.; Chen, Q.; Wang, J., Electronic Structure of Twisted Bilayers of Graphene/MoS2and MoS2/MoS2. *The Journal of Physical Chemistry C* **2015,** *119* (9), 4752-4758.

40. Joensen, P.; Frindt, R.; Morrison, S. R., Single-layer MoS2. *Materials research bulletin* **1986,** *21* (4), 457-461.

41. Liu, B.; Fathi, M.; Chen, L.; Abbas, A.; Ma, Y.; Zhou, C., Chemical vapor deposition growth of monolayer WSe2 with tunable device characteristics and growth mechanism study. *ACS nano* **2015,** *9* (6), 6119-6127.

42. Liu, H.; Wong, S. L.; Chi, D., CVD Growth of MoS2-based Two-dimensional Materials. *Chemical Vapor Deposition* **2015,** *21* (10-11-12), 241-259.

43. Shi, Y.; Li, H.; Li, L.-J., Recent advances in controlled synthesis of two-dimensional transition metal dichalcogenides via vapour deposition techniques. *Chemical Society Reviews* **2015,** *44* (9), 2744-2756.

44. Zhang, Y.; Zhang, L.; Zhou, C., Review of chemical vapor deposition of graphene and related applications. *Accounts of chemical research* **2013,** *46* (10), 2329-2339.

45. Geim, A. K.; Grigorieva, I. V., Van der Waals heterostructures. *Nature* **2013,** *499* (7459), 419.

46. Kośmider, K.; Fernández-Rossier, J., Electronic properties of the MoS 2-WS 2 heterojunction. *Physical Review B* **2013,** *87* (7), 075451.

47. Britnell, L.; Gorbachev, R.; Jalil, R.; Belle, B.; Schedin, F.; Mishchenko, A.; Georgiou, T.; Katsnelson, M.; Eaves, L.; Morozov, S., Field-effect tunneling transistor based on vertical graphene heterostructures. *Science* **2012,** *335* (6071), 947-950.

48. Georgiou, T.; Jalil, R.; Belle, B. D.; Britnell, L.; Gorbachev, R. V.; Morozov, S. V.; Kim, Y.-J.; Gholinia, A.; Haigh, S. J.; Makarovsky, O., Vertical field-effect transistor based on graphene–WS 2 heterostructures for flexible and transparent electronics. *Nature nanotechnology* **2013,** *8* (2), 100.

49. Cao, B.; Li, T., Interlayer electronic coupling in arbitrarily stacked MoS2 bilayers controlled by interlayer S–S interaction. *The Journal of Physical Chemistry C* **2014,** *119* (2), 1247-1252.

50. Castellanos-Gomez, A.; van der Zant, H. S.; Steele, G. A., Folded MoS 2 layers with reduced interlayer coupling. *Nano Research* **2014,** *7* (4), 572-578.

51. Huang, S.; Ling, X.; Liang, L.; Kong, J.; Terrones, H.; Meunier, V.; Dresselhaus, M. S., Probing the interlayer coupling of twisted bilayer MoS2 using photoluminescence spectroscopy. *Nano letters* **2014,** *14* (10), 5500-5508.

52. Liu, K.; Zhang, L.; Cao, T.; Jin, C.; Qiu, D.; Zhou, Q.; Zettl, A.; Yang, P.; Louie, S. G.; Wang, F., Evolution of interlayer coupling in twisted molybdenum disulfide bilayers. *Nature communications* **2014,** *5*, 4966.

53. van Der Zande, A. M.; Kunstmann, J.; Chernikov, A.; Chenet, D. A.; You, Y.; Zhang, X.; Huang, P. Y.; Berkelbach, T. C.; Wang, L.; Zhang, F., Tailoring the electronic structure in bilayer molybdenum disulfide via interlayer twist. *Nano letters* **2014,** *14* (7), 3869-3875.

54. Zheng, S.; Sun, L.; Zhou, X.; Liu, F.; Liu, Z.; Shen, Z.; Fan, H. J., Coupling and Interlayer Exciton in Twist-Stacked WS2 Bilayers. *Advanced Optical Materials* **2015,** *3* (11), 1600-1605.

55. Compton, O. C.; Cranford, S. W.; Putz, K. W.; An, Z.; Brinson, L. C.; Buehler, M. J.; Nguyen, S. T., Tuning the mechanical properties of graphene oxide paper and its associated polymer nanocomposites by controlling cooperative intersheet hydrogen bonding. *ACS nano* **2012,** *6* (3), 2008-2019.

56. An, Z.; Compton, O. C.; Putz, K. W.; Brinson, L. C.; Nguyen, S. T., Bio-inspired borate cross-linking in ultra-stiff graphene oxide thin films. *Advanced Materials* **2011,** *23* (33), 3842-3846.

57. Gao, E.; Cao, Y.; Liu, Y.; Xu, Z., Optimizing Interfacial Cross-Linking in Graphene-Derived Materials, Which Balances Intralayer and Interlayer Load Transfer. *ACS applied materials & interfaces* **2017,** *9* (29), 24830-24839.

58. Chen, Z.; Santoso, I.; Wang, R.; Xie, L. F.; Mao, H. Y.; Huang, H.; Wang, Y. Z.; Gao, X. Y.; Chen, Z. K.; Ma, D., Surface transfer hole doping of epitaxial graphene using MoO 3 thin film. *Applied Physics Letters* **2010,** *96* (21), 213104.

59. Esconjauregui, S.; D'Arsié, L.; Guo, Y.; Yang, J.; Sugime, H.; Caneva, S.; Cepek, C.; Robertson, J., Efficient transfer doping of carbon nanotube forests by moo3. *ACS nano* **2015,** *9* (10), 10422-10430.

60. Hellstrom, S. L.; Vosgueritchian, M.; Stoltenberg, R. M.; Irfan, I.; Hammock, M.; Wang, Y. B.; Jia, C.; Guo, X.; Gao, Y.; Bao, Z., Strong and stable doping of carbon nanotubes and graphene by MoO x for transparent electrodes. *Nano letters* **2012,** *12* (7), 3574-3580.

61. Meyer, J.; Kidambi, P. R.; Bayer, B. C.; Weijtens, C.; Kuhn, A.; Centeno, A.; Pesquera, A.; Zurutuza, A.; Robertson, J.; Hofmann, S., Metal oxide induced charge transfer doping and band alignment of graphene electrodes for efficient organic light emitting diodes. *Scientific reports* **2014,** *4*, 5380.

62. Kim, S.; Song, S.; Park, J.; Yu, H. S.; Cho, S.; Kim, D.; Baik, J.; Choe, D.-H.; Chang, K. J.; Lee, Y. H., Long-Range Lattice Engineering of MoTe2 by a 2D Electride. *Nano letters* **2017,** *17* (6), 3363-3368.

63. Baskoutas, S.; Terzis, A. F., Size-dependent band gap of colloidal quantum dots. *Journal of applied physics* **2006,** *99* (1), 013708.

CHAPTER TWO – METHODS FOR PREPARATION, PROCESSING, AND CHARACTERIZATION OF 2D MATERIALS AND FILMS

2.1 Introduction

Over the last five years, I have developed expertise in the exfoliation of layered materials, transmission electron microscopy, electrical measurements with van der Pauw geometry, and Density Functional Theory (DFT). In this chapter, I present experimental and computational details that do not appear elsewhere in my dissertation. This includes techniques for the mechanical and liquid exfoliation of layered materials (Section 2.2), the imaging of 2DMs with TEM to identify thin flakes from electron diffraction and simulation (Section 2.3), the measurement of conductivity and activation energy for charge transport in 2DM films (Section 2.4) and finally, specific equations and calculations to study the stability and physical, optical, and electrical properties 2DMs and their heterostructures (Section 2.5).

2.2 Preparation of 2D materials from bulk layered crystals

2.2.1 Mechanical Exfoliation

Since the experimental observation of graphene in 2004[1], the scotch-tape exfoliation method has been shown to be a viable, albeit tedious synthetic route for producing 2D materials. In this approach, a piece of Scotch tape, Nitto tape, or alternative adhesive is adhered to the surface of the crystal. The adhesive is then peeled overcoming the weak van der Waals forces to pull apart adjacent layers. The sample can then be thinned further with multiple cleavage events, or can be deposited on a substrate by pressing the tape onto the surface and peeling away. Finally, tape residue is removed from the substrate with acetone and IPA rinses. While this technique can

produce monolayers of a 2DM, there are significant disadvantages. The overall yield is extremely low and requires optical microscopy to identify monolayers. Tape residue is difficult to remove from the sample and can further complicate the identification of monolayers. Lateral dimensions of ultrathin flakes can be extremely small or only limited to the edge of thicker flakes.

Despite these challenges, I explored mechanical exfoliation as a technique to produce monolayers of black phosphorus. While other studies have shown that the observation of monolayers is exceedingly rare due to the material's tendency to oxidize and degrade, I quantitatively assessed the potential of mechanical exfoliation to easily and reproducibly yield thin flakes. I prepared and analyzed samples under an inert atmosphere, using scotch tape for exfoliation and a Bruker Dimension FastScan atomic force microscope (AFM) to rapidly analyze sheet thickness over macroscopic areas. The thickness of over 3,000 flakes was assessed from random survey of larger areas. This analysis revealed that the yield of flakes thinner than 10 layers is less than 0.06%; in addition, no flakes thinner than 6 layers were found. Given the low odds for identifying and characterizing black phosphorus and other 2D materials prepared in this way, the preparation method that I have primarily used in my experimental work is liquid exfoliation.

2.2.2 Liquid Exfoliation

An alternative approach to the preparation of two-dimensional materials is liquid exfoliation, in which a layered crystal is placed in an appropriate solvent and subjected to ultrasonication[2-3]. In principle, a successful liquid exfoliation relies on the combination of two physical processes: cavitation of the solution induced by sonication applies a shearing and cleaving force to the layered material, while an optimal solvent is chosen to minimize the exfoliation energy and to prevent the aggregation and settling of the 2DM particulates. Typically, solvents are chosen by their ability to match the surface energy, Hansen solubility parameters, or density of the layered

material[2, 4-7]. To assess the efficacy of the chosen solvent and the sonication parameters, the concentration of 2D material suspensions are analyzed with mass-spectrometry and compared to the measured amount of starting layered material. Additionally, solvents are qualitatively assessed on their ability to retain the suspension of 2D materials – i.e. no change in absorbance, formation of aggregates, or chemical reactions for at least one week.

To prepare two-dimensional materials in our lab, layered crystals were slightly crushed using a mortar and pestle in a nitrogen glove box. For typical experiments, 10 mg of powder was weighed into a 20-mL scintillation vial. Twenty milliliters of solvent was added to give a concentration of 0.5 mg/mL. Vials were tightly capped and, when necessary, wrapped with parafilm to prevent air exposure before placing into a Branson 5800 bath sonicator. The bath sonicator was outfitted with a test tube rack to allow for controlled placement of vials. Vials were systematically moved through several locations in the rack during the course of sonication to minimize vial-to-vial variations in material dispersion. The samples were subjected to eight to ten cycles of sonication, each lasting 99 minutes. Bath water was changed after each cycle to maintain a temperature between 22 and 30 °C (during sonication, bath temperature increased dramatically). During the sonication process, the layered crystals dispersed into the solution and the suspensions acquired a colored appearance that is dependent on the material being exfoliated. After sonication, air-sensitive samples were returned to the glove box.

To fractionate 2DM suspensions and isolate narrow thickness distributions, we employed a three-step centrifugation protocol. First, solutions were transferred to Nalgene Oak Ridge FEP 10- or 50-mL centrifuge tubes. The solutions were centrifuged in a Sorvall RC-5B superspeed refrigerated centrifuge (rotor radius 10.7 cm). Second, the supernatant from the centrifuge tubes was collected and transferred to a clean centrifuge tube. Third, the supernatant was centrifuged at

a speed higher than the first run. The sediment was collected and redispersed in fresh solvent. Depending on choice of centrifugation speeds, these fractionated suspensions contained 2DMs with narrow and systematically varying thicknesses distributions (see Fig. 3-4 a,b).

As a typical example, a distribution could be collected at RCF values between 17,200*g* and 23,400*g*. The tube would first be spun at 17,200*g* for 30 minutes. The resulting supernatant would then be removed and re-centrifuged at 23,400*g* for 30 minutes. The sediment from the second centrifuge would then contain a distribution of flakes that could then be redispersed into any solvent (often we chose IPA) for further analysis; for simplicity, we label this new suspension as 20,200g, the average RCF between the two sequential centrifugation steps. All solution transfers between centrifuge tubes were performed inside a glove box. High speed centrifugations (>12,000*g*) were performed at 4 °C to lengthen tube lifetime. Following the final centrifugation steps, 2DM suspension are then ready for deposition as films, optical characterization, or preparation as transmission electron microscopy samples.

Table 2-1. Labeling of centrifugation fractions containing 2DM suspensions

Sequential RCF (g)	Label (1,000g)
30 to 480	0.12
480 to 1,900	1.1
1,900 to 4,300	3.0
7,700 to 12,000	9.7
17,200 to 23,400	20.2

2.3 Advanced transmission electron microscopy techniques for 2D materials

In electron microscopy, an electron wavefront is used to illuminate samples. Compared to optical microscopes, a standard electron microscope appears similar in construction, and consists of an electron emission source, followed by a series of apertures and magnetic lenses to refocus diffracted and transmitted electron beams and ultimately reproduce an image on a phosphor screen (Figure 2-1).

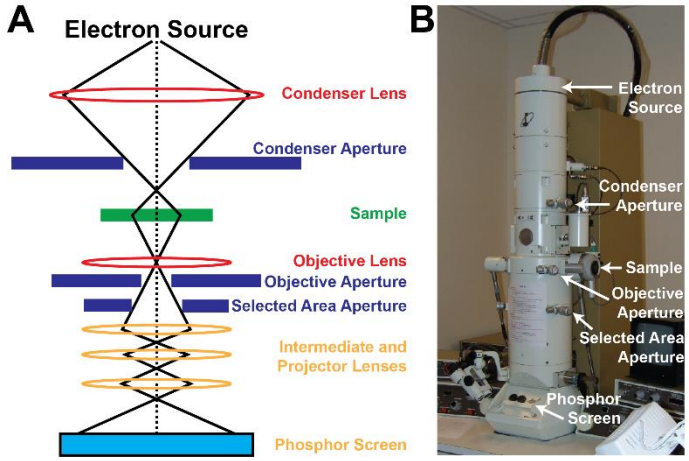

Figure 2-1. Electron Microscope Optics and Design: (**A**) Theoretical design of microscope column with lens and apertures for the projection of an electron image and (**B**) a JEOL 100 CX TEM for low-resolution imaging. Taken at CHANL, UNC Chapel Hill.

Despite these similarities, fundamental differences between the physics of electron and light optics enable TEM to achieve high spatial resolution, phase-contrast images, and coherent scattering of electrons. In the proceeding sections, I discuss the important TEM and TEM simulations techniques I developed or applied during my Ph.D. for the study of 2D materials, as well how they relate to the underlying physics of electron optics.

2.3.1 Edge contrast analysis

In its simplest application, TEM generates real space images of transparent samples, in which electrons passing through the sample are refocused and measured as an intensity of

electrons that reach the detector. Differences in intensity due to the presence of a sample causes contrast (Eqn. 2.1) in the resulting image.

$$C = \frac{I - I_0}{I} \qquad (2.1)$$

There are three primary types of contrast in TEM: mass-thickness contrast, diffraction contrast, and phase contrast. In mass-thickness contrast, Rutherford scattering of the electron beam from atomic nuclei will lower the intensity and is dependent on atomic number *Z*, sample density, and thickness.

Previously, it has been shown that mass-thickness contrast can be used to determine the thickness of amorphous, biological, and metallic samples due to the linear relationship between specimen thickness and measured contrast[8-14]. However, special care must be taken during TEM imaging to limit the other contributions to contrast. For example, diffraction contrast caused by the elastic scattering of electrons from defects, tilted or 'bent' samples, or Bragg diffraction from crystal planes, can be removed by appropriately placing the objective aperture in the center of the optical axis so that only the transmitted electron beam is projected. In addition, phase contrast due to the phase shift in diffracted beams is present in every sample, however, its visualization relies on high accelerating voltages (>200 keV) for better resolution, small spherical aberrations for a coherent phase-shift, and higher magnifications to observe the spatial frequency of phase contrast. While these factors are critical for HRTEM image formation, they have little bearing on low resolution techniques where contrast is primarily from mass-thickness.

I build upon the mass-thickness contrast technique used for ultrathin materials to characterize the thickness of 2D materials and identify monolayer samples. The thickness of a layered crystal is a stepwise function of the number of layers. Given the linear relationship between thickness and contrast, it is expected that the observed contrast in a TEM image of

exfoliated 2D materials should also be a stepwise function, and that the smallest possible contrast is that of monolayer flake. The contrast from any flake is then a multiple of the smallest possible contrast and can be used to assign the thickness of any flake observed. I now present a detailed method for conducting an edge contrast analysis of a 2DM suspension of phosphorene, as well as selection bias and potential sources of error.

i. Sample Preparation – In a glove box, 2DM suspensions in IPA or NMP were dropcast (~10 µL) onto a 300-mesh copper TEM grid coated with Lacey carbon (Ted Pella). After deposition, the solvent was evaporated for one hour (IPA) or at least 48 hours (NMP). During this period, TEM grids were held with self-closing tweezers and were not blotted against filter paper to ensure that a representative distribution of the material was deposited. For air sensitive samples, the TEM grids were placed in a grid box wrapped in aluminum foil, placed in a nitrogen-filled zip-loc bag, and brought to the TEM. Grids were rapidly transferred into the TEM with a minimal amount of light exposure. A JEOL 100CX II TEM was used for low resolution imaging. The TEM was operated at 100 kV accelerating voltage and had a resolution of 2 Å (lattice) and 3 Å (point to point).

ii. Alignment – The microscope was carefully aligned, including objective lens, condenser lens, gun position, eucentric height and sample tilt. The latter two alignments are of critical importance to ensure there is no change in defocus or variation in sample height when translating across the grid. When a TEM is improperly aligned, diffracted electrons are not refocused in the image to the point of origin, causing an artificial (diffraction) contrast in the image.

iii. Imaging – A charge-coupled device (CCD) camera was used to acquire all TEM images. The scintillator crystal and camera were pristine and well maintained, and thus there were no

artifacts or variation in background seen in the resulting images. Each image was taken at identical imaging conditions including exposure time, magnification, and defocus value. All images were taken at Scherzer defocus with a complete refocusing of diffracted electrons, and only minor, if any, defocus adjustments were necessary between samples. No pictures were analyzed near the edge of the grid bars, due to the artificial uniform increase in brightness.

iv. *Contrast Analysis* - Contrast changes across phosphorus flake edges were measured by drawing a line profile across and perpendicular to the edge of the flake (Fig. 3.a, line and inset) using Gatan Digital Micrograph.. To first establish the thickness-contrast relationship for our TEM, I measured contrast change for 500 flakes and found that the smallest intensity change was 25 ± 3 counts and all other intensity changes were multiples of 25 counts (Fig. 3.c, inset). I therefore assigned an intensity change of 25, 50, 75, and 100 counts to monolayers, bilayers, trilayers, and four-layered 2D phosphorus flakes, respectively. I note that in some cases, the edge of the flake was over vacuum, and in other cases it was over a carbon film. The maximum difference between the two measurements was 9 counts, and the average difference was 4.4 ± 3.0 counts (N = 12). These numbers are considerably smaller than the average counts per layer of 25 ± 3 counts. I conclude that there was, in general, a negligible difference between these two cases.

v. *Sample Selection* – The analysis of edge contrast is central for the accurate determination of the optical properties of 2D phosphorus, however it also has the highest potential to introduce an analytical bias. We have identified the five most common occurrences for bias in the contrast analysis and here report their prevalence or prevention.

a. Organic Residue: Solvents and environmental organic contaminants will vaporize into an amorphous carbon film if not properly removed from the TEM grid, contributing a non-

uniform contrast to the flake and lacey carbon film. To account for this, we evaporated our solvent for extended periods of time (30 minutes to 48 hours) under vacuum. Samples with a non-uniform contrast due to organics were discarded from our analysis. This error is independent of flake thickness and we find that *c.a.* 10% of samples across all three suspensions were affected by organic residue. We note that thermal degassing could further eliminate organic residue.

b. Polycrystallinity: Phosphorus flakes with a large degree of polycrystallinity will always exhibit some amount of diffraction contrast that is not uniform across the flake, no matter how well the microscope is aligned or focused. We removed these flakes with a low speed centrifugation (500 RPM), and any flakes imaged showing diffraction contrast were not included in our final analysis. These flakes were *c.a.* 10% of all three combined phosphorus suspensions.

c. Multilayer flakes: The presence of flakes with more than one distinct thickness is uncontrollable, however this was only somewhat common in the thickest flake distributions (*c.a.* 15% of flakes have more than one thickness). These flakes are predominantly of one thickness, with >60% of flake area having the corresponding uniform contrast, and were thus assigned to this value for our optical analysis. In the medium and thinner distributions, nearly all flakes exhibited a complete uniform contrast. The overall representation of multilayer flakes for the combined three fractions was *c.a.* 6%.

d. Aggregation: During our TEM analysis, we have noticed a tendency for flakes to aggregate. We found that this occurrence is related to the volatility of the liquid exfoliation solvent as well as the deposition technique. To prevent this we used isopropanol as a high

vapor pressure solvent for TEM samples prepared specifically for edge contrast analysis. Because of the complexity of a 2D phosphorus aggregated structure, flakes can appear to be amorphous, polycrystalline, and have non-uniform contrast. We have chosen to not analyze any flakes that are a component of an aggregate.

e. Lateral Size: An important criterion for the proper execution of the edge contrast thickness measurements is constant magnification, however this can complicate the analysis of small 2D phosphorus flakes (<15 nm linear dimension for our chosen magnification). We have sought to analyze all flakes with size larger than 15 nm, and the observation of flakes smaller than this size was rare, (c.a. <1%). After applying the following techniques to eliminate sample bias, we believe we have accurately accounted for a representative sample of 2D phosphorus flakes in each suspension.

2.3.2 Electron diffraction and Fast-Fourier transforms (FFTs) to determine material thickness

For a given accelerating voltage, an emitted electron beam has a corresponding wavelength, λ. As electrons pass through a crystalline sample, they are scattered at some angle off of the optic axis with a corresponding phase shift. When this phase shift, or the path length difference, is equal to a multiple of λ (also known as meeting the Bragg condition), there is a constructive interference of diffracted beams. By altering the imaging conditions of the TEM with objective apertures and lens strength, a single diffracted beam can be projected as a dark field image, or each diffracted beam can be focused to create a spot pattern containing information on crystal structure and lattice spacing.

Constructive and deconstructive interference will ultimately determine which diffracted beams appear in a diffraction pattern and their intensity. In general, a miller plane family that

passes through all of the atoms of a unit cell will have a strong intensity in the diffraction pattern. There are 219 distinct space groups for crystals, and since a diffraction pattern is a two-dimensional projection of a 3D scattering event, both the symmetry and the orientation (zone axis) of a crystal is necessary to extract information on crystal structure and lattice constants.

2DMs present an interesting case for electron diffraction. Large changes in crystal symmetry can occur for monolayer, bilayer, and trilayers of 2DMs. We take advantage of these changes in symmetry to identify monolayer 2DMs using a careful analysis of diffraction patterns and FFT and a comparison to electron simulation. Here I describe the two critical techniques to characterize the thickness of 2DM using diffraction:

1. *Obtaining experimental diffraction patterns (DPs) and FFT*:

   TEM grids with dropcast suspensions of 2DMs were prepared as described in section 2.2.1. To obtain diffraction patterns, a properly aligned JEOL 100CX II TEM was used. The TEM was operated at 100 kV accelerating voltage and first samples were scanned for optimal flakes for interpretable diffraction patterns. An 'optimal' flake meets the following criteria: (i) isolated, to prevent double diffraction or polycrystalline patterns. (ii) low contrast, as described in section 2.3.1, contrast can be used to screen the sample for thin flakes quickly and efficiently. (iii) lateral size and position, flakes should be over vacuum and larger than the smallest selected area aperture (0.4 microns) to ensure coherent diffraction with detectable intensities. (iv) tilt, flakes should be lying almost perfectly flat so that the optical axis is perpendicular to the atomic layers. (v) defocus, samples should be imaged at Scherzer defocus so that all diffracted electrons are realigned to their point of origin.

Once a suitable sample was found the smallest selected area aperture was inserted and positioned over the flake. The TEM was switched to SA diffraction mode and a diffraction pattern would then illuminate the phosphor screen. To capture the pattern, the camera was inserted and a 0.1 s exposure time and 83 cm camera length were used. Immediately after the image is taken, the camera was removed to prevent damage to the CCD. The image can then be analyzed using Gatan Digital Micrograph to confirm that flakes are crystalline and oriented perpendicular to the electron beam.

Liquid exfoliation can result in flakes that have lateral dimensions too small to reliably observe a diffraction pattern. To characterize the thickness of these samples, a high-resolution JEOL 2010F-FasTEM at 200kV accelerating voltage was used to obtain FFTs. In addition to the previously outlined criteria for sample selection, flakes exhibiting strong phase-contrast are highly crystalline and ideal for FFT analysis. FFTs are easily obtained by capturing the back focal plane during standard HRTEM imaging. The resulting DPs (FFTs) from low resolution (high resolution) TEM can then be compared to electron microscopy simulations.

2. *Modeling Thickness Dependent FFT and DP using Java Electon Microscopy Simulation:*

I used Java Electron Microscopy Simulation (JEMS) software to predict variations in the DP and FFT of 2DMs as a function of thickness. Crystallographic information files (cif) were generated using Accelerys/BIOVIA Materials Studio for monolayer, bilayer, trilayer, etc, flakes. These files were then imported to JEMS and a zone axis perpendicular to the layered structure was chosen (typically [001]) for HRTEM imaging, DP, and FFT simulation.

Diffraction patterns were generated in JEMS with a straightforward application of structure factor for diffracting crystals, however, simulations for FFT are sensitive to HRTEM components and imaging conditions. The most important aspect of modeling FFTs is an accurate depiction of the contrast transfer function (Eqn. 2.2, 2.3).

$$T(\vec{k}) = \exp[2\pi i \chi(\vec{k})] \quad (2.2)$$

$$\chi(\vec{k}) = 0.25 C_s \lambda^3 k^4 + 0.5 \Delta z \lambda k^2 \quad (2.3)$$

The CTF determines the contrast observed for elements of an image with a given spatial frequency (k), and relies on the accelerating voltage (wavelength) of the electron beam, the spherical aberration C_s, and the defocus value *z*. Typically, Scherzer defocus (Eqn. 2.4) is chosen as a value of z to minimize the number of nodes in the CTF, thus simplifying the interpretation of the FFT and maximizing the range of frequencies observed in the image.

$$\Delta z = (\tfrac{4}{3} C_s \lambda)^{1/2} \quad (2.4)$$

Specifically, I modeled the experimental imaging conditions of our JEOL 2010F-FasTEM. The accelerating voltage of the electron beam was 200 kV, which corresponds to a wavelength of 0.0027 nm. This HRTEM is equipped with a high-resolution polepiece with a Cs of 1.00 mm, and samples were imaged near Scherzer defocus (61.0 nm). Using these values, I modeled the FFT of different thicknesses of 2DM. I quantified the intensities of the diffraction plane families in the HRTEM FFT simulations and DP using signal integration image analysis to establish a trend in spot intensities. Finally, the observed experimental DP and FFTs can be compared to simulations to characterize the thickness of exfoliated flakes. An illustrative case for black phosphorus is presented in Chapter Three, where the ratio of the intensity for [101]:[200] plane families is zero for

all even layered flakes, severely diminished (<1.0) for odd layered flakes greater with 3 or more layers, and strong (>>1.0) for a monolayer.

2.4 Temperature- and pressure-dependent electrical measurements on 2DM films

For metals and semiconductors, conductivity measurements are extremely important for the extrapolation of other electrical properties such as mobility, carrier concentration, and activation energy. Films of 2DMs present an interesting case for electrical measurements: individual flakes have high in-plane electrical transport, but interlayer transport is dominated by tunneling events due to the large van der Waals distance and low orbital overlap. Given the anisotropy of individual 2DM flakes, it is easy to infer a strong structure-property relationship for the electrical properties of reassembled 2DM films, including porosity, contaminants, and turbostratic disorder. To assess this relationship, I measured the conductivity of and activation energy for charge transport in 2DM films using uniaxial pressure and temperature-controlled van der Pauw resistivity measurements.

2.4.1 Van der Pauw geometry for conductivity and activation energy

In 1958, L.J. van der Pauw and coworkers developed an alternative approach to measuring the conductivity of samples with arbitrary shape[15]. Four contacts can be made around the perimeter of the sample, labeled *A*, *B*, *C* and *D* (Figure 2-2). A current is then sourced from contact *A* to *B,* and the potential measured from *C* to *D*. The resistance, for this orientation of measurement is given by the following equation:

$$R_{AB.CD} = V_{CD}/I_{AB} \qquad (2.5)$$

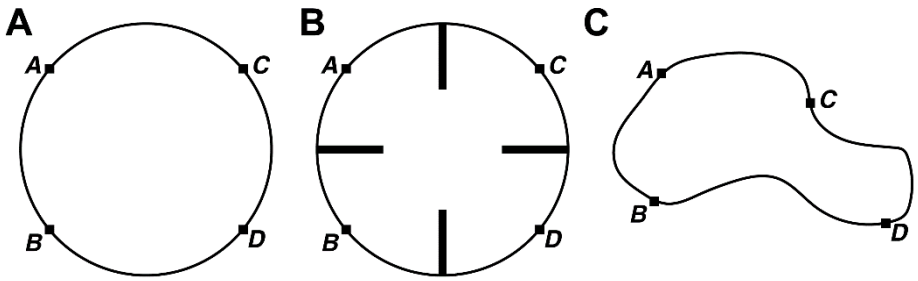

Figure 2-2. Common van der Pauw resistivity measurement geometries: (A) Circular sample with four contact points at the perimeter. **(B)** Cloverleaf geometry for Hall measurements. **(C)** Amorphous sample geometry

Given the four contacts points, there are four orientations for resistance measurements that can be taken and are as follows: $R_{AB.CD}$, $R_{BC.DA}$, $R_{CD.AB}$, and $R_{DA.BC}$. The average resistance for a current applied in a vertical orientation (R_v) and a horizontal orientation (R_h) can then be calculated.

$$R_v = \frac{R_{AB.CD} + R_{CD.AB}}{2} \tag{2.6}$$

$$R_h = \frac{R_{BC.DA} + R_{DA.BC}}{2} \tag{2.7}$$

These resistances can be then be used to solve for sheet resistance, R_s, using the following relationship:

$$\exp\left(-\frac{R_v \pi}{R_s}\right) + \exp\left(-\frac{R_h \pi}{R_s}\right) = 1 \tag{2.8}$$

Finally, it is a simple calculation to convert sheet resistance to conductivity:

$$\sigma = \frac{1}{(R_s\, d)} \tag{2.9}$$

where *d* is the thickness of the sample in either centimeters or meters and σ is conductivity in S/cm or S/m.

I modeled the electrical transport in assembled films of 2DM as hopping transport. Hopping can be described as discrete tunneling events across the length of a material and has the following relationship with temperature:

$$\sigma = \sigma_{min} exp(\frac{-E_a}{kT}) \quad (2.10)$$

where E_a is the activation energy for charge transport, *k* is Boltzman's constant and *T* is temperature. Plotting ln σ *vs*. 1/*T* can then be used to extract E_a as the slope of the line, as seen in Eqn _:

$$ln(\sigma) = \frac{-E_a}{kT} + A \quad (2.11)$$

I found that 2DM films follow the ln σ ~ 1/T relationship closely (See section 4.4) with minor deviations from linearity. Given that electrons must tunnel across vdW gaps, contaminants, or pores, it is expected that there is a good fit to the hopping model for 2DM films.

2.4.2 Preparation of vacuum filtered films

To prepare VF films for electrical measurements, 2DM suspensions were first passed through a 0.1 micron pore filter, type VVLP, from Millipore. Depending on the diameter of the filtration frit, either 20 mL of 3 mL of suspension was required to make 1 cm or 0.25 cm diameter film, respectively. After all of the suspension passed through the filter, the film was then washed with electronic grade IPA (99.999% purity) and allowed to air dry. Nitrogen was flowed over the film during each step to prevent oxidation of the material. Finally, vacuum filtered films were annealed under vacuum at 100° C in the large antechamber of a Vigor glovebox further dry samples and improve the processability of the film. to form four contact pads using a plastic mask. Contact pad dimensions were 1mm by 5 mm with approximately 1 mm^2 on the surface of the films at equidistant points on the perimeter of the film. The contact also extended off of the film and onto the membrane, to allow for electrical connections to be made that would not be directly pressurized. After annealing, contacts were placed onto films using thermal evaporation or e-beam evaporation.

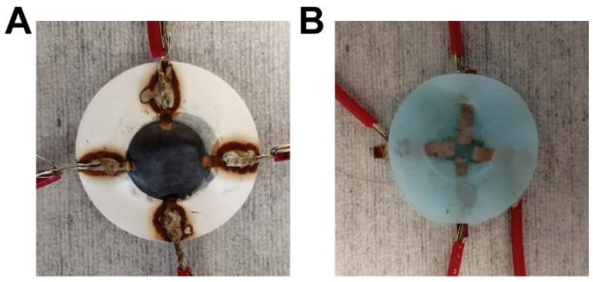

Figure 2-3. 2DM Films with electrical contacts: (A) Vacuum filtered film of MoS_2 with four contact points made at the periphery of the film. Nickel wires are adhered to the contact points using silver epoxy. **(B)** Langmuir-Blodgett trough film of MoS_2. Films were deposited onto a Teflon substrate and contacts are made with conductive copper tape. Wires can be adhered to the copper tape with silver epoxy or soldering.

Typically, 5 nm of chrome followed by 50 nm of gold were sputtered onto the film . This ensures that only the film and a small portion of the contact pads will experience the force of the pellet press. Four nickel wires were cut to a length of 5 cm and stripped at each end. A conductive silver epoxy (MG Chemicals #8331S-15G) was applied to one end of each wire and place at the end of the contact pad farthest from the film. The film was then heated to 80° C for one hour to finish the application of the epoxy (Fig. 2-3A). Vacuum films were then stored under inert conditions or their electrical properties were immediately measured.

2.4.3 Preparation of LB trough films, post-deposition

An alternative approach to prepare 2DM films was deposition *via* LB trough. I will describe briefly the relevant details, but I refer the reader to the dissertation of my colleague, Dr. Tyler Farnsworth from the Scott Warren lab, for an in-depth discussion on the preparation of 2DM films using the LB technique.

In general, suspensions of 2DM were deposited on the surface of the LB trough and compressed to form a homogenous film. A glass slide, oriented parallel to the surface of trough was then slowly pulled out of the trough. As the solvent evaporates, a homogenous film is deposited on the surface of the glass. The film is then annealed at 120 ° C under vacuum. This

process is considered one cycle of deposition. After annealing, the film can then be resubmerged for additional cycles and to prepare samples with a desired thickness. An additional challenge for this approach is that a flexible substrate is required to pressurize samples. To address this, we prewrapped glass slides with 0.5 in width PTFE tape (TaegaSeal). After the deposition cycles, the PTFE tape was easily unwound from the slide with the deposited 2DM film intact.

The 2DM films on PTFE were then carefully cut with scissors to be 3.0 mm by 3.0 mm and placed in the center of circular piece of insulating paper. To make electrical contacts to the film, 1.0 mm by 5.0 mm strips of copper foil backed with conductive adhesive were adhered to the corners of the film and extended to the edge of the paper. Finally, four nickel wires were attached to the contacts with silver epoxy or soldering, as described in the previous section (Figure 2-3B).

2.4.4 Electrical measurements on 2DM films with pressure and temperature control

Prior to electrical measurements, the 2DM films were placed within a hydraulic press. A pellet die was inverted to provide a pedestal (1.0 cm diameter) for samples to be placed and pressurized, while still being able to make electrical contacts to the extended nickel wires (Figure 2-4). The pressure of the sample could then be easily adjusted and recorded using the pressure gauge. To control the temperature of the sample, each component of the die was wrapped with a

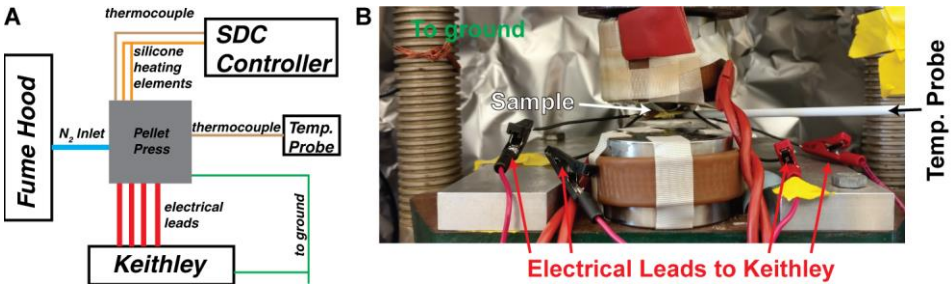

Figure 2-4. Uniaxial pressure and temperature controlled conductivity measurements: (A) Schematic for setting up a vdP measurement within a hydraulic press. **(B)** Picture within the aluminum-wrapped pellet press, showing sample placement, inverted pellet die, electrical leads, grounding, temperature probe, silicone heating elements. Not shown: thermocouple for SDC controller and N_2 inlet hose.

silicone heating tape (BriskHeat, 0.5 inches by 12 inches) and controlled with an SDC digital benchtop temperature controller. The digital controller thermocouple was placed between the silicone heating element and the die to correctly control the temperature of the system. Finally, an additional thermocouple was placed in contact with the pedestal, either directly above or below the sample, to accurately probe the temperature of the sample.

A Keithley 2636B Sourcemeter was used to make electrical measurements on 2DM films. The Sourcemeter was setup for four-point measurements with Channel A as the source (Sense Hi and Sense Lo ports) and Channel B acting as a voltmeter (Test Hi and Test Lo ports). Shielded Triax cables with adaptors to alligator leads were used to make connections to the nickel wires in a van der Pauw measurement geometry. The entire system was then double wrapped in aluminum foil to prevent the effects of stray electromagnetic fields during electrical measurements. Finally, a nitrogen line was passed through a desiccant and into the aluminum foil sample chamber to prevent undesired side reactions due to an applied bias.

Once the previous preparations were completed, a typical temperature- and pressure-dependent experiment was conducted in the following steps. (*i*) The SDC temperature controller was set to 90° C. (*ii*) Once the temperature of the sample has reached at least 70° C, the SDC controller is turned off. (*iii*) The sourcemeter is then turned on so that channel A is sourcing an appropriate voltage for the sample material and thickness, while channel B is forced to zero current. (*iv*) The current (channel A) and voltage (channel B) can then be taken at temperature intervals as the system is cools. (*v*) This process was repeated at different pressures using the hydraulic press. (*vi*) Finally, the film was removed and the thickness was measured using cross-

sectional SEM. (*vii*) Using the collected data and thickness, the conductivity and activation energy for charge transport can be calculated with Eqns. 2.8, 2.9 and 2.11 from section 2.3.1.

2.5 Application of DFT for 2D materials

Density functional theory has become a robust and quick computational tool to predict new materials and their optical, electrical, and physical properties. For exact solutions of the Schrödinger equation, there is the many-body problem of electron-electron interactions. To simplify this issue, density functional theory uses the ground state electron density to solve for the total energy of the system. This does not come without its limitations, since the use of electron density causes spurious self-interactions so that an exchange-correlation term must be included in the total energy. An appropriate exchange-correlation functional should always be considered depending on the system to be calculated, such as metals, semiconductors, or highly correlated materials.

It is not within the scope of this dissertation to provide an in depth discussion of the history and background of density functional theory, however I highly recommend reading "Density functional theory of atoms and molecules" by Robert G. Parr and Weitao Yang[16], "A Chemist's Guide to Density Functional Theory" by Wolfram Koch and Max C. Holthausen[17], and for a more solid state crystals perspective "Fundamentals of Semiconductor, Physical and Material Properties" by Peter Y. Yu and Manuel Cardona[18]. For future doctoral students who want to learn DFT independently, I would also suggest studying basic quantum mechanics. In this regard, the MIT Opencourseware lecture series by Prof. Allan Adams on Quantum Physics was a great resource for understanding the theory behind a DFT code, such as modeling potentials, fourier transforms, plane-wave cut off energies, etc. Finally, one of the most instructive methods I found to learn DFT was simply reading and replicating literature results. I

now describe the most relevant computational techniques and approaches that I used to study 2D materials and their heterostructures.

2.5.1 General methods using CASTEP

Density functional calculations were performed using the CASTEP[19] code with plane-wave basis set[20] approximations. Ultrasoft[21] pseudopotentials were used to describe core electrons, and a 600 eV cut-off energy was typically used. A GGA PBE functional[22] was used for the exchange-correlation contribution to total energy and Grimme's DFT-D[23] correction was used to account for long-range dispersion forces (see section 2.5.2 for additional details). A Monkhorst-Pack[24] grid corresponding to an inverse spacing of 0.02 1/Å between k-points was used. In order to calculate a 2DM of varying thickness, a periodic 12 Å vacuum slab was included in the unit cell to prevent self-interactions.

Prior to performing any geometry optimization or property calculations, it is extremely important to check for energy convergence. Internal energy minimization is done with an SCF loop with convergence set to 5.0×10^{-7} eV/atom and a window of three, however, external testing for convergence should always be performed. There are two important tests: (*i*) the plane-wave cut off energy should be increased in multiples of 25 eV while recording the total energy, E_{tot}. When the $dE_{tot}/d\ln E_{cut}$ is less than 0.01 eV/atom the calculation can be considered well converged. (*ii*) In a similar manner, the k-point mesh should be increased while monitoring E_{tot} until dE_{tot}/dk-point is less than 0.01 eV/atom.

Structures were optimized using a BFGS algorithm[25] with a convergence tolerance of 5.0×10^{-7} eV/atom for energy, 0.01 eV/Å for max force, 0.02 GPa for max stress, and 5.0×10^{-4} Å for max displacement. With an appropriate plane-wave cut off energy and k-point mesh as determined above, this usually resulted in structures with lattice constants within 1.0% of experimentally

determined values. For layered materials, it also important to include a semiempirical parameter to account for van der Waals forces. A discussion of Grimme's DFT-D correction is presented in section 2.5.2.

Once a structure was geometry optimized, a subsequent properties calculation could be performed to obtain the band structure, electron density, density of states, partial density of states, and optical properties. For these property calculations, an increased k-point mesh is required for greater accuracy, and therefore I used a 0.0025 1/Å k-point spacing. Furthermore, the number of conduction bands (referred to as extra bands in the Materials Studio and CASTEP interface) will also effect the accuracy of the result. Generally, I specified the number of conduction bands as 10*n*, where *n* is the number of atoms in the periodic cell. The exception for this relationship is optics calculations, which required at least 100*n* conduction bands.

2.5.2 Grimme's DFT-D correction for dispersion forces

It is well known that the LDA and GGA functionals of DFT will often inaccurately describe the long range intramolecular forces found in van der Waals (vdW) materials. To account for this, I used a semiempirical DFT-D with Grimme's dispersion correction to solve for the relaxed geometry and minimum energy of our bulk homogenous and heterogeneous layered systems[19, 23, 26]. The total energy now takes the form of:

$$E_{tot} = E_{DFT} + s_i \sum_{i=1}^{N} \sum_{j>1}^{N} f(S_R R_{ij}^0, R_{ij}) C_{6,ij} R_{ij}^{-6} \qquad (2.12)$$

Where E_{dft} is the typical energy calculated and is the sum of the kinetic (E_{kin}), electrostatic (E_{el}), and exchange-correlation (E_{xc}) components. The latter term of Eqn (1) accounts for long range forces between every pair of atoms, in which internuclear distance is R_{ij} and $C_{6,ij}R^{-6}_{ij}$ is the van der Waals coefficient describing the dispersion interaction. This interaction is modulated by a damping function, $f(S_R R^0_{ij}, R_{ij})$, with a cutoff at R^0_{ij}, the heteronuclear bond distance. Finally, the

scaling factors s_i and S_R are dependent on the dispersion scheme chosen: For Grimme's dispersion correction, s_i is equal to 0.75 and S_R is unity.

The geometry optimization of layered materials with van der Waals forces is drastically improved when Grimme's DFT-D correction is included. In general, the provided atomic vdW constants from CASTEP are sufficient to optimize structures with lattice constants typically within 2.0% of experimentally determined values, with greatest improvement in accuracy for interlayer distances. One exception is the optimization of graphite, in which I adjusted our vdW constant to 16.34 eV $Å^6$ to better describe the interaction of sp^2 hybridized carbon in graphite[27-28], resulting in an increase in interlayer distance, *d*, from 3.25 Å to 3.32 Å. This is in much closer agreement with experimentally determined values of 3.36 Å[29-30] and this vdW constant was used for all calculations involving multilayer or single layer graphite.

2.5.3 Binding energy, gravitational deformation and phonon modes for 2DM stability

From a thermodynamic perspective, 2DMs are a metastable phase of their parent layered material. In this regard, it can be difficult to predict whether a layered material can be exfoliated to the two-dimensional level. I here describe three critical analyses for the stability of a 2DM, including (*i*) binding energy calculations for interlayer interactions, (*ii*) the gravitational deformation of a 2DM as a freestanding material, and (*iii*) the application of phonon calculations as measure of stress on the 2DM.

(i) Binding energy:

The weak van der Waals forces in graphite result in an interlayer binding energy, E_{BE}, of 35 meV/atom[31]. Because E_{BE} is approximately equal to exfoliation energy, E_{ex}, its magnitude is often used as a metric to whether a layered material can be exfoliated. Advanced computational approaches using random phase approximation[32] have predicted the binding

energy for vdW layered materials to be 10-20 meV/Å^2. While there can be errors in the E_{BE} when calculated with a GGA PBE functional and Grimme's DFT-D corrections, it is qualitatively correct in determining structures and predicting trends. Therefore, I used binding energy calculations to determine the binding energy of new layered materials (black phosphorus, layered electrides) and in 2DM heterostructures (Chapter 5).

To calculate E_{BE}, we varied the interlayer distance between individual layers and then calculated the total energy. An 'infinite' structure was built with an interlayer distance of 12 Å, such that there were no interactions between sheets. We then calculated E_{BE} as:

$$E_{BE} = \frac{(E_{ild} - E_{\infty})}{n_{inter}} \quad (2.13)$$

where E_{∞} is the energy of the infinite structure, E_{ild} is the energy of the optimized structure, and n_{inter} is the number of atoms at the interface of two layers. Alternatively, E_{BE} can be calculated per unit area, and typically is reported as either meV/Å^2 or meV/atom.

(ii) Gravitational deformation of 2DM:

An important criterion for the stability of a 2DM is the ability to withstand its own weight. The processing of 2DM for electronic applications and optical measurement requires numerous lift-off and transfer steps, as well as the suspension of these materials as a membrane. The 2D Young's modulus of a 2DM can be calculated from an applied strain:

$$YM_{2D} = \frac{d^2 E_s}{d\epsilon^2} * A^{-1} \quad (2.14)$$

where E_s is the difference in energy between the optimized structure and the strained unit cell, Ɛ is the strain in a single lattice direction, and *A* is the area of the unit cell. Using the YM_{2D}, the deformation of a 2DM as a membrane can be calculated with Eqn 2.15.

$$\frac{h}{l} = \left(\frac{\rho g l}{YM_{2D}}\right)^{1/3} \quad (2.15)$$

where l is a lateral dimension of the suspended region, ρ is the density of the material, g is the gravitational force, and h is the deformation of the material in the z direction. It is expected that for a given l, the ratio h/l should be at least <0.001, implying the material can withstand its gravitational weight.

(iii) Phonon dispersions

A final technique to predict the stability of a 2DM is to calculate the phonon dispersions. Phonons are quantized vibrational modes of the atomic nuclei and can be either acoustic or optical. Since phonons are a physical process, they always have positive energies associated with their vibrational wavelength. The observation of negative phonons implies a material is unstable, and that a more stable phase can be found corresponding to the atomic displacements of the negative phonon.

I calculated the phonon dispersion of layered materials and 2DM using the finite displacement phonon property calculations with CASTEP. First, structures were geometry optimized to a higher degree of convergence than described in section 2.4.1. Particularly, energy, max stress, and max GPa tolerance were increased to 1×10^{-10} eV/atom, 0.001 eV/Å, and 0.001 GPa, respectively. A cutoff radius was chosen so that the supercell was at least four times the volume of the unit cell, in order to accurately model longer wavelength phonon modes. Phonon dispersion spectra were plotted along a Brillouin zone path encompassing the irreducible wedge, to account for phonon modes at all high symmetry points. The resulting phonon dispersions were then checked for negative phonon modes.

2.5.4 Self-interaction error and hybrid exchange functionals for accurate band gap determination of 2DMs

One of the most exciting features of 2DMs is the ability to control their optoelectronic properties with thickness. For example, black phosphorus has a band gap of 0.3 eV and 2.0 eV for bulklike and monolayer flakes, respectively. The accurate determination of band gap, as a function of thickness, is then very important for predicting the properties of a 2DM, however, it is well known that DFT will often undervalue the band gap due to the spurious self-interaction error[33]. This can be easily seen when solving for the coulomb forces of a one-electron density:

$$V^{el}[\rho] = \frac{1}{2}\int\int \frac{\rho(r_1)\rho(r_2)}{r_{12}} dr_1 dr_2 \neq 0 \qquad (2.16)$$

where $\rho(r_i)$ and $\rho(r_j)$ are two fragments of the electron density, and r_{ij} is the distance between them. Occupied states near the fermi level increase in energy, resulting in smaller apparent band gaps. The self-interaction error is also known to affect the activation energy for reactions[34] and charge transfer[35].

To account for the self-interaction error, an exact approach to the exchange energy, the Hartree-Fock method[36-38], can be calculated to cancel the coulomb interactions between an electron with itself. Despite this advantage, solving the HF energy can be computationally expensive and inaccurate for metallic systems, where electronic states tend to be highly delocalized. Therefore, hybrid functionals, such as HSE06[39] and PBE0[40], were empirically designed to include a 1:3 mixing of the Hartree Fock exchange energy with the PBE exchange-correlation energy. While LDA and GGA-PBE functionals are qualitatively correct, these functionals showed remarkably improved values for band gap, charge transfer, and optical properties.

When necessary, I used hybrid functionals to determine the band gap of 2D semiconductors or insulators. These calculations require norm-conserving pseudopotentials[41],

and a higher plane-wave cut off energy was increased to 900 eV for proper convergence. Typically a gamma-point energy calculation is sufficient, however, in my experience, a k-point mesh with a total of ~20 k-points can be solved within the three day time-limit of the Dogwood cluster at UNC. Finally, the electron minimization scheme must be set to All Bands/EDFT and is implemented by CASTEP from Marzari, *et al*[42].

2.5.5 Bader charge transfer in 2DM systems

Mulliken population analysis[43-44] can be used to assess the bonding and charge transfer in crystal systems. However, there can be large discrepancies between Mulliken charges calculated in CASTEP and experimental values. For example, in the ionic compound NaCl, actual atomic charges are close to ±0.8 e, while those reported from CASTEP are ±0.53 e. Henkelman and colleagues have developed a code to perform Bader charge analysis[45-48], which partitions the electron density using zero-flux boundaries and integrates the resulting Bader volumes. Indeed, Bader analysis shows remarkably improved results compared to Mulliken population analysis and I used this code to determine the charge transfer between electride and 2DM heterostructures (Chapter 5).

To perform a Bader analysis, first a standard CASTEP energy task calculation was performed, with the additional line "write_formatted_density : true" to the .param file to generate a .den_fmt file. Because the code is written for VASP and Gaussian output files, this .den_fmt file was rewritten to a .cube file using den2vasp. The output .castep from the energy calculation and corresponding .cube can then be analyzed with the Bader analysis code which was provided by the Henkelman group. The code was unpacked and compiled using GFortran for Windows. After the code has run, it is important to check the total integrated electron count and confirm that is with 0.0001 e of the initial CASTEP calculation. If there is an electron deficiency, the

plane-wave cutoff energy should be increased for a smaller tiling of the electron density and improved Bader volume partitioning and integration.

REFERENCES

1. Novoselov, K. S.; Geim, A. K.; Morozov, S. V.; Jiang, D.; Zhang, Y.; Dubonos, S. V.; Grigorieva, I. V.; Firsov, A. A., Electric field effect in atomically thin carbon films. *science* **2004,** *306* (5696), 666-669.

2. Coleman, J. N.; Lotya, M.; O'Neill, A.; Bergin, S. D.; King, P. J.; Khan, U.; Young, K.; Gaucher, A.; De, S.; Smith, R. J., Two-dimensional nanosheets produced by liquid exfoliation of layered materials. *Science* **2011,** *331* (6017), 568-571.

3. Hernandez, Y.; Nicolosi, V.; Lotya, M.; Blighe, F. M.; Sun, Z.; De, S.; McGovern, I.; Holland, B.; Byrne, M.; Gun'Ko, Y. K., High-yield production of graphene by liquid-phase exfoliation of graphite. *Nature nanotechnology* **2008,** *3* (9), 563.

4. Coleman, J. N., Liquid-phase exfoliation of nanotubes and graphene. *Advanced Functional Materials* **2009,** *19* (23), 3680-3695.

5. Coleman, J. N., Liquid exfoliation of defect-free graphene. *Accounts of chemical research* **2012,** *46* (1), 14-22.

6. Yi, M.; Shen, Z.; Zhang, X.; Ma, S., Achieving concentrated graphene dispersions in water/acetone mixtures by the strategy of tailoring Hansen solubility parameters. *Journal of Physics D: Applied Physics* **2012,** *46* (2), 025301.

7. Zhou, K. G.; Mao, N. N.; Wang, H. X.; Peng, Y.; Zhang, H. L., A mixed-solvent strategy for efficient exfoliation of inorganic graphene analogues. *Angewandte Chemie International Edition* **2011,** *50* (46), 10839-10842.

8. Berriman, J.; Bryan, R.; Freeman, R.; Leonard, K., Methods for specimen thickness determination in electron microscopy. *Ultramicroscopy* **1984,** *13* (4), 351-364.

9. Engel, A., Mass determination by electron scattering. *Micron (1969)* **1982,** *13* (4), 425-436.

10. Leapman, R.; Andrews, S., Characterization of biological macromolecules by combined mass mapping and electron energy-loss spectroscopy. *Journal of microscopy* **1992,** *165* (2), 225-238.

11. Maeyama, K.; Takaoka, A.; Ura, K., Effective thickness measurement of thin film for environmental cell by measuring electron transmissivity. *Microscopy* **1994,** *43* (1), 45-47.

12. Pozsgai, I., Thickness determination by measuring electron transmission in the TEM at 200 kV. *Ultramicroscopy* **1997,** *68* (1), 69-75.

13. Yang, Y.-Y.; Egerton, R., Tests of two alternative methods for measuring specimen thickness in a transmission electron microscope. *Micron* **1995,** *26* (1), 1-5.

14. Zeitler, E.; Bahr, G. F., A photometric procedure for weight determination of submicroscopic particles quantitative electron microscopy. *Journal of Applied Physics* **1962,** *33* (3), 847-853.

15. Van der Pauw, L., A method of measuring specific resistivity and Hall effect of discs of arbitrary shape. *Philips research reports* **1958,** *13*, 1-9.

16. Yang, W.; Ayers, P. W., Density-functional theory. In *Computational Medicinal Chemistry for Drug Discovery*, CRC Press: 2003; pp 103-132.

17. Koch, W.; Holthausen, M. C., *A chemist's guide to density functional theory*. John Wiley & Sons: 2015.

18. Yu, P. Y.; Cardona, M., *Fundamentals of semiconductors: physics and materials properties*. Springer: 1996.

19. Clark, S. J.; Segall, M. D.; Pickard, C. J.; Hasnip, P. J.; Probert, M. I.; Refson, K.; Payne, M. C., First principles methods using CASTEP. *Zeitschrift für Kristallographie-Crystalline Materials* **2005,** *220* (5/6), 567-570.

20. Kresse, G.; Furthmüller, J., Efficiency of ab-initio total energy calculations for metals and semiconductors using a plane-wave basis set. *Computational materials science* **1996,** *6* (1), 15-50.

21. Vanderbilt, D., Soft self-consistent pseudopotentials in a generalized eigenvalue formalism. *Physical Review B* **1990,** *41* (11), 7892.

22. Perdew, J. P., Density-functional approximation for the correlation energy of the inhomogeneous electron gas. *Physical Review B* **1986,** *33* (12), 8822.

23. Grimme, S., Semiempirical GGA-type density functional constructed with a long-range dispersion correction. *Journal of computational chemistry* **2006,** *27* (15), 1787-1799.

24. Monkhorst, H. J.; Pack, J. D., Special points for Brillouin-zone integrations. *Physical review B* **1976,** *13* (12), 5188.

25. Pfrommer, B. G.; Côté, M.; Louie, S. G.; Cohen, M. L., Relaxation of crystals with the quasi-Newton method. *Journal of Computational Physics* **1997,** *131* (1), 233-240.

26. Hohenberg, P.; Kohn, W., Inhomogeneous electron gas. *Physical review* **1964,** *136* (3B), B864.

27. Hasegawa, M.; Nishidate, K., Semiempirical approach to the energetics of interlayer binding in graphite. *Physical review B* **2004,** *70* (20), 205431.

28. Wu, Q.; Yang, W., Empirical correction to density functional theory for van der Waals interactions. *The Journal of chemical physics* **2002,** *116* (2), 515-524.

29. Baskin, Y.; Meyer, L., Lattice constants of graphite at low temperatures. *Physical Review* **1955,** *100* (2), 544.

30. Franklin, R. E., The structure of graphitic carbons. *Acta crystallographica* **1951,** *4* (3), 253-261.

31. Benedict, L. X.; Chopra, N. G.; Cohen, M. L.; Zettl, A.; Louie, S. G.; Crespi, V. H., Microscopic determination of the interlayer binding energy in graphite. *Chemical Physics Letters* **1998,** *286* (5-6), 490-496.

32. Björkman, T.; Gulans, A.; Krasheninnikov, A. V.; Nieminen, R. M., van der Waals bonding in layered compounds from advanced density-functional first-principles calculations. *Physical review letters* **2012,** *108* (23), 235502.

33. Marsman, M.; Paier, J.; Stroppa, A.; Kresse, G., Hybrid functionals applied to extended systems. *Journal of Physics: Condensed Matter* **2008,** *20* (6), 064201.

34. Zhao, Y.; Lynch, B. J.; Truhlar, D. G., Development and assessment of a new hybrid density functional model for thermochemical kinetics. *The Journal of Physical Chemistry A* **2004,** *108* (14), 2715-2719.

35. Laricchia, S.; Fabiano, E.; Sala, F. D., Semilocal and hybrid density embedding calculations of ground-state charge-transfer complexes. *The Journal of chemical physics* **2013,** *138* (12), 124112.

36. Roothan, C., Hartree Fock theory. *Reviews of Modern Physics* **1951,** *23*, 69.

37. Pople, J.; Nesbet, R. K., Self-consistent orbitals for radicals. *The Journal of Chemical Physics* **1954,** *22* (3), 571-572.

38. McWeeny, R.; Diercksen, G., Self-Consistent Perturbation Theory. II. Extension to Open Shells. *The Journal of Chemical Physics* **1968,** *49* (11), 4852-4856.

39. Krukau, A. V.; Vydrov, O. A.; Izmaylov, A. F.; Scuseria, G. E., Influence of the exchange screening parameter on the performance of screened hybrid functionals. *The Journal of chemical physics* **2006,** *125* (22), 224106.

40. Adamo, C.; Barone, V., Toward reliable density functional methods without adjustable parameters: The PBE0 model. *The Journal of chemical physics* **1999,** *110* (13), 6158-6170.

41. Lin, J.; Qteish, A.; Payne, M.; Heine, V., Optimized and transferable nonlocal separable ab initio pseudopotentials. *Physical Review B* **1993,** *47* (8), 4174.

42. Marzari, N.; Vanderbilt, D.; Payne, M. C., Ensemble density-functional theory for ab initio molecular dynamics of metals and finite-temperature insulators. *Physical review letters* **1997,** *79* (7), 1337.

43. Segall, M.; Pickard, C.; Shah, R.; Payne, M., Population analysis in plane wave electronic structure calculations. *Molecular Physics* **1996,** *89* (2), 571-577.

44. Segall, M.; Shah, R.; Pickard, C.; Payne, M., Population analysis of plane-wave electronic structure calculations of bulk materials. *Physical Review B* **1996,** *54* (23), 16317.

45. Henkelman, G.; Arnaldsson, A.; Jónsson, H., A fast and robust algorithm for Bader decomposition of charge density. *Computational Materials Science* **2006,** *36* (3), 354-360.

46. Sanville, E.; Kenny, S. D.; Smith, R.; Henkelman, G., Improved grid-based algorithm for Bader charge allocation. *Journal of computational chemistry* **2007,** *28* (5), 899-908.

47. Tang, W.; Sanville, E.; Henkelman, G., A grid-based Bader analysis algorithm without lattice bias. *Journal of Physics: Condensed Matter* **2009,** *21* (8), 084204.

48. Yu, M.; Trinkle, D. R., Accurate and efficient algorithm for Bader charge integration. *The Journal of chemical physics* **2011,** *134* (6), 064111.

CHAPTER THREE – PHOSPHORENE: SYNTHESIS, CHARACTERIZATION, AND QUANTITATIVE OPTICAL SPECTROSCOPY[1]

*Adam H. Woomer[§#], Tyler W. Farnsworth[§#], Jun Hu[§], Rebekah A. Wells[§], Carrie L. Donley[‡], and Scott C. Warren[§†]**

[§]Department of Chemistry, [‡]Chapel Hill Analytical and Nanofabrication Laboratory, and [†]Department of Applied Physical Sciences, University of North Carolina at Chapel Hill, Chapel Hill, NC 27599, USA.

[#]These authors contributed equally.

3.1 Introduction

Solution-processable nanomaterials with tunable optoelectronic properties are being considered as potential building blocks for numerous technologies, such as photovoltaics,[1] transistors,[2] and light-emitting diodes.[3] Among these nanomaterials, quantum dots have attracted broad interest because of their size-dependent electronic structure and controllable physical properties; for example, band gaps can be increased by as much as 2 eV as particle size decreases.[4–7] With the advent of two-dimensional (2D) semiconductors,[8] new opportunities have emerged for designing materials and devices, although the size-dependent variation of electronic properties like band gaps are, in general, smaller: transition metal dichalcogenides have band gaps that can only be tuned by 0.7 eV[9,10] while, for example, PbSe quantum dots can be tuned

[1]Reprinted (adapted) with permission from Woomer, A. H. *et al.* Phosphorene: Synthesis, Scale-Up, and Quantitative Optical Spectroscopy, *ACS Nano*, **2015,** *9*, 8869-8884. Copyright (2015) American Chemical Society.

from 0.27 to 1.5 eV.[11–13] Toward increasing the library of solution-processable materials, here we show that black phosphorus can be liquid exfoliated to yield a family of 2D flakes with tunable optical properties that rival those of quantum dots.

Black phosphorus,[14] a layered 3D crystal of elemental phosphorus (Figure 1a), and its 2D derivative, termed phosphorene[15,16] (Figure 1b), have recently attracted renewed[17] attention. In the last few months, there have been exciting demonstrations of the material's application to transistors,[16,18,19] photovoltaics,[20,21] photodetectors,[22,23] and batteries.[24,25] As a 2D material with an intriguing corrugated or accordion-like structure, phosphorene has captured significant theoretical interest with numerous predictions of the material's anisotropic[16,26] and thickness-dependent optoelectronic properties,[27,28] mechanical properties,[29] and chemical reactivity.[30–32] Most predictions have gone untested, however, because there is still no reliable method to make or purify monolayer or few-layer phosphorus. When monolayers have been observed, they are typically situated at the edges of thicker sheets and are typically too small to characterize. Underlying these practical challenges are the inherent problems associated with phosphorus: the phosphorus-phosphorus bonds are significantly weaker than carbon-carbon bonds and several studies have noted the material's tendency to oxidize[14,33] or form other allotropes.[34,35] In addition, interlayer interactions may be stronger in black phosphorus than in other 2D materials.[36,37] These strong interlayer interactions would inhibit exfoliation and, consequently, black phosphorus may be harder to exfoliate and more likely to fragment than other 2D materials. In fact, this is consistent with reports of mechanical exfoliation in which sheets of fewer than six layers have seldom been observed.[16,18,19,38,39]

Our own attempts to mechanically exfoliate black phosphorus confirmed the results of other groups. We prepared and analyzed samples under an inert atmosphere, using scotch tape

for exfoliation and a Bruker Dimension FastScan atomic force microscope (AFM) to rapidly analyze sheet thickness over macroscopic areas (see Supporting Information for additional details). We randomly surveyed large areas and assessed the structure of over 3,000 flakes. Our survey revealed that the yield of sheets thinner than 10 layers is less than 0.06%; in addition, no sheets thinner than 6 layers were found. Given the low odds for identifying and characterizing 2D materials prepared in this way, we began exploring liquid exfoliation[40,41] as an alternative route for material preparation. Here we provide evidence that liquid exfoliation, when carefully executed under an inert atmosphere, produces macroscopic (milligram-to-gram scale) quantities of monolayer and few-layer phosphorene.[42] We note that this is a considerable improvement over state-of-the-art methods of liquid exfoliation,[43–45] which have so-far produced flakes with thicknesses that are 10 to 20 times thicker than those described here. We characterize the material's structure, stability, and thickness-dependent optical properties and compare these properties to theoretical predictions. In addition, we perform the first quantitative optical absorption measurements on 2D phosphorus, allowing us to determine the thickness-dependent optical transitions and band gaps.

3.2 Liquid exfoliation of black phosphorus

Black phosphorus crystals (Figure 3-1a) were acquired from Smart Elements between December 2012 and March 2014 or grown in our laboratory by SnI_2 vapor transport.[46] (Smart Elements modified its method of manufacture in the summer of 2014 and the microstructures of materials acquired after this date may differ.) Black phosphorus was ground in a mortar and pestle and sonicated in anhydrous, deoxygenated organic liquids using low-power bath sonication under an inert atmosphere. In our initial experiments, black phosphorus was sonicated in electronic grade isopropanol for sixteen hours. During sonication, the phosphorus

was suspended in solution and its color changed from black to reddish-brown to yellow (Figure 3-1c), indicating a profound change in the electronic structure of the material. We quantified this change in appearance by ultraviolet-visible-near IR (UV-vis-near IR) absorption spectroscopy (see discussion below for further details). Over several weeks, there was limited reaggregation and no further change in color, suggesting that these suspensions were comprised of small phosphorus particulates. To examine the morphology of the particulates, suspensions were drop-cast onto a silicon wafer for analysis by scanning electron microscopy (SEM, Figure 3-1d). These images confirmed the presence of thin phosphorus flakes with lateral dimensions between 50 nm and 50 μm. From these results, we concluded that a more extensive study was required to identify conditions that maximized the yield of thin phosphorus flakes.

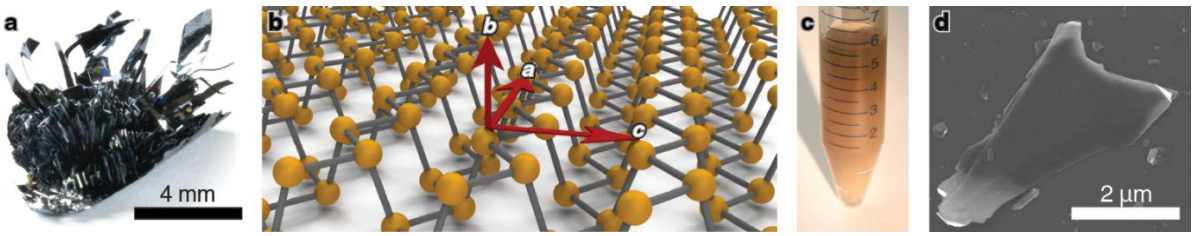

Figure 3-1. Liquid exfoliation of black phosphorus: (A) Photograph of black phosphorus grown by chemical vapor transport. **(B)** Illustration of a phosphorene monolayer showing the conventional crystallographic axes. The zig-zag direction is 'a', the armchair direction is 'c', and the 'b' direction is normal to the flake. **(C)** Photograph of a liquid-exfoliated suspension of 2D phosphorus in isopropanol. **(D)** SEM image of liquid-exfoliated 2D phosphorus.

We surveyed[42] eighteen solvents for their ability to exfoliate black phosphorus (see Supporting Information for full experimental details). Black phosphorus (10 mg) was added to 20 mL of each solvent and sonicated for thirteen hours under anhydrous and air-free conditions. The suspensions were centrifuged at 3,000*g* for 30 minutes to remove unexfoliated black phosphorus. The supernatant was further purified *via* dialysis to remove small (< 2.5 nm) phosphorus fragments. These suspensions were characterized with inductively coupled plasma-

mass spectroscopy (ICP-MS) and UV-vis transmission spectroscopy to measure a dispersed concentration. We found that the best solvent was benzonitrile, which achieved a mean concentration of 0.11 ± 0.02 mg/mL. Plots of phosphorus concentration *vs*. the Hansen solubility parameters of each solvent (Figure 3-2a-d) allow us to estimate that the Hildebrand parameter for 2D phosphorus is 22 ± 3 $MPa^{1/2}$. Although there is significant solvent-to-solvent variability—a

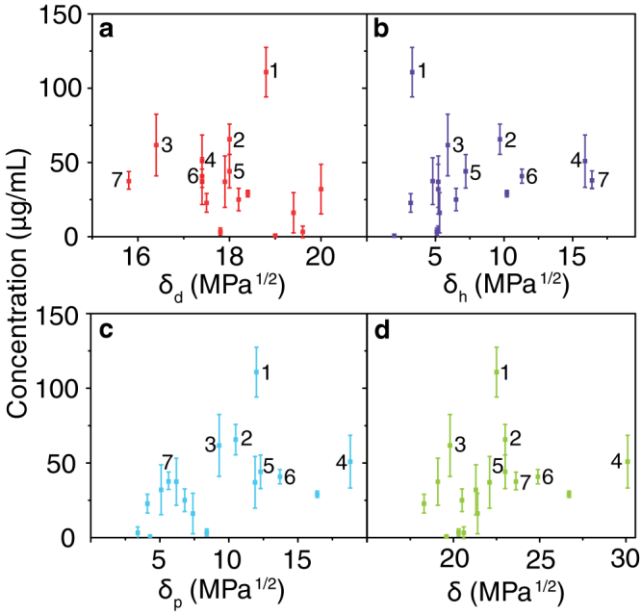

Figure 3-2. Survey of organic liquids for liquid exfoliation of black phosphorus: showing 2D phosphorus concentrations *vs*. Hansen **(A-C)** and Hildebrand **(D)** solubility parameters for 18 solvents. The Hansen plots depict the energy due to dispersion forces **(A)**, hydrogen bonding **(B)**, and dipolar intermolecular forces **(C)**. Numbers 1 through 7 rank the best liquids: (1) benzonitrile, (2) 1,3-dimethyl-2-imidazolidinone, (3) 1-vinyl-2-pyrrolidinone, (4) *N*-methylformamide, (5) *N*-methyl-2-pyrrolidone, (6) *N*,*N*-dimethylformamide, (7) 2-propanol. Each data point is an average of three trials; the error bars correspond to the standard deviation.

feature common to graphene, boron nitride, and transition metal dichalcogenides[41]—we find that the optimal solvents for 2D phosphorus are similar to those for other 2D materials. An essential difference, however, is that 2D phosphorus must be handled and sonicated under an inert atmosphere, as we demonstrate below.

3.3 Characterization of 2D phosphorus

In order to examine the structure of the suspended material, we used transmission electron microscopy (TEM) to quantify shape, size, and thickness as well as high resolution TEM (HR-TEM) to assess crystallinity. We imaged and measured thousands of phosphorus flakes; Figure 3-3a-c shows TEM images of several representative samples. As before, a broad distribution of flake sizes was found. Single pieces typically had uniform contrast, suggesting that they had a planar morphology. All of the pieces examined in HR-TEM exhibited lattice fringes, showing that the crystallinity of phosphorus flakes was preserved (Figure 3-3d). We analyzed HR-TEM images by performing fast Fourier transforms (FFT), allowing us to observe the expected {200} and {002} plane families of black phosphorus. In addition, some flakes exhibited strong 101 intensities (Figure 3-3e), which are forbidden sets of diffracting planes in bulk black phosphorus. To understand the origin of the 101 spots, we used multi-slice calculations (JEMS[47]) to simulate HR-TEM images of 2D phosphorus sheets with varying thicknesses from four common microscopes (see Supporting Information for additional details). Fast Fourier transforms were applied to the HR-TEM images to determine the intensities of spots corresponding to plane families. In agreement with a previous analysis of electron diffraction patterns,[28] we found that a large 101:200 intensity ratio in FFTs is a unique characteristic of monolayers (Figure 3-3f) when imaged at or near Scherzer defocus, thus confirming their presence in our suspensions. We attribute the diffuse background of the FFT (Figure 3-3e) to the likely presence of absorbed organics, which has been observed previously for other 2D materials that were not degassed at elevated temperatures prior to imaging.[48,49]

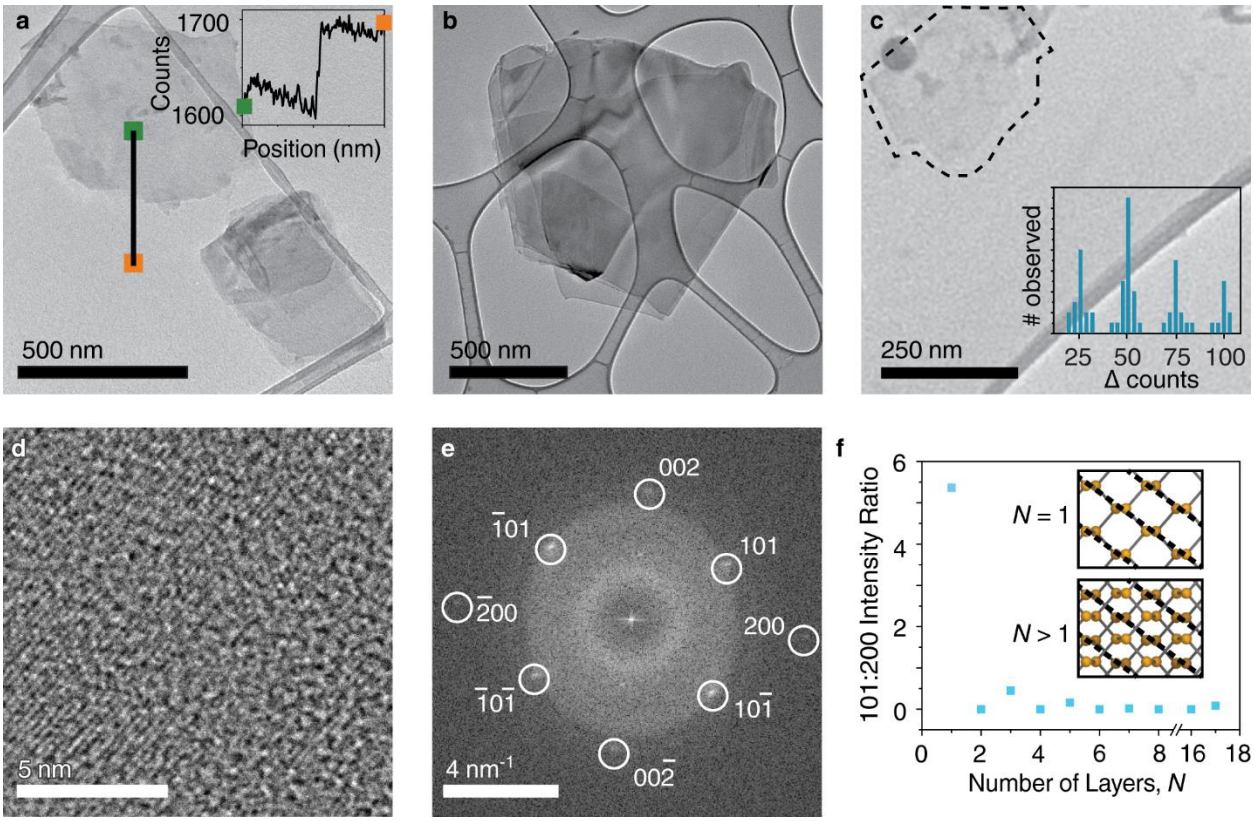

Figure 3-3. TEM characterization of liquid-exfoliated 2D phosphorus: (A-C) TEM images of 2D phosphorus. **(C)** TEM image of a monolayer of 2D phosphorus. The inset in **(A)** shows the contrast change (*ca.* 75 counts) from a line profile drawn across a flake that is three layers thick. The inset in **(C)** provides a histogram of contrast changes from one hundred flakes. The changes in intensity (25, 50, *etc*.) correspond to monolayers, bilayers, *etc*. **(D)** HR-TEM image of phosphorene, a monolayer. **(E)** FFT of the HR-TEM image in **(D)**. **(F)** Intensity ratios of 101 and 200 spots in FFT HR-TEM images and their relation to layer thickness, as calculated from multi-slice simulations in JEMS.[47] Insets show that constructive interference from {101} plane families (dashed lines) occur in monolayers but have low or no intensity in multilayer flakes.

To quantify the thickness of all flakes in our suspensions, we used our real-space TEM images—all acquired under identical imaging conditions including exposure time, aperture selection, lens currents, magnification and defocus value—to measure the change in intensity across sheet edges for hundreds of flakes (Fig 3-3a, line and inset). Flake edges were suspended over either vacuum or carbon film (see Section 2.3.1 for additional details). The smallest intensity change was 25 ± 3 counts and all other intensity changes were multiples of 25 counts

(Figure 3-3c, inset). We therefore assigned an intensity change of 25, 50, 75, and 100 counts to monolayers, bilayers, trilayers, and four-layered 2D phosphorus flakes, respectively. Further confirming this assignment, we found that only those flakes with a contrast change of *ca.* 25 counts had the intense 101 spots that are a hallmark of monolayers. Although this method is simple and fast, we do note that the linear relationship breaks down for flakes that are thicker than *ca.* 40 layers.

With the goal of isolating 2D flakes with well-defined thicknesses and optical properties, we used centrifugation to fractionate the phosphorus suspensions. We centrifuged at a rotational centrifugal force (RCF) as low as 120*g* and then centrifuged the supernatant at a slightly greater RCF, reaching values of up to 48,000*g*. The sediment from the second centrifugation was collected and re-dispersed in pure solvent. This new suspension is labeled by the average centrifugal force between the two RCFs; for example, a suspension labeled 20,200*g* has been centrifuged at 17,200*g* and 23,400*g* (see Section 2.2.2 for full experimental details). Using TEM, we analyzed the thicknesses (Figure 3-4a) lateral size (Figure 3-4b) and of the suspended 2D phosphorus flakes. We found that this centrifugation approach could systematically isolate flakes with varying size and thickness distributions. When centrifuging at high speeds, for example, we collected macroscopic quantities of flakes with size distributions centered near one-layer and two-layer thicknesses (Figure 3-4a) in which monolayers comprised up to 45% of the sample. Phosphorene—a material that has been sought after but rarely observed—is now easily accessible.

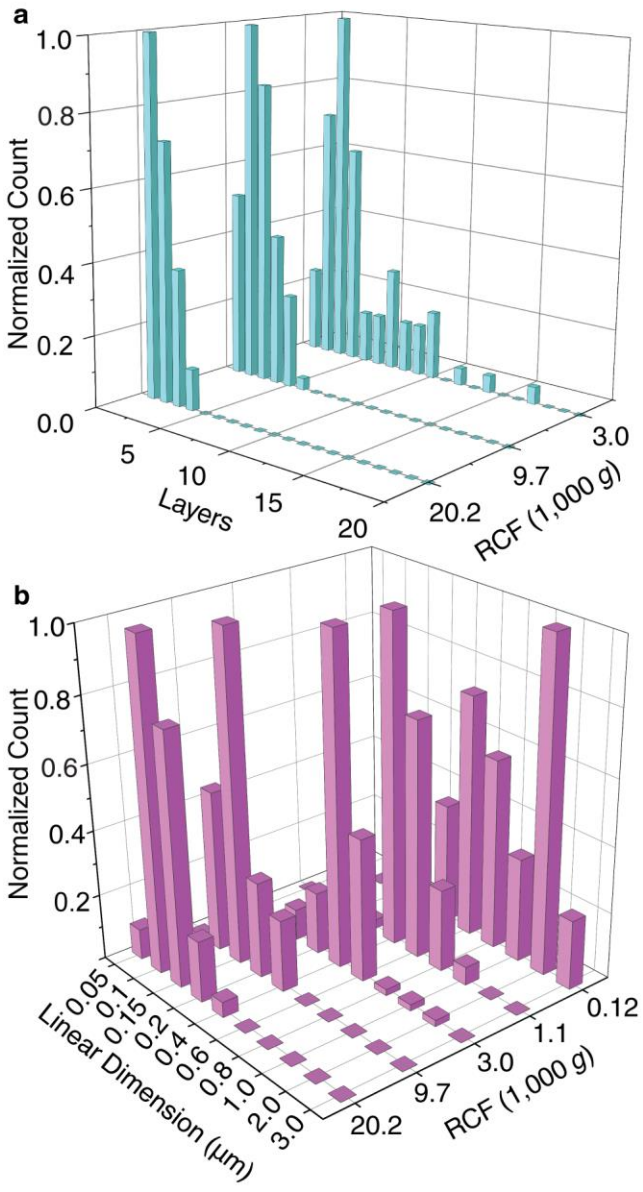

Figure 3-4. Centrifugation rate to control thickness and lateral size: (A) thickness and **(B)** flake lateral size.

Stability of phosphorene and 2D phosphorus

As first recognized by Bridgman in 1914,[(ref. 14)] black phosphorus oxidizes and converts to phosphoric acid under humid atmospheric conditions. More recent studies have also shown that mechanically-exfoliated phosphorus degrades in air.[19,28,32] We used x-ray photoelectron

spectroscopy (XPS) and measurements of apparent pH to assess the oxidation. We performed XPS both on bulk black phosphorus to obtain a reference spectrum (Figure 3-5a) and on 2D phosphorus to test whether oxidation accompanies liquid exfoliation (Figure 3-5b). In addition to performing all exfoliation and centrifugation under an inert atmosphere, we constructed a transfer chamber that excluded oxygen and water during sample transfer to and from the XPS instrument. Pristine black phosphorus had $2p_{1/2}$ and $2p_{3/2}$ peaks that are characteristic of unoxidized elemental phosphorus.[50] We exposed the same sample to air and re-acquired XPS spectra at later time intervals. A broad peak at 134 eV emerged, which can be attributed to several types of phosphorus-oxygen bonds.[51] Lacking an oxidation mechanism, we cannot yet identify the type or types of P-O species that may be present in our samples. We performed similar experiments on thin 2D phosphorus (< 6 layers). The pristine sample exhibited no signs of oxidation (Figure 3-5b, black). Upon exposure to oxygen gas that contained some water (not dried) and 460 nm light, a broad peak appeared at 133 eV, characteristic of oxidized phosphorus. In this modified material, *ca.* 5% of the phosphorus was oxidized, as estimated by peak integration software. Collectively, our analyses demonstrate that liquid exfoliation successfully yields high-quality, unoxidized 2D phosphorus.

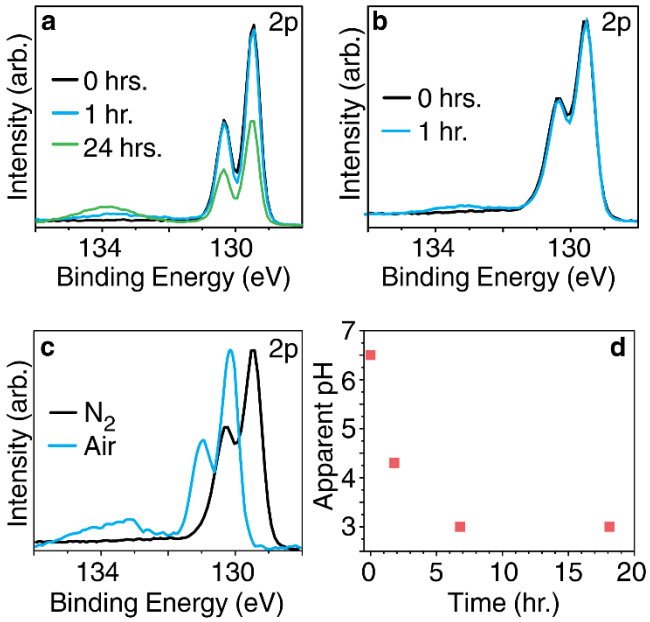

Figure 3-5. Oxidation studies of Black Phosphorus: (A) XPS of freshly cleaved bulk black phosphorus after exposure to ambient air and room light for 0 (black), 1 (blue), and 24 (green) hours. **(B)** XPS analysis of few-layer 2D phosphorus showing that the material prepared by liquid exfoliation was unoxidized (black). The few-layer sheets were controllably oxidized by exposure to light ($\lambda = 460$ nm) and oxygen with some water (blue). **(C)** Exfoliation of black phosphorus in a sealed vial with N_2 (black) or air (blue) in the head space of the vial shows that the presence of air causes 28% of the phosphorus to become oxidized. Binding energies also increase, although the origin of this effect—whether sample charging, doping, or both—is not yet clear. **(D)** When few-layer 2D phosphorus (< 6 layers) is suspended in isopropanol and exposed to light and air ($\lambda = 460$ nm), the apparent pH (recorded by a pH meter) decreases because of acid production.

In order to evaluate whether handling under an inert atmosphere is important, we sonicated black phosphorus in a sealed vial, with either nitrogen or air in the vial's headspace. Analysis of the air-exposed material by XPS (Figure 3-5c) shows substantial oxidation, with 28% of the phosphorus no longer in the unoxidized form. In addition, we monitored the pH of a solution of few-layer phosphorus that was suspended in isopropanol and exposed to light and air (Figure 3-5d). We found that the solution rapidly acidifies, consistent with Bridgman's prediction[14] that phosphoric acid is produced upon exposure to air. When higher phosphorus concentrations are used, the apparent change in pH is larger. On the basis of these and prior

findings,[43] we conclude that although liquid exfoliation in the presence of air may produce some crystalline, thin material, its surfaces and interior[52] are oxidized, acid is present, and its overall quality is low.

3.4 Exfoliation of black phosphorus at the 10-gram scale

We explored shear mixing[42,53] as a method for the scaled-up production of 2D phosphorus. We used a Silverson L5M-A shear mixer with either a 0.75-inch or 1.385-inch rotor with square holes for our work at the 1-gram and 10-gram scales, respectively. All experiments were performed under oxygen-free and water-free conditions by bubbling nitrogen gas into the mixing container. In addition, we used a water bath to keep the solutions at room temperature during mixing. We used several different grades of NMP, as it was disclosed to us by the Coleman group that only certain types of NMP may work for shear mixing of graphene.[54] Ultimately, we selected NMP from Sigma Aldrich (99.5% purity, anhydrous) for our scaled-up exfoliation. Black phosphorus was ground in a mortar and pestle prior to its use in shear mixing. We used two different grades of black phosphorus, both of which we produced in our laboratory. The first, "high quality" black phosphorus, was highly crystalline with millimeter-sized crystals and was difficult to grind; the second, "low quality" black phosphorus, was highly polycrystalline, had trace amounts of red phosphorus, and was easy to grind. In our experiments, we found that only the low-quality material could be successfully exfoliated by shear mixing alone, regardless of the type of NMP or the conditions of shear mixing. This observation is consistent with a mechanism in which the separation of layers is nucleated at grain boundaries or other defects in the material. In order to exfoliate the higher-quality starting material, we had to rely on a combination of shear mixing and bath sonication.

For our scaled-up synthesis, we dispersed 6 grams of pulverized, high-quality black phosphorus into 100 mL of NMP and bath sonicated the suspension for 2 hours. Next, we added 700 mL of NMP and shear mixed the sample at 5,000 rpm for 4 hours. The dispersion was sonicated again for 3 hours and then shear mixed again for 1 hour at 5,000 rpm. The resulting suspension is shown in Figure 6a. The material was then centrifuged at 20,200*g* to yield a highly concentrated suspension of very thin, fractionated material (Figure 3-6a, small vial). In this suspension, nearly 25% of the sample was monolayers (Figure 3-6b) and the lateral size (Figure 3-6c) was similar to the material produced using bath sonication at a smaller scale (Figure 3-4). This demonstration reveals that the production of high quality 2D phosphorus—including phosphorene—can be readily accomplished using simple and scalable approaches.

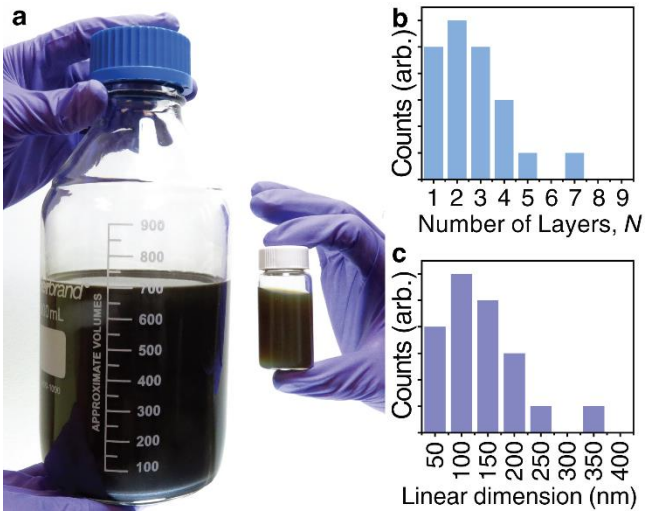

Figure 3-6. Scaled-up production of 2D phosphorus: (A) Photograph of solutions that were exfoliated using a combination of shear mixing and sonication. In our scale-up, we used six grams of black phosphorus and 800 mL of NMP (left). We centrifuged 40 mL of this mixture at 20,200*g* to isolate a highly concentrated suspension containing thin pieces (right). The size distribution of 2D phosphorus in this fraction is shown in **(B)** and **(C)**.

3.5 Optical absorption in 2D phosphorus: background

The optoelectronic properties of black phosphorus and 2D phosphorus—high mobility, anisotropy and the extreme variation in band structure with flake thickness—have provoked intense interest and debate. In 1981, a calculation first proposed the idea of a monolayer of black phosphorus[55] (*i.e.*, phosphorene) and calculated a band gap of 1.8 eV, which is significantly larger than the bulk value of 0.33 ± 0.02 eV (see below for discussion). This remarkable prediction was dormant until several months ago, when the possibility of making phosphorene began to emerge. Despite this interest, the synthesis of monolayers has remained a challenge and, consequently, the majority of recent studies have been theoretical. These studies have essentially confirmed the 1981 prediction—that the band gap is tunable—although they have also introduced considerable uncertainty as to the actual size of the gap: values for monolayers typically range from 1.0 to 2.2 eV (see Table 3-1). Nevertheless, theory consistently predicts that the band gap is direct for all thicknesses of 2D phosphorus, which has driven further interest because most other 2D semiconductors have indirect band gaps.

These predictions are compelling and need to be systematically examined but, so far, only a few experiments have been reported. Photoluminescence measurements have shown that these predictions are qualitatively correct, but with a varying exciton binding energy of 0.01 to 0.9 eV in phosphorene, this technique will underestimate the band gap of black phosphorus by a similar amount, which depends on the static dielectric constant of the surrounding medium.[56–58] In addition, surface defects, contamination, and oxidation of samples may introduce further experimental uncertainty. In fact, results so far are quite varied: in one study, a trilayer photoluminesced at 1.60 eV, while, in another, the measured value was 0.97 eV (see optical gaps, Table 1). Electrical measurements have also been performed and the reported mobility

gaps were smaller than those found by photoluminescence (see mobility and optical gaps, Table 1), a result that is surprising because the mobility gap should be larger than the optical gap in a semiconductor with few interband states.[59,60] However, the study did provide a detailed analysis of many flake

Table 3-1. Reported optical, mobility, and band gaps of 2D phosphorus:

Thickness (layers)	**1**	**2**	**3**	**4**	**Bulk**	**Source**
Photoluminescence (optical gap, eV)	1.75	1.29	0.97	0.84		Yang, J.[61]
	1.45					Liu, H.[16]
	1.31					Wang, X.[62]
		1.29	0.98	0.88		Zhang, S.[63]
			1.60			Castellanos-Gomez, A.[28]
Electrical (mobility gap, eV)	0.98	0.71	0.61	0.56	0.30	Das, S.[64]
Computation (band gap, eV)	2.15	1.70	1.48	1.36	1.08	Castellanos-Gomez, A.[28]
	2.0	1.30	1.06		0.30	Tran, V.[37]
	1.94	1.7	1.3	0.8	0.43	Liang, L.[65]
	1.60	1.01	0.68	0.46	0.10	Rudenko, A.[66]
	1.52	1.01	0.79	0.67	0.36	Qiao, J.[67]
	1.01	0.66	0.52	0.47	0.31	Liu, H.[16]
		1.02	0.79	0.68		Zhang, S.[63]
Absorbance (band gap, eV)		1.88	1.43	1.19	0.33	This work, see Table 3-2.

thicknesses, and revealed that bulk properties begin to transition towards quantum-confined properties at flake sizes as large as 30 layers.

In this section, we report our experiments on the optical absorbance of black phosphorus and fractionated suspensions of 2D phosphorus. We also report our analyses of these spectra, from which we estimate the absorption edge and band gap in black phosphorus and 2D phosphorus. Some of our analysis uses Elliot's theory of light absorption[68] by delocalized, Wannier-type excitons,[69] and we implement Elliot's theory in the form of Tauc plots.[70] Tauc plots determine the band-to-band transition energy as well as the nature of the transition—whether it is phonon-mediated (indirect) or not (direct), and whether it is dipole-mediated (allowed) or not (forbidden). A proper Tauc plot yields a linear relationship between $(\alpha h\nu)^n$ and hν, where α is the absorption coefficient, hν is the photon energy, and n describes the nature of the transition. Although Tauc plots have been criticized because of their simplistic assumptions about band structure and their poor treatment of excitonic effects,[56] they have been used to analyze the absorption edge of many semiconductors, including black phosphorus.[71] In a reported Tauc analysis of black phosphorus, a room-temperature band gap of 0.31 eV was found.[71] This agrees with previously reported electrical measurements,[17,72–76] which we have averaged to calculate a room-temperature band gap of 0.33 ± 0.02 eV. Although this agreement is promising, there are important differences between our 2D samples and bulk black phosphorus that may prevent the application of Tauc's method to our materials. Next, we consider these differences and the corresponding limitations of Elliot's theory.

We have identified five possible reasons why a Tauc analysis could fail to apply to our 2D phosphorus suspensions.

(1) *Light scattering:* A Tauc analysis requires an accurate measurement of the absorption coefficient, α, *versus* wavelength. We measured light that is absorbed by our suspensions of 2D phosphorus using a transmission geometry, but in a traditional transmission geometry, most scattered light is not captured by the detector. To account for forward-scattered light, we placed samples near the opening aperture of an integrating sphere. This measurement showed that the amount of forward-scattered light was relatively small. In addition, because there is less back-scattered light than forward-scattered light,[77] we estimated that our measurements that capture both the transmitted and forward-scattered but neglect back-scattered light have less than a 3% error (see Supporting Information for complete details). Consequently, we have reported an absorption coefficient rather than an extinction coefficient.

(2) *Exciton binding energy:* Elliot's theory is only applicable to Wannier excitons, which have an exciton binding energy (EBE) of less than 100 meV. Bulk black phosphorus has an EBE of 8 meV and the excitonic features in absorbance spectra are only apparent at low temperature.[17] The predicted EBE of phosphorene (a monolayer) depends on the static dielectric constant of the surrounding medium, and can be as large as 900 meV in a vacuum.[28,37] We performed most optical absorbance experiments in NMP, which has a high dielectric constant (32.17) and yields a small EBE (15 meV, see Supporting Information). The small EBEs, combined with the measurement of our absorbance spectra at room temperature and low light intensities, allows Elliot's theory to be applied because excitons will not obscure the absorption edge as they do in MoS_2 and other transition metal chalcogenides.

(3) *Urbach tail:* In materials with significant structural disorder, a pronounced absorption extends below the absorption edge.[78] This absorption, called an Urbach tail, could be present in 2D phosphorus because of the loss of periodicity and presence of defects at the edge of sheets. Urbach tails give a non-linear contribution to Tauc plots. To avoid misinterpreting our spectra, we only extracted an estimate of the band gap when a linear fit of the Tauc plot was obtained at energies above the Urbach tail.

(4) *Anisotropic optical properties:* The nature of black phosphorus' band gap depends on direction: it is direct and allowed in the ***c*** direction but direct and forbidden in the ***a*** direction (see Figure 1b).[17] In principle, this would prevent a Tauc plot from distinguishing either transition. Fortunately, the forbidden transition is relatively weak and its contribution to light absorption is negligible;[17] thus, it does not obscure the Tauc analysis of the direct, allowed band gap.

(5) *Variation in band gap:* Tauc analyses are typically applied to materials with a single band gap. If multiple gaps are present and they span a narrow range of energies, it is not possible to distinguish each gap. The superposition of multiple absorption edges of similar strength leads to non-linearity in the Tauc plot, preventing one from determining the nature of the absorption edge or from extracting an accurate band gap energy. Of the five limitations, we found that this consideration is the most important. Our suspensions contain flakes of several thicknesses and therefore several band gaps. Because the absorption coefficients from flakes of different thicknesses are similar and because their band gaps fall across a range of energies, we found that it is not always possible to use a Tauc analysis (see below). In those instances, we have developed and applied a different method for estimating the absorption edge.

3.6 Optical absorption in 2D phosphorus: measurement and Tauc analysis

In this section, we report our measurement and Tauc analyses of the optical absorbance of 2D phosphorus suspensions. In order to interpret these measurements, we first established reference spectra of bulk black phosphorus. We performed UV-vis-nIR (175 nm to 3,300 nm) and FT-IR measurements on a polycrystalline sample (KBr pellet, Figure 3-7a, black) and used a CRAIC microspectrophotometer on single flakes of mechanically cleaved bulk crystals (Figure 3-7a, gray). All spectra were acquired under an inert atmosphere. Fractionated suspensions of 2D phosphorus (Figure 3-4) were analyzed using an integrating sphere to capture both transmitted and scattered light.

The polycrystalline black phosphorus within the KBr pellet had a high optical density, which allowed us to quantify light absorption near the band gap threshold. We observed an onset of absorption at *ca.* 0.4 eV (Figure 3-7a, black), characteristic of bulk black phosphorus. The analysis of cleaved phosphorus flakes (20 to 40 nm thick) with low optical density revealed an additional absorption edge at *ca*. 1.95 eV (Figure 3-7a, gray). We attribute this absorption event to a higher energy transition. We will see that these two absorption thresholds—the low-energy band gap transition and the high-energy transition (see band diagram in Figure 3-8b)—are also present in suspensions of 2D phosphorus.

The fractionated suspensions of 2D phosphorus varied significantly in their appearance: in transmitted light, dilute suspensions of thick pieces appeared black or brown while those containing primarily thin pieces appeared red or yellow (Figure 3-7b, inset). These observations were consistent with the corresponding optical absorbance spectra of the suspensions (Figure 3-7b) in which we observed a spectral blue-shift as the flake thickness decreased. There are two notable features in these spectra: a sharply rising absorption within the visible region and a

slowly rising absorption that extends into the near-IR. In the following analysis, we will attribute these spectral features to the same high- and low-energy transitions observed in the bulk material.

We sought to quantify these absorption features by using a Tauc analysis. The high-energy transition achieved an excellent fit to a Tauc model when $n = 2$, indicating that this transition is direct and allowed (Figure 3-7c). We assigned the high-energy transition energies to values of 1.95 eV in bulk black phosphorus and 3.15 eV in a suspension containing primarily monolayers, the thinnest fraction analyzed. The fact that the Tauc models fit our data may suggest that the five experimental challenges outlined above—light scattering, high exciton binding energy, Urbach tail, anisotropic optical properties, and variation in band gap—have a negligible effect on our Tauc analyses of the high-energy transition.

When we applied the direct Tauc model to the low-energy transition, we measured a value of 0.40 eV for bulk black phosphorus (Figure3- 7d, bulk) which is slightly larger than previous estimates of its band gap. The method of sample preparation—grinding bulk black phosphorus with KBr to make a pellet—may have exfoliated some thin sheets, yielding a slightly larger band gap. We found that the band gap is direct and allowed, which is consistent with earlier findings. Because theory consistently predicts that the band gap is direct for all thicknesses of 2D phosphorus, we attempted to apply direct Tauc models (both allowed and forbidden) to the low-energy, band gap transition of 2D phosphorus. For all Tauc models that we explored, we never found a linear region of the Tauc plot, which prevented us from determining the band gap using this method (Figure 3-7d shows the direct, allowed Tauc plot). We attribute the non-linearity of the Tauc plot to several causes. First, the low-energy transition has a lower absorption coefficient than the high-energy transition. The weak absorbance is more likely to be obscured

by other optical processes, such as light absorption from Urbach tails or light scattering. Second, the polydispersity of our samples gives a broader distribution of absorption edges for the low-

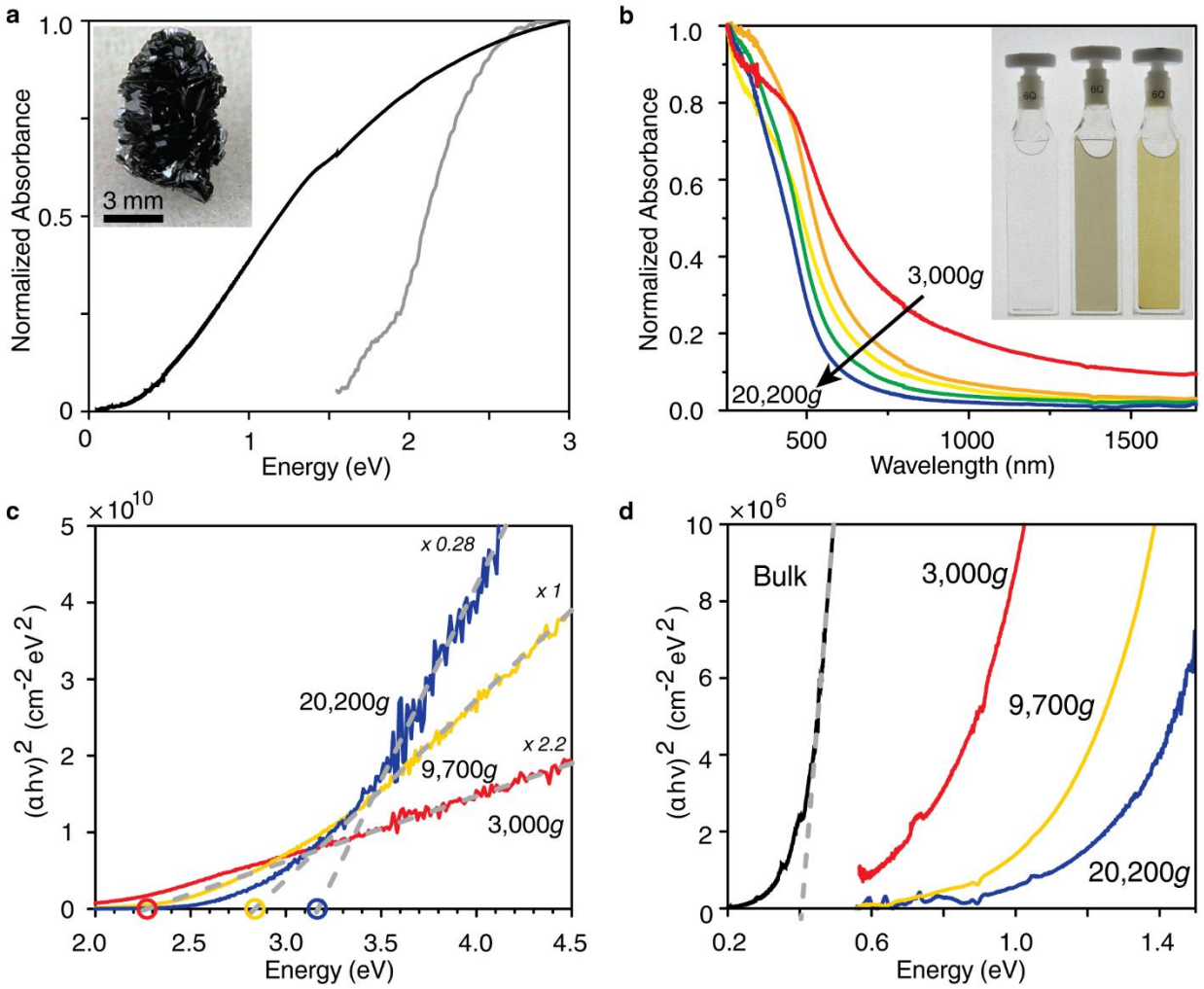

Figure 3-7. UV-vis-nIR spectroscopy of black phosphorus and few-layer flakes: **(A)** Optical absorbance of bulk phosphorus measured at two different optical densities (black = high; gray = low) to reveal two distinct optical transitions (*ca.* 0.4 eV and 1.95 eV). **(B)** Absorbance of 2D phosphorus suspensions that were prepared by fractionation at RCFs near 3.0, 5.9, 9.7, 14.5, and 20.2 thousand *g*'s (red to blue). **(C)** Representative direct Tauc plots used to determine the band-to-band transition. **(D)** Representative direct Tauc plots of the low-energy optical transition. The fit to Tauc models is poor, consistent with the wider range of optical absorption edges that are present in these suspensions.

energy absorption than the high-energy absorption. This is because the high-energy transition is less sensitive to flake thickness than the low energy transition, as will become apparent in the following analysis. Because of these experimental challenges in applying a Tauc analysis to the absorption edge of 2D phosphorus, we introduce a new analytical method that can supplant the Tauc method when analyzing families of bulk and quantum-confined semiconductors.

3.7 A method for determining absorption edges in quantum-confined semiconductors

In our suspensions of 2D phosphorus, sample polydispersity has prevented a straightforward application of Elliot's theory. Indeed, this is an extremely common problem and the liberal application of the Tauc method often causes large errors in the measurement of band gaps.[56] To circumvent these challenges, we now introduce an alternate method that can be applied to families of bulk and quantum-confined semiconductors such as black and 2D phosphorus. We validated our method using simulated absorption spectra of monodisperse and polydisperse suspensions of 2D phosphorus. Our tests demonstrate that the method is robust: it can determine absorption edges of semiconductors in polydisperse samples and has several advantages over the Tauc method, such as providing an estimate of uncertainty in the absorption edge energy (usually less than a few percent). Crucially, the measurement of an absorption edge (also called the optical gap) also allows us to determine the band gap because the optical and band gaps differ in energy by the exciton binding energy, which is <15 meV in our experiments and therefore negligible.

Our analytical method, which we call the "alpha method", utilizes the similarities that often exist between the electronic structures of quantum-confined semiconductors and the corresponding bulk semiconductor. As an example, numerous studies of black phosphorus and 2D phosphorus show that the band gaps of bulk and 2D phosphorus are always direct with both

allowed and forbidden contributions, that their lowest energy transition is always located at the Z-point (in a 3D Brillouin zone), and that the conduction and valence bands are always comprised primarily of p_z orbitals.[17,37,55] In the case of the black phosphorus family, these similarities result in joint densities of states near the absorption edge that are virtually unchanged among members of the family, except for an effective scissoring of the band gap energy. In general, the absorption coefficient increases with increasing quantum confinement,[79] but we hypothesized that the change in the absorption coefficient at the absorption edge (α_{AE}) with confinement would be small and could therefore be treated as being unchanged from the bulk to the monolayer. While this is an oversimplification, we will show that this introduces only a small error in the determination of optical/band gap energies.

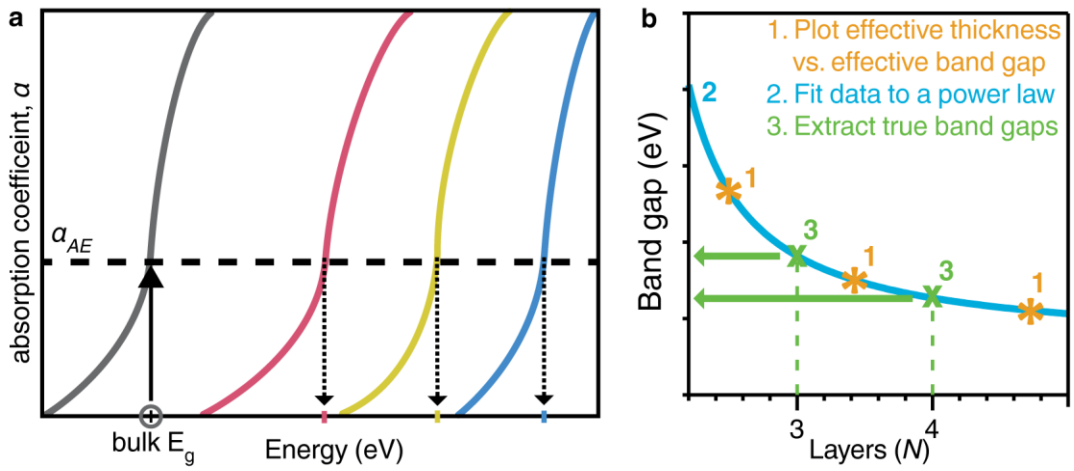

Figure 3-8. "Alpha method" for band gap determination: (A) The absorption coefficient at the absorption edge (α_{AE}) is measured for the bulk material. We use this α_{AE} to estimate the band gap energy for the quantum-confined 2D flakes. If the 2D flakes are not monodisperse in thickness, the band gap that we have determined is an effective band gap. **(B)** To convert an effective band gap into a real band gap, we (1) plot the effective band gap *vs*. effective thickness for a series of polydisperse samples. Next (2), we fit the data to a power law, see equation [3.1] in the text. Lastly (3), we use the power law fit to extract the band gap for 2D flakes with real thicknesses.

The step-wise analytical method that follows from this hypothesis is illustrated in Figure 3-8a. Using black phosphorus as an example, we exploit the fact that the band gap of the bulk

material has been measured many times and has a well-defined value (0.33 ± 0.02 eV). First, we measure the absorption spectrum of the bulk material to determine the value of α_{AE}. Second, we measure the absorption spectra of a series of samples of 2D phosphorus. Finally, we assign the band gap of each sample as the energy at which the absorption coefficient equals α_{AE} (see Figure 3-8a). Note that this process is equating the absorption edge (optical gap) and the fundamental absorption edge (band gap), which is an accurate approximation in our experiments but is not necessarily true in all cases.

To validate the alpha method, we used four calculated (G_0W_0) absorption spectra—the spectra that come from bulk, trilayer, bilayer, and monolayer phosphorus.[37] For each spectrum, we used the reported band gaps, acquired by measuring the energy difference between the conduction and valence bands. We then applied the alpha method to the same data to obtain a second estimate. Across this family of materials, we found that the maximum difference between the methods was 1.85%—an amount that is essentially negligible for most purposes. Although the central assumption—that α_{AE} is the same in all members of the family—is not true, the error due to this assumption is small. This is because α rises steeply near the band gap ($d\alpha/dE$ is large as the energy E approaches the band gap energy E_g). Consequently, even if large differences in α_{AE} exist among the members of a semiconductor family, these produce small differences in the estimated band gap energy.

With this set of results for monodisperse samples in hand, we then tested whether the alpha method could be applied to polydisperse samples. We constructed a series of 24 different artificial mixtures of 2-, 3-, 4-, and 5-layer pieces by taking linear combinations of the calculated absorption spectra of the individual flakes. For these mixtures, Tauc plots were often unusable: the plots either contained several linear regions or did not contain any linear region at all. On the

other hand, when we applied the alpha method to each suspension, we always obtained an estimate of an "effective band gap". We found that the effective band gap increased monotonically as the sample distributions shifted from containing a majority of thicker flakes (4- or 5-layers) to a majority of thinner flakes (2- or 3-layers) and that, as expected, the effective band gap always fell between the band gaps of the thinnest (2-layer) and thickest (5-layer) flakes. This example shows that the effective band gap does not necessarily correspond to the band gap of any real material but rather represents the contributions from various-sized flakes in a given mixture. Nevertheless, if this effective band gap is properly correlated with an "effective thickness" and these band gap-thickness correlations are performed on multiple samples, then it would be possible, at least in principle, to interpolate between these data points to obtain the band gap of 2D materials with real thicknesses (*e.g.*, a bilayer or a trilayer) as illustrated in Figure 3-8b.

The challenge with this approach is that it is not obvious whether the interpolated values are correct. We addressed this challenge by applying a robust mathematical approach to determine an effective thickness for each simulated mixture that, when paired with the effective band gap (alpha method), would lead to correct values of the band gap for real flake thicknesses. We compared our effective thicknesses and effective band gaps to those predicted by a power-law fit of the true thickness and true band gaps for the individual flakes in our simulated mixtures. A power-law fit was selected because, as suggested by numerous calculations, it appears to correctly describe the variation in band gap with flake thickness.[16,28,37,67,80] The power law model yields a band gap for the N_{th} layer as:

$$E_{g_N} = \frac{E_{g_1} - E_{g\infty}}{N^x} + E_{g\infty} \qquad (3.1)$$

where E_{g_1} is the band gap of phosphorene (a monolayer), E_{g_∞} is the band gap of bulk black phosphorus and *x* is a parameter describing the nature of quantum confinement in the system. Values of *x* are usually between 0 and 2, where the variation is due in large part to the extent of Coulomb interactions[79,81] and therefore depends on the material geometry (quantum dot *vs*. nanowire *vs*. 2D flake). In the present case, the power law fit is useful because it provides an excellent fit to the calculated G_0W_0 spectra and because it allows us to make direct comparisons of the real band gaps to the effective band gaps at non-real (*i.e.*, non-integer) thicknesses.

In these calculations, we considered the same series of mixtures as above. The skewness of these 24 distributions was systematically varied to capture the full range of likely skews that may be observed experimentally, which, as seen in Figure 4, typically have a log-normal shape. For each artificial mixture, we employed the alpha method to determine an effective band gap and we tested five different statistical approaches to extract effective thicknesses. The approaches that we tested were a number-averaged mean (analogous to $\overline{M_n}$ in polymer physics), a weight-averaged mean (analogous to $\overline{M_w}$ in polymer physics), and the mean, median and mode that were derived from a log-normal fit to each distribution. We note that the weight-averaged mean is not equivalent to a weight fraction, which is defined as the weight of material per total weight of solvent and material (see Supporting Information, Section 11, for a complete description of these statistical measures).

From these 24 mixtures comprising realistic skews, we found that the best two averages were the log-normal mean and the number-averaged mean. When paired with the effective thickness as calculated by the log-normal mean, the calculated band gap (power law) was 0.3 ± 1.5% above the effective band gap (alpha method). When paired with the effective thickness from the number-averaged mean, the calculated band gap was 0.2 ± 2.6% below the effective

band gap. The next two closest measures of thickness were the log-normal median (2.3 ± 1.6% above the effective band gap) and the weight-averaged mean (3.6 ± 3.5% below the effective band gap). In general, we found that the extent to which these statistical measures over- or underestimated the true bandgap varied systematically with the skewness of the distribution. For distributions with low skewness, the band gap was systematically overestimated by about 1.5%, while distributions with high skewness, such as those obtained in our experiments (Figure 4), the band gap was systematically underestimated by about 1%, although there were a small number of outliers with errors up to 6%. A table and graphs that summarize these calculations are provided in section 11 of the Supporting Information.

The central conclusion from these simulations is that the alpha method, when combined with an appropriate flake thickness, yields band gaps that are reliable. As noted above, the maximum difference between the reported band gap and the alpha band gap was 1.85%. In addition, the maximum error in using either the number-averaged mean or the log-normal mean was 6%. We emphasize that these are maximum errors and the typical errors will be less. However, these estimates of error only describe those errors due to data analysis and do not include systematic or non-systematic errors that are inherent to the experimental measurements.

3.8 Thickness-dependent absorption edges of black and 2D phosphorus

In this section, we compile the results of our experimental determination of the absorption edge of 2D phosphorus. As we described above, the absorption edge probed by our experiments (the optical gap) is indistinguishable from the band gap because the exciton binding energy is extremely small (8 to 15 meV) and exciton fission is rapid. When discussing the energy associated with a particular transition, we will use “absorption edge”, “optical gap” and “band gap” interchangeably.

From the absorption spectrum of bulk black phosphorus, we measured α_{AE} to be 0.24 μm^{-1}, which is equivalent to a light penetration depth of 4 μm. (We note that the absorption coefficient determined by us is similar to the one reported previously,[73] $\alpha_{AE} = 0.17\ \mu m^{-1}$.) We then used this absorption coefficient to determine the effective band gap of each 2D phosphorus suspension. The thickness distribution of each phosphorus suspension was analyzed by TEM and this distribution was converted into effective thicknesses using the four most accurate statistical averages (log-normal mean, number-averaged mean, log-normal median and weight-averaged mean). For each of these averages, a power law (Equation 3.1) was fit to the thickness-band gap data set. The same process was repeated for the high-energy transition, with the only difference being that the band-to-band transition energy was taken from a Tauc analysis rather than the alpha method (see justification, above).

Figure 3-9 summarizes our most important findings: the experimental quantification of the band-to-band transitions of 2D phosphorus. Figure 3-9a displays the band gaps (orange curves, "low energy") and high-energy transitions (blue curves, "high energy"). The low energy and high energy transitions show the most probable values (dark orange, dark blue) and a maximum likely range of values (light orange, light blue). The four curves that define the most probable and maximum likely boundaries come from the power-law fits to the four types of effective thicknesses, with the most probable boundaries defined by the log-normal and number-averaged means and with the maximum likely boundaries defined by the log-normal median and weight-averaged mean. The average exponent *x* of the power law (Equation 3.1) calculated from our data is 0.81. Earlier theoretical predictions suggest that the value may between 0.7 and 1.0, with an average value of 0.80 ± 0.11 reported across six studies.[16,28,37,66,82,83]

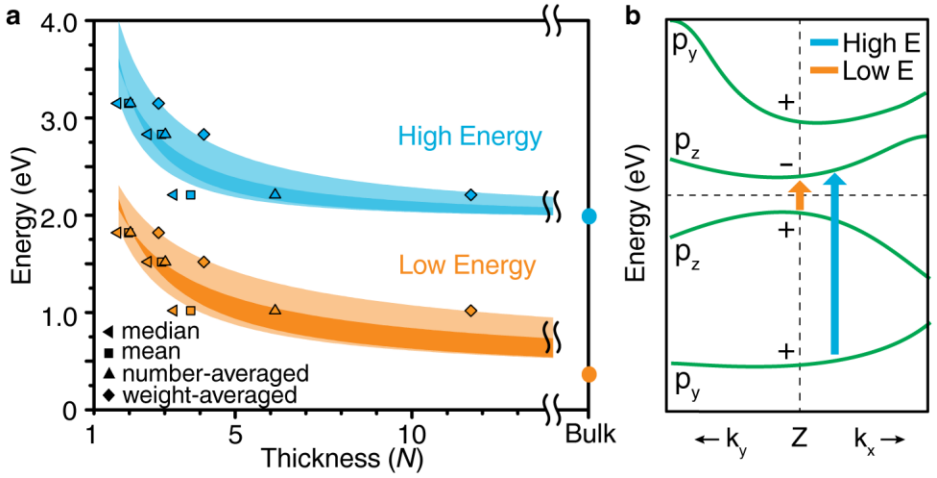

Figure 3-9. Experimentally determined band gap (low energy) and high-energy transitions of 2D and bulk black phosphorus: (A) The band gap (orange, "low energy") and high-energy band-to-band (blue, "high energy") transitions are plotted with respect to flake thickness. The dark blue and dark orange regions define the most probable energy values and the light orange and light blue define the maximum likely range. **(B)** Band structure of bulk black phosphorus at the Z point of the first Brillouin zone. The orange arrow represents the band gap transition (VB → CB) while the blue arrow represents the high energy transition (VB-1 → CB). The plot also shows the parity of bands near the Z point (+, -) and the nature of orbitals that primarily contribute to each band (p_y, p_z). The valence bands come from angle-resolved photoelectron spectroscopy measurements[18,85] and the conduction bands come from calculations.[18,84] The horizontal dashed line shows the Fermi level.

Our measurements provide direct experimental evidence that the band gap and the high-energy transitions undergo extreme changes as flakes approach monolayer thickness. The band gap can be tuned from 0.33 ± 0.02 eV in bulk to 1.88 ± 0.24 eV in bilayers. The higher energy transition can be tuned from 1.95 ± 0.06 eV in bulk to 3.23 ± 0.39 eV in bilayers. These ranges surpass all known 2D materials and are as large as the most tunable quantum dots. The most important band gaps and high-energy transitions are reported in Figure 3-9a and Tables 3-1 and 3-2. Our estimates of error (*e.g.*, ± 0.24 eV for the band gap of bilayers) are the same as the maximum ranges in Figure 3-9a (light blue and light orange regions). These estimates of error do not include the 1.85% maximum error between the alpha method and reported gaps or experimental error. We have not extrapolated our power law to a monolayer thickness because

of the errors associated with such an extrapolation: the smallest effective thickness of our samples was 1.71 layers and it has also been suggested that a phosphorene monolayer does not lie on the power-law curve.[37]

Table 3-2. Electronic band-to-band transitions in 2D phosphorus.

Layers	Band gap (eV)	High-energy (eV)
2	1.88 ± 0.24	3.23 ± 0.39
3	1.43 ± 0.28	2.68 ± 0.32
4	1.19 ± 0.28	2.44 ± 0.27
5	1.04 ± 0.27	2.31 ± 0.23
6	0.94 ± 0.26	2.23 ± 0.20
7	0.87 ± 0.26	2.18 ± 0.17
8	0.81 ± 0.25	2.14 ± 0.16
9	0.77 ± 0.24	2.11 ± 0.14
10	0.73 ± 0.23	2.09 ± 0.13
15	0.62 ± 0.20	2.03 ± 0.09
20	0.56 ± 0.18	2.01 ± 0.07
∞	0.33 ± 0.02	1.95 ± 0.06

In order to place these measurements in context, we compare our band gaps to prior optical gap measurements (see Table 3-1). We focus, in particular, on the optical gaps of Yang[61] and Zhang[63] because these studies surveyed the largest range of flake thicknesses and because these studies are the only two that are in agreement. When the optical gap and band gap are measured in the same dielectric environment, the band gap is expected to be larger than the optical gap by an amount equal to the exciton binding energy. This relationship only holds true for measurements that are performed in media with the same dielectric constant, since the

exciton binding energy, optical gap, and band gap all depend on the medium's dielectric constant. This sensitivity to the medium's dielectric constant disappears as flakes become thicker and in the limit of thick flakes, the optical gaps and band gaps converge because the exciton binding energy is 8 meV in bulk black phosphorus.[17] To see whether the electrical gap and optical gap do converge, we focus on four- and five-layer thicknesses, which are the thickest flakes that have been studied in the photoluminescence (optical gap) experiments. The four-layer optical gap was reported as 0.86 eV and the five-layer optical gap was 0.80 eV. We measured a four-layer band gap as 1.19 ± 0.28 eV and a five-layer band gap as 1.04 ± 0.27 eV. It is apparent that the difference between the band gap in our experiments and the optical gap in the photoluminescence experiments is decreasing (0.33 eV for four-layer, 0.24 eV for five-layer), as expected. Although the extent to which we can make comparisons is limited by the available data, it appears that there is reasonable agreement between our measurements and some previous photoluminescence measurements.

Next, we turn our attention to the high-energy band-to-band transition. Although this transition has been neglected in earlier studies, we suggest two reasons that understanding this transition will be important. First, the changes in the color of 2D phosphorus with decreasing thickness (Figure 3-7b, inset) are due, in large part, to changes in the high-energy band-to-band transition rather than the band gap. As a result, the ability to modulate the material's color requires an understanding of the high energy transition. Second, the high-energy transition has a substantially larger absorption coefficient (3.3 μm^{-1} at 3 eV) and a smaller light penetration depth (300 nm at 3 eV) than the band gap transition. This feature will be important in designing 2D phosphorus for applications that require high light absorption. From our Tauc analyses of the high-energy transition, we found that the bulk material has a transition energy of 1.95 eV,

increasing up to 3.23 ± 0.39 eV in bilayers (Figure 9b, blue). From these measurements, it is also apparent that the high-energy transition is less sensitive to flake thickness as compared to the low-energy band gap transition: from bulk to bilayers, the band gap changes by 1.55 eV while the high-energy transition changes by 1.28 eV. This difference in sensitivity may be why Tauc plots appear to work well for the high-energy transition while they do not work for the low-energy transition.

Finally, we describe four key observations that allow us to determine the nature of the high-energy transition. First, the Tauc plots show that there is a linear relationship between $(\alpha h\nu)^2$ and the photon energy (Figure 3-7c), which is characteristic of a direct, allowed transition. Second, the high-energy transition is sensitive to material thickness, varying from 1.95 eV in bulk to 3.23 eV in bilayers. These changes follow a power law and therefore appear to be driven by quantum confinement.[79,81] As such, it is plausible that the high-energy transition occurs at or near the Z-point of the Brillouin zone, since Z is perpendicular to the plane of flakes. In examining the band structure near the Z-point (Figure 3-9b), it is clear that there are two likely candidates for a direct optical transition at or near the Z-point: a transition between the valence band (VB) and the second lowest unoccupied band (CB+1) or between the second highest occupied band (VB-1) and the conduction band (CB). Third, the energy of the transition for the bulk material (1.95 eV) can be compared to previous measurements of the band structure of bulk black phosphorus.[15,84] From these comparisons, it is clear that only the VB-1 → CB transition provides the right energy. Fourth, the absorption coefficient of the high-energy optical transition is considerably larger (about ten times larger) than that of the low-energy optical transition. This observation is consistent with an assignment of the optical transition to VB-1 → CB: this transition is direct, allowed in the *c*-direction, and leads to a change in parity (+ → -).[17] These

selection rules favor strong optical absorption. Figure 3-9b summarizes this assignment and also identifies the low-energy transition.

3.9 Conclusions

In this work, we have described our method[42] for preparing and isolating large quantities of monolayers, bilayers, and few-layer flakes and we identified benzonitrile as the best solvent of those we surveyed. Although shear mixing provides insufficient force for exfoliating high-quality samples of black phosphorus, it is possible to combine shear mixing and sonication to exfoliate black phosphorus at the 10-gram scale. Using XPS, TEM, and multi-slice TEM simulations, we observed that monolayers, bilayers, and few-layer flakes of 2D phosphorus are crystalline and unoxidized. Our work also demonstrates a rapid and simple TEM-based method for measuring the thickness of 2D phosphorus.

Using a method that we introduced here for quantifying the optical absorbance spectra, we showed that it is possible to measure the optical gap of polydisperse 2D phosphorus samples and to extract an accurate estimate of the material's band gap. Our results may go some ways towards resolving the long-standing question of how the band gap of black phosphorus changes with thickness. We expect that the methodology presented here will be broadly applicable as it provides a robust approach for optical or band gap measurement in mixtures of complex semiconductors and can extract useful information even when the Tauc analysis fails.

Of central importance for future applications of 2D phosphorus, we have performed the first accurate measurements of the thickness-dependent band gap. Although there are a large number of theoretical predictions, these predictions have not yet been tested, until now, by careful experiments. We found that the band gap can be tuned from 0.33 ± 0.02 eV in bulk black phosphorus to 1.88 ± 0.24 eV in bilayer phosphorus. It is important to note that the band gap

will likely depend on the surrounding medium but, in any case, the range of optical transitions for black and 2D phosphorus is relatively large compared to that of other quantum-confined nanomaterials such as MoS_2 (1.2 to 1.9 eV),[9,85] CdSe quantum dots (2.0 to 3.0 eV)[86] or PbSe quantum dots (0.27 to 1.5 eV).[11–13,86] This suggests that the electronic coupling between layers is stronger than in most other van der Waals layered solids but a complete description of this unusual property is still needed. Looking toward future applications of this material, we suggest that the astounding range of band gaps that can be achieved by 2D phosphorus, with tunable absorption thresholds from the infrared to the visible, will provide a new material platform for the design and development of solar cells, photodetectors, photocatalysts, transistors, and batteries.

REFERENCES

1. Thompson, B. C.; Fréchet, J. M. J. Polymer-Fullerene Composite Solar Cells. *Angew. Chem. Int. Ed.*, **2008**, *47*, 58–77.

2. Talapin, D. V; Murray, C. B. PbSe Nanocrystal Solids for N- and P-Channel Thin Film Field-Effect Transistors. *Science* **2005**, *310*, 86–89.

3. Wu, J.; Agrawal, M.; Becerril, H. A.; Bao, Z.; Liu, Z.; Chen, Y.; Peumans, P. Organic Light-Emitting Diodes on Solution-Processed Graphene Transparent Electrodes. *ACS Nano* **2010**, *4*, 43–48.

4. Rossetti, R.; Nakahara, S.; Brus, L. E. Quantum Size Effects in the Redox Potentials, Resonance Raman Spectra, and Electronic Spectra of CdS Crystallites in Aqueous Solution. *J. Chem. Phys.* **1983**, *79*, 1086.

5. Brus, L. Electronic Wave Functions in Semiconductor Clusters: Experiment and Theory. *J. Phys. Chem.* **1986**, *90*, 2555–2560.

6. Rossetti, R.; Hull, R.; Gibson, J. M.; Brus, L. E. Excited Electronic States and Optical Spectra of ZnS and CdS Crystallites in the ~15 to 50 Å Size Range: Evolution from Molecular to Bulk Semiconducting Properties. *J. Chem. Phys.* **1985**, *82*, 552.

7. Dannhauser, T.; Johansson, K.; Whitten, D. Photophysics of Quantized Colloidal Semiconductors. Dramatic Luminescence Enhancement by Binding of Simple Amines. **1986**, *90*, 6074–6076.

8. Novoselov, K. S.; Jiang, D.; Schedin, F.; Booth, T. J.; Khotkevich, V. V; Morozov, S. V; Geim, A. K. Two-Dimensional Atomic Crystals. *Proc. Natl. Acad. Sci. U. S. A.* **2005**, *102*, 10451–10453.

9. Mak, K. F.; Lee, C.; Hone, J.; Shan, J.; Heinz, T. F. Atomically Thin MoS_2: A New Direct-Gap Semiconductor. *Phys. Rev. Lett.* **2010**, *105*, 136805.

10. Yun, W. S.; Han, S.; Hong, S. C.; Kim, I. G.; Lee, J. Thickness and Strain Effects on Electronic Structures of Transition Metal Dichalcogenides: 2H-MX_2 Semiconductors (M = Mo, W; X = S, Se, Te). *Phys. Rev. B*, **2012**, *85*, 033305.

11. Gorer, S.; Albu-Yaron, A.; Hodes, G. Quantum Size Effects in Chemically Deposited, Nanocrystalline Lead Selenide Films. *J. Phys. Chem.* **1995**, *99*, 16442–16448.

12. Kang, I.; Wise, F. W. Electronic Structure and Optical Properties of PbS and PbSe Quantum Dots. *J. Opt. Soc. Am. B*, 1997, *14*, 1632.

13. Pietryga, J. M.; Schaller, R. D.; Werder, D.; Stewart, M. H.; Klimov, V. I.; Hollingsworth, J. A. Pushing the Band Gap Envelope: Mid-Infrared Emitting Colloidal PbSe Quantum Dots. *J. Am. Chem. Soc.* **2004**, *126*, 11752–11753.

14. Bridgman, P. W. Two New Modifications of Phosphorus. *J. Am. Chem. Soc.* **1914**, *36*, 1344–1363.

15. Li, L.; Yu, Y.; Ye, G. J.; Ge, Q.; Ou, X.; Wu, H.; Feng, D.; Chen, X. H.; Zhang, Y. Black Phosphorus Field-Effect Transistors. *Nat. Nano.* **2014**, *9*, 372–377.

16. Liu, H.; Neal, A. T.; Zhu, Z.; Luo, Z.; Xu, X.; Tománek, D.; Ye, P. D. Phosphorene: An Unexplored 2D Semiconductor with a High Hole Mobility. *ACS Nano* **2014**, *8*, 4033–4041.

17. Morita, A. Semiconducting Black Phosphorus. *Appl. Phys. A* **1986**, *39*, 227–242.

18. Li, L.; Yu, Y.; Ye, G. J.; Ge, Q.; Ou, X.; Wu, H.; Feng, D.; Chen, X. H.; Zhang, Y. Black Phosphorus Field-Effect Transistors. *Nat. Nano.* **2014**, *9*, 372–377.

19. Koenig, S. P.; Doganov, R. A.; Schmidt, H.; Castro Neto, A. H.; Özyilmaz, B. Electric Field Effect in Ultrathin Black Phosphorus. *Appl. Phys. Lett.* **2014**, *104*, 103106.

20. Buscema, M.; Groenendijk, D. J.; Steele, G. A.; van der Zant, H. S. J. Photovoltaic Effect in Few-Layer Black Phosphorus PN Junctions Defined by Local Electrostatic Gating. *Nat. Comm.* **2014**, *5*, 4651.

21. Deng, Y.; Luo, Z.; Conrad, N. J.; Liu, H.; Gong, Y.; Najmaei, S.; Ajayan, P. M.; Lou, J.; Xu, X.; Ye, P. D. Black Phosphorus-Monolayer MoS_2 van Der Waals Heterojunction P-N Diode. *ACS Nano* **2014**, *8*, 8292-8298.

22. Engel, M.; Steiner, M.; Avouris, P. A Black Phosphorus Photo-Detector for Multispectral, High-Resolution Imaging. *Nano Lett.* **2014**, *14*, 6414–6417.

23. Low, T.; Engel, M.; Steiner, M.; Avouris, P. Origin of Photoresponse in Black Phosphorus Phototransistors. *Phys. Rev. B* **2014**, *90*, 081408.

24. Park, C.-M.; Sohn, H.-J. Black Phosphorus and Its Composite for Lithium Rechargeable Batteries. *Adv. Mater.* **2007**, *19*, 2465–2468.

25. Cunningham, G.; Lotya, M.; Cucinotta, C. S.; Sanvito, S.; Bergin, S. D.; Menzel, R.; Shaffer, M. S. P.; Coleman, J. N. Solvent Exfoliation of Transition Metal Dichalcogenides: Dispersibility of Exfoliated Nanosheets Varies Only Weakly Between Compounds. *ACS Nano* **2012**, *6*, 3468–3480.

26. Fei, R.; Yang, L. Strain-Engineering the Anisotropic Electrical Conductance of Few-Layer Black Phosphorus. *Nano Lett.* **2014**, *14*, 2884–2889.

27. Low, T.; Rodin, A. S.; Carvalho, A.; Jiang, Y.; Wang, H.; Xia, F.; Neto, A. H. C. Tunable Optical Properties of Multilayers Black Phosphorus. *Phys. Rev. B* **2014**, 90, 075434.

28. Castellanos-Gomez, A.; Vicarelli, L.; Prada, E.; Island, J. O.; Narasimha-Acharya, K. L.; Blanter, S. I.; Groenendijk, D. J.; Buscema, M.; Steele, G. A; Alvarez, J. V; *et al.* Isolation and Characterization of Few-Layer Black Phosphorus. *2D Mater.* **2014**, *1*, 025001.

29. Jiang, J.-W.; Park, H. S. Mechanical Properties of Single-Layer Black Phosphorus. *J. Phys. D. Appl. Phys.* **2014**, *47*, 385304.

30. Kou, L.; Frauenheim, T.; Chen, C. Phosphorene as a Superior Gas Sensor: Selective Adsorption and Distinct I - V Response. *J. Phys. Chem. Lett.* **2014**, *5*, 2675–2681.

31. Zhang, R.; Li, B.; Yang, J. First-Principles Study of the Interactions of Electron Donor and Acceptor Molecules with Phosphorene. *arXiv* **2014**, *1409.7190*.

32. Favron, A.; Gaufrès, E.; Fossard, F.; Phaneuf-L'Heureux, A.-L.; Tang, N. Y.-W.; Lévesque, P. L.; Loiseau, A.; Leonelli, R.; Francoeur, S.; Martel, R. Photooxidation and Quantum Confinement Effects in Exfoliated Black Phosphorus. *Nat. Mater.* **2015**, 826–832.

33. Ziletti, A.; Carvalho, A.; Campbell, D. K.; Coker, D. F.; Neto, A. H. C. Oxygen Defects in Phosphorene. *Phys. Rev. Lett.* **2014**, 046801.

34. Carvalho, A.; Rodin, A. S.; Neto, A. H. C. Phosphorene Nanoribbons. *EPL-Europhys. Lett.* **2014**, *108*, 47005.

35. Xie, J.; Si, M. S.; Yang, D. Z.; Zhang, Z. Y.; Xue, D. S. A Theoretical Study of Blue Phosphorene Nanoribbons Based on First-Principles Calculations. *J. Appl. Phys.* **2014**, *116*, 073704.

36. Guan, J.; Zhu, Z.; Tomanek, D. High Stability of Faceted Nanotubes and Fullerenes of Multi-Phase Layered Phosphorus: A Computational Study. *Phys. Rev. Lett.* **2014**, 113, 226801.

37. Tran, V.; Soklaski, R.; Liang, Y.; Yang, L. Layer-Controlled Band Gap and Anisotropic Excitons in Few-Layer Black Phosphorus. *Phys. Rev. B* **2014**, *89*, 235319.

38. Xia, F.; Wang, H.; Jia, Y. Rediscovering Black Phosphorus as an Anisotropic Layered Material for Optoelectronics and Electronics. *Nat. Commun.* **2014**, *5*, 4458.

39. Buscema, M.; Groenendijk, D. J.; Blanter, S. I.; Steele, G. A.; van der Zant, H. S. J.; Castellanos-Gomez, A. Fast and Broadband Photoresponse of Few-Layer Black Phosphorus Field-Effect Transistors. *Nano Lett.* **2014**, *14*, 3347–3352.

40. Hernandez, Y.; Nicolosi, V.; Lotya, M.; Blighe, F. M.; Sun, Z.; De, S.; McGovern, I. T.; Holland, B.; Byrne, M.; Gun'Ko, Y. K.; *et al.* High-Yield Production of Graphene by Liquid-Phase Exfoliation of Graphite. *Nat. Nano.* **2008**, *3*, 563–568.

41. Coleman, J. N.; Lotya, M.; O'Neill, A.; Bergin, S. D.; King, P. J.; Khan, U.; Young, K.; Gaucher, A.; De, S.; Smith, R. J.; *et al.* Two-Dimensional Nanosheets Produced by Liquid Exfoliation of Layered Materials. *Science* **2011**, *331*, 568–571.

42. Warren, S. C.; Woomer, A. H.; Wells, R. A.; Farnsworth, T. W. Two Dimensional Materials Produced by the Liquid Exfoliation of Black Phosphorus. 62/031,184, 2014.

43. Brent, J. R.; Savjani, N.; Lewis, E. A.; Haigh, S. J.; Lewis, D. J.; O'Brien, P. Production of Few-Layer Phosphorene by Liquid Exfoliation of Black Phosphorus. *Chem. Commun.* **2014**, *50*, 13338–13341.

44. Yasaei, P.; Kumar, B.; Foroozan, T.; Wang, C.; Asadi, M.; Tuschel, D.; Indacochea, J. E.; Klie, R. F.; Salehi-Khojin, A. High-Quality Black Phosphorus Atomic Layers by Liquid-Phase Exfoliation. *Adv. Mater.* **2015**, *27*, 1887–1892.

45. Kang, J.; Wood, J. D.; Wells, S. A.; Lee, J.-H.; Liu, X.; Chen, K.-S.; Hersam, M. C. Solvent Exfoliation of Electronic-Grade, Two-Dimensional Black Phosphorus. *ACS Nano* **2015**, *9*, 3596–3604.

46. Köpf, M.; Eckstein, N.; Pfister, D.; Grotz, C.; Krüger, I.; Greiwe, M.; Hansen, T.; Kohlmann, H.; Nilges, T. Access and *In Situ* Growth of Phosphorene-Precursor Black Phosphorus. *J. Cryst. Growth* **2014**, *405*, 6–10.

47. Stadelmann, P. JEMS - EMS Java Version http://cimewww.epfl.ch/people/stadelmann/jemsWebSite/jems.html.

48. Ci, L.; Song, L.; Jin, C.; Jariwala, D.; Wu, D.; Li, Y.; Srivastava, A.; Wang, Z. F.; Storr, K.; Balicas, L.; *et al.* Atomic Layers of Hybridized Boron Nitride and Graphene Domains. *Nat. Mater.* **2010**, *9*, 430–435.

49. Gass, M. H.; Bangert, U.; Bleloch, A. L.; Wang, P.; Nair, R. R.; Geim, A. K. Free-Standing Graphene at Atomic Resolution. *Nat. Nano.* **2008**, *3*, 676–681.

50. Favron, A.; Gaufrès, E.; Fossard, F.; Lévesque, P. L.; Heureux, P.; Tang, N. Y.; Loiseau, A.; Leonelli, R. Exfoliating Black Phosphorus down to the Monolayer: Photo-Induced Oxidation and Electronic Confinement Effects. *arXiv* **2014**, *1408.0345*.

51. Goodman, N. B.; Ley, L.; Bullett, D. W. Valence-Band Structures of Phosphorus Allotropes. *Phys. Rev. B* **1983**, *27*, 7440–7450.

52. Moulder, J. F.; Stickle, W. F.; Sobol, P. E.; Bomben, K. D. *Handbook of X-Ray Photoelectron Spectroscopy*; 1979; Vol. 3.

53. Wood, J. D.; Wells, S. A.; Jariwala, D.; Chen, K.-S.; Cho, E.; Sangwan, V. K.; Liu, X.; Lauhon, L. J.; Marks, T. J.; Hersam, M. C. Effective Passivation of Exfoliated Black Phosphorus Transistors against Ambient Degradation. *Nano Lett.* **2014**, *14*, 6964–6970.

54. Paton, K. R.; Varrla, E.; Backes, C.; Smith, R. J.; Khan, U.; O'Neill, A.; Boland, C.; Lotya, M.; Istrate, O. M.; King, P.; *et al.* Scalable Production of Large Quantities of Defect-Free Few-Layer Graphene by Shear Exfoliation in Liquids. *Nat. Mater.* **2014**, *13*, 624–630.

55. Paton, K. Personal Communication.

56. Takao, Y.; Asahina, H.; Morita, A. Electronic Structure of Black Phosphorus in Tight Binding Approach. *J. Phys. Soc. Jpn.* **1981**, *50*, 3362–3369.

57. Klingshirn, C. *Semiconductor Optics*; 2007.

58. Degoli, E.; Cantele, G.; Luppi, E.; Magri, R.; Ninno, D.; Bisi, O.; Ossicini, S. Ab Initio Structural and Electronic Properties of Hydrogenated Silicon Nanoclusters in the Ground and Excited State. *Phys. Rev. B* **2004**, *69*, 155411.

59. Choi, J. H.; Strano, M. S. Solvatochromism in Single-Walled Carbon Nanotubes. *Appl. Phys. Lett.* **2007**, *90*.

60. Jackson, W. B.; Kelso, S. M.; Tsai, C. C.; Allen, J. W.; Oh, S.-J. Energy Dependence of the Optical Matrix Element in Hydrogenated Amorphous and Crystalline Silicon. *Phys. Rev. B* **1985**, *31*, 5187–5198.

61. Mott, N. F. *Electronic Processes in Non-Crystalline Materials*; Davis, E. A., Ed.; 2nd Ed.; Clarendon Press: Oxford, 1979.

62. Yang, J.; Xu, R.; Pei, J.; Myint, Y. W.; Wang, F.; Wang, Z.; Yu, Z.; Lu, Y. Unambiguous Identification of Monolayer Phosphorene by Phase-Shifting Interferometry. *arXiv* **2014**, *1412.6701*.

63. Wang, X.; Jones, A. M.; Seyler, K. L.; Tran, V.; Jia, Y.; Wang, H.; Yang, L.; Xu, X.; Xia, F. Highly Anisotropic and Robust Excitons in Monolayer Black Phosphorus. *Nat. Nano.* **2014**, 10, 517-521.

64. Zhang, S.; Yang, J.; Xu, R.; Wang, F. Extraordinary Photoluminescence and Strong Temperature/Angle-Dependent Raman Responses in Few-Layer Phosphorene. *ACS Nano* **2014**, *8*, 9590–9596.

65. Das, S.; Zhang, W.; Demarteau, M.; Hoffmann, A.; Dubey, M.; Roelofs, A. Tunable Transport Gap in Phosphorene. *Nano Lett.* **2014**, *14*, 5733–5739.

66. Liang, L.; Wang, J.; Lin, W.; Sumpter, B. G.; Meunier, V.; Pan, M. Electronic Bandgap and Edge Reconstruction in Phosphorene Materials. *Nano Lett.* **2014**, *14*, 6400–6406.

67. Rudenko, A. N.; Katsnelson, M. I. Quasiparticle Band Structure and Tight-Binding Model for Single- and Bilayer Black Phosphorus. *Phys. Rev. B - Condens. Matter Mater. Phys.* **2014**, *89*, 1–5.

68. Qiao, J.; Kong, X.; Hu, Z.-X.; Yang, F.; Ji, W. High-Mobility Transport Anisotropy and Linear Dichroism in Few-Layer Black Phosphorus. *Nat. Commun.* **2014**, *5*, 4475.

69. Elliott, R. Intensity of Optical Absorption by Excitons. *Phys. Rev.* **1957**, *108*, 1384–1389.

70. Wannier, G. The Structure of Electronic Excitation Levels in Insulating Crystals. *Phys. Rev.* **1937**, *52*, 191–197.

71. Tauc, J. Optical Properties and Electronic Structure of Amorphous Ge and Si. *Mater. Res. Bull.* **1968**, *3*, 37–46.

72. Baba, M.; Nakamura, Y.; Shibata, K.; Morita, A. Photoconduction of Black Phosphorus in the Infrared Region. *Jpn. J. Appl. Phys.* **1991**, *30*, L1178.

73. Keyes, R. The Electrical Properties of Black Phosphorus. *Phys. Rev.* **1953**, *92*, 580

74. Warschauer, D. Electrical and Optical Properties of Crystalline Black Phosphorus. *J. Appl. Phys.* **1963**, *34*, 1853–1860.

75. Maruyama, Y.; Suzuki, S.; Kobayashi, K.; Tanuma, S. Synthesis and Some Properties of Black Phosphorus Single Crystals. *Physica B+C*, 1981, *105*, 99–102.

76. Irotani, I. S. H.; Physics, S. Growth of Large Single Crystals of Black Phosphorus at High Pressures and Temperatures, and Its Electrical Properties. *Mol. Cryst. Liq. Cryst.* **1982**, *86*, 203–211.

77. Akahama, Y.; Endo, S.; Narita, S. I. Electrical Properties of Black Phosphorus Single Crystals. *J. Phys. Soc. Japan* **1983**, *52*, 2148–2155.

78. Hecht, E.; Ganesan, A. R. *Optics*; 4th Ed.; Dorling Kindersley, 2008.

79. Urbach, F. The Long-Wavelength Edge of Photographic Sensitivity and of the Electronic Absorption of Solids. *Phys. Rev.* **1953**, *92*, 1324.

80. Brus, L. E. Electron–Electron and Electron-Hole Interactions in Small Semiconductor Crystallites: The Size Dependence of the Lowest Excited Electronic State. *J. Chem. Phys.* **1984**, *80*, 4403.

81. Rudenko, A. N.; Katsnelson, M. I. Quasiparticle Band Structure and Tight-Binding Model for Single- and Bilayer Black Phosphorus. *Phys. Rev. B* **2014**, *89*, 201408.

82. Perebeinos, V.; Tersoff, J.; Avouris, P. Scaling of Excitons in Carbon Nanotubes. *Phys. Rev. Lett.* **2004**, *92*, 257402–1.

83. Qiao, J.; Kong, X.; Hu, Z.-X.; Yang, F.; Ji, W. High-Mobility Transport Anisotropy and Linear Dichroism in Few-Layer Black Phosphorus. *Nat Commun* **2014**, *5*.

84. Wang, V.; Kawazoe, Y.; Geng, W. T. Native Point Defects in Few-Layer Phosphorene. *Phys. Rev. B* **2015**, *91*, 45433.

85. Yuan, H.; Liu, X.; Afshinmanesh, F.; Li, W.; Xu, G.; Sun, J.; Lian, B.; Ye, G.; Hikita, Y.; Shen, Z.; *et al.* Polarization-sensitive broadband photodetector using a black phosphorus vertical p–n junction. *Nat. Nano.* **2015**, *AOP*.

86. Splendiani, A.; Sun, L.; Zhang, Y.; Li, T.; Kim, J.; Chim, C.-Y.; Galli, G.; Wang, F. Emerging Photoluminescence in Monolayer MoS_2. *Nano Lett.* **2010**, *10*, 1271–1275.

87. Murray, C. B.; Norris, D.; Bawendi, M. G. Synthesis and Characterization of Nearly Monodisperse CdE (E= S, Se, Te) Semiconductor Nanocrystallites. *J. Am. Chem. Soc.* **1993**, *115*, 8706–8715.

CHAPTER FOUR – ENGINEERED 3D MATERIALS WITH QUANTUM-CONFINED 2D PROPERTIES

*Tyler W. Farnsworth[§#], Adam H. Woomer[§#], Jon R. Thompson[§], and Scott C. Warren[§]**

[§]Department of Applied Physical Sciences, University of North Carolina at Chapel Hill, Chapel Hill, NC 27599, USA.

[#]These authors contributed equally.

4.1 Introduction

Quantum confinement has resulted in some of the most exciting properties within chemistry, materials science, and physics. The size-dependent electronic structure of quantum confined materials have made them candidates for a wide variety of applications, from electronic displays[1-2] to photovoltaics[3-4] to medical imaging[5-6] to sensors[7-8]. Many applications, especially those in optics and electronics, require that quantum-confined building blocks retain their properties, even when in an aggregated, electronically conductive state. This requirement has led to numerous efforts in, for example, quantum dot solids, to identify methods of reducing the distance between dots while maintaining their quantum confined properties[9-13]. With the relatively recent emergence of 2D quantum-confined semiconductors, a similar challenge has now emerged: is it possible to control the separation between adjacent 2D flakes to produce highly conductive 3D solids that retain the quantum-confined optoelectronic properties of their 2D building blocks?

The emergence of quantum confinement in 2D semiconductors has been heralded as a significant advance towards enabling fascinating new materials. One of the outstanding examples of such quantum confined semiconductors is 2D MoS_2, which transitions to a direct band gap material with strong photoluminescence only at monolayer thickness[14-15]. Another exciting advance has been the development of quantum confined 2D phosphorus, which has a band gap that can be tuned from 0.3 eV (bulk) to 2.1 eV (monolayer)[6]. Numerous studies have examined the optoelectronic properties of 2D materials when they are restacked into solids. Such studies consistently show that the quantum confined properties are lost when two 2D solids are stacked on top of each other, regardless of the orientation between the two flakes[16].

Here we introduce a strategy to maintain quantum confinement in highly conductive 3D solids comprised of 2D materials. Our strategy relies on the entrapment of a monolayer of small molecules between adjacent layers, which lead to a small (ca. 4 Å) increase in interlayer spacing between adjacent flakes. This distance is large enough to maintain full quantum confinement—as judged by, for example, the photoluminescence of our 3D films of MoS_2—but is small enough to achieve among the highest electrical conductivities yet reported for 3D assemblies of 2D materials. Compared to quantum dots, which are challenged by trap state passivation, our 3D films have low trap state densities due to the intrinsic lack of surface states on all but the edges of 2D flakes. Furthermore, our results indicate that the conductivity of solids are at least the same order of magnitude, if not greater, than those of quantum dots. By using 2D materials as building blocks, we show that we can engineer 3D architectures that remain quantum-confined even in "bulk" form, allowing the integration of 2D materials into a wider range of technologies than were previously accessible and the fabrication of materials with a wide range of desirable colors and properties.

4.2 Qualitative optical evidence of quantum confinement in 2DM films

2D flakes of various TMDs and black phosphorus were prepared by liquid exfoliation by sonication in N-methyl 2-pyrrolidone (NMP). These were centrifuged to isolate 2D materials with well-defined thickness distributions. Samples containing monolayers of MoS_2 were prepared by n-butyl lithium-assisted chemical exfoliation, and transformed back into the 2H phase via refluxing in 1,3-dimethyl-3,4,5,6-tetrahydro-2(1H)-pyrimidinone (DMPU) under an inert atmosphere. Samples of 2D flakes were transferred into n-butanol for deposition in a Langmuir-Blodgett (LB) trough. Films of varying thicknesses were deposited onto glass, silicon, or polymer substrates through repeated LB film formation and deposition. Thicker films were prepared by vacuum filtration of suspensions of 2D flakes in isopropanol onto a 0.1 μm PVDF membrane.

The liquid suspensions of 2D flakes in solvents exhibited variable colors depending on their thickness owing to varying degrees of quantum confinement. Most samples transitioned from a grey/black color in thick flakes towards yellow or red in monolayers. When these flakes were deposited as thick films, either via LB deposition or vacuum filtration, we observed that the color of the films matched that of the starting 2D suspension (Figure 1A). When we measured the electrical conductivity of one such film of thin 2D phosphorus, we were surprised to observe that the the electrical conductivity, ca. 10^{-4} S/cm, exceeded that of many high quality films of 2D materials[17]. This suggested that, in spite of the quantum confinement, the flakes within these materials were in good electrical contact.

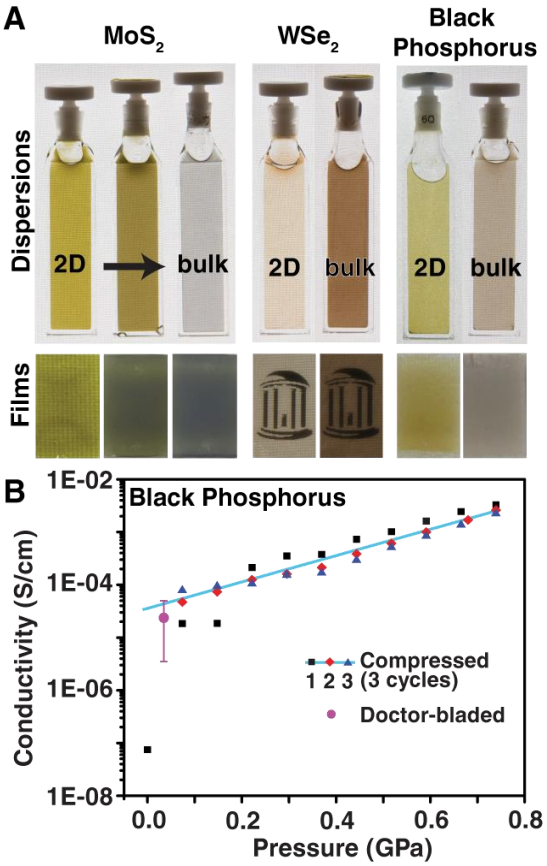

Figure 4-1. Suspensions and films of 2DM exhibiting quantum confined optical properties and electronic coupling: (A) 2D materials of MoS_2, WSe_2, and black phosphorus dispersed in solvent. Each film was prepared from the dispersion directly above. **(B)** Electrical conductivity of films of 2D black phosphorus at atmospheric pressure and under uniaxial pressure. After uniaxial pressure is released, the films retain quantum confinement and have an electrical conductivity of 10^{-5} to 10^{-4} S/cm.

4.3 Structural investigations of 2DM films

To understand the origin of this surprising combination of quantum confinement and electrical conductivity, we examined the structure of the vacuum-filtered and Langmuir-Blodgett films. Scanning electron microscopy of the vacuum filtered films (Figure 4-2A) revealed densely packed layers of 2D materials with a preferential co-facial alignment of adjacent 2D flakes. The Langmuir-Blodgett films were thinner, slightly rough, but individual flakes were difficult to distinguish (Figure 4-2B). The lack of well defined features suggested a relatively

dense packing of the 2D flakes. The co-facial alignment of adjacent flakes, as seen in (Figure 4-2A) for MoS_2, was observed in all vacuum filtered films, and could partially explain the high electrical conductivity observed in these films.

To provide deeper insight into the structure of these films, we performed several x-ray diffraction techniques. To confirm whether most flakes shared a similar orientation, we mapped the orientation of the (002) plane in a film made from few-layer MoS_2 using the pole figure technique (Figure 4-2C). The (002) plane is parallel to the plane of each 2D flake. A randomly oriented film would show equal intensities at all angles; instead, we observed strong intensities within 15 degrees of the film's normal. This indicated that most flakes were oriented with their normal nearly parallel to the film's normal, similar to the SEM image in Figure 2A. Next, to measure the spacing between flakes, we prepared a LB multilayer film made of monolayer MoS_2. Near room temperature, we observed strong diffraction at 8.9° 2-theta, corresponding to an interlayer distance of 7.0 Å (Figure 4-2 D,E). Upon heating above 240 °C, the peak at 8.9° disappeared and a new peak at 14.1° appeared, corresponding to an interlayer distance of 3.3 Å (the bulk interlayer distance is 3.2 Å). Upon returning to room temperature, the peak at 14.1° remained. This behavior suggested the presence of a molecule trapped between adjacent layers that evaporated upon heating. To assess if a molecule was present, we performed secondary ion mass spectroscopy (SIMS) on the same film. Indeed, we observed a large signal from the cyanide ion, which is a decomposition product from the DMPU solvent used to prepare the MoS_2 film. The boiling point of DMPU, 240 °C, agreed with the temperature at which the interlayer spacing decreased. These structural investigations indicate, therefore, that the 2D flakes are largely stacked parallel to each other (i.e., in a co-facial orientation) with a small, planar molecule holding apart adjacent layers.

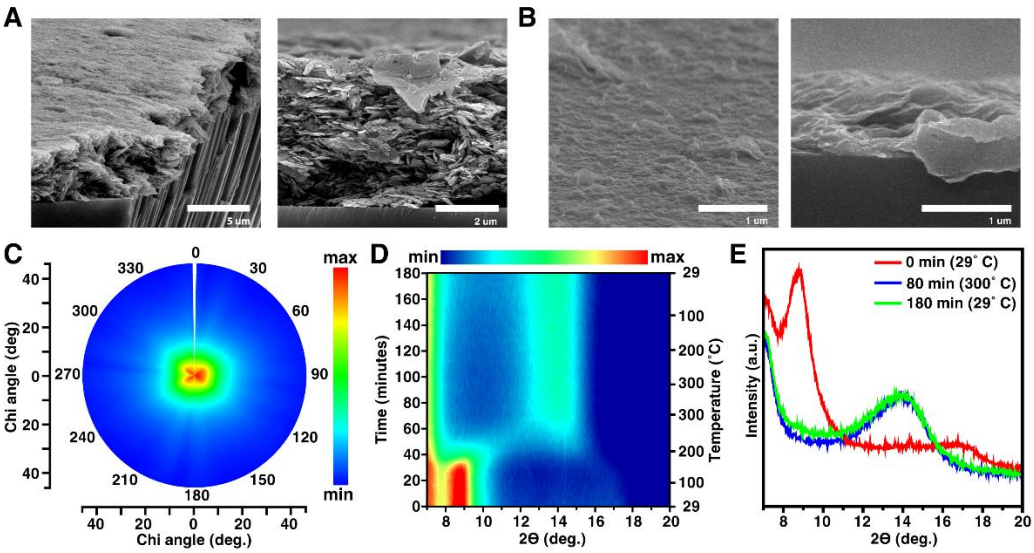

Figure 4-2. Structural analysis of MoS2 films: (A) SEM images of a vacuum-filtered film of few-layer MoS_2. **(B)** Top and side-view SEM images of a LB film of monolayer MoS_2. **(C)** Pole figure analysis of the (002) plane of a film of few-layer MoS_2. **(D, E)** 2-theta analysis of monolayer MoS_2 as a function of temperature; scale bar shows intensity of diffracted x-rays.

4.4 Van der Pauw Conductivity Measurements and Activation Energy of 2DM Films

To further understand the electronic coupling between individual flakes that have been reassembled into a film, we measured their electrical properties using uniaxially pressure- and temperature-dependent van der Pauw resistivity measurements (Figure 4-3). We use MoS_2 films as a model system because we can control the average number of layers per flake by choice of preparation technique: intercalation of n-butyllithium (nBuLi) yields primarily monolayer MoS_2 flakes while normal liquid exfoliated suspensions can be centrifuged to get polydisperse fractions of thin (3–10 layers) and thick (10 layers to bulk-like) flakes.

We first measured the conductivity of the films of monolayer MoS_2 (Figure 3A). We found that conductivity of films prior to pressurization (Figure 4-3A., black) is 3.2×10^{-8} S/cm at 30° C. When the pressure was increased to 0.1 GPa (Figure 4-3A., red), there was a dramatic increase in the conductivity to 6.1×10^{-6} S/cm at 30° C. It has been shown that for polycrystalline 2H-MoS_2, there is a 0.448 log (σ)/GPa dependence up to 10.0 GPa with

hydrostatic pressure[18]. For 0.1 GPa applied pressure, this corresponds to a 10% increase in conductivity. Given the 1000-fold increase in conductivity with applied pressure, we therefore conclude that the increase in conductivity with compression is due to an improvement in the percolative network for electrical transport. Increasing the pressure further to 0.2 GPa (Figure 3A., blue) only slightly improved the conductivity of the film, to 9.8×10^{-6} S/cm at 30° C.

For all pressures, there is a $\log \sigma \sim 1/T$ dependence. This dependence has also been observed in analogous systems, such as nanoparticle arrays, in which charge transport proceeds *via* hopping events across the array[19]. We measured an activation energy (E_a) for charge transport of 1.2 eV, which is larger than the reported in-plane E_a of 0.417 eV for 2H-MoS_2 at room temperature[20]. We therefore expect the measured activation energy to be the energy required for an electron to hop from one 2D flake to the next, thereby making one flake positively charged and the other negatively charged. This is called a charging energy, and is the work required to charge a capacitor to the elementary charge of an electron (Eqn. 4.1):

$$E_a = \int^{e} \frac{q}{C} dq = \frac{e^2}{2C} \qquad (4.1)$$

where q is charge and C is the capacitance. For spherical nanoparticle systems, it has been shown that E_a is proportional to s/r , where s and r are nanoparticle separation and radius, respectively[8].

We expect a similar dependence of E_a on flake thickness and separation. To investigate this dependence, we measured the electrical properties of vacuum filtered films with thick (10 layers to bulk-like) and thin (3 to 10 layers) MoS_2 flakes (Figure 4-3B,C). Consistent with our findings above, there was at least an order of magnitude increase in conductivity upon compression of the vacuum filtered films. Additionally, we find that $E_a \sim 1/t$, where t is the thickness of MoS_2 flakes and that pressurizing the film has a minimal effect on E_a. These

experiments demonstrate that compression does increase the proportion of flake area that is situated at the point of closest contact (an interlayer distance of 7.0 Å), where the rate of electron transfer is the highest.

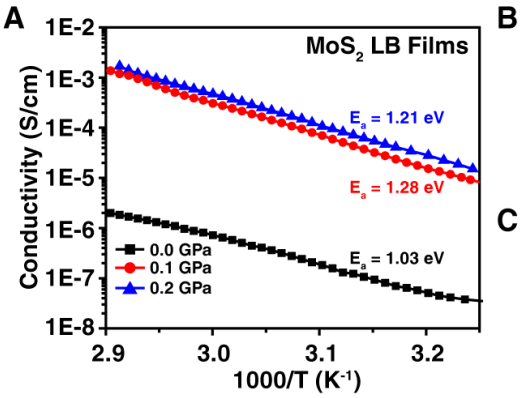

B

MoS_2 VF, 2k-4k RPM, 'thick' flakes

P (GPa)	σ, 23° C (S/cm)	σ, 66° C (S/cm)	E_a (eV)
0.00	3.44×10^{-5}	1.62×10^{-4}	0.321 ± 0.030
0.99	1.16×10^{-3}	5.24×10^{-3}	0.312 ± 0.006

C

MoS_2 VF, 12k-20k RPM, 'thin' flakes

P (GPa)	σ, 23° C (S/cm)	σ, 83° C (S/cm)	E_a (eV)
0.00	7.83×10^{-6}	1.16×10^{-4}	0.560 ± 0.016
0.49	3.11×10^{-5}	3.64×10^{-4}	0.545 ± 0.032

Figure 4-3. Electrical properties of MoS2 films with varying flake thickness. (A) Conductivity of MoS_2 films prepared from nBuLi exfoliation and Langmuir-Blodgett trough deposition. Tables of conductivity and activation energy values for vacuum filtered (VF) films of 'thick' (~10–40 layers) MoS_2 flakes **(B)** and thin (~3–10 layers) MoS_2 flakes **(C)**.

4.5 Raman and Photoluminescence evidence of Quantum confinement

With these conductivity measurements in hand, we next explored the quantum confinement of Langmuir-Blodgett films of various 2D materials via UV-vis-nIR, fluorescence, and Raman spectroscopies. We found that the dispersions of both bulk-like and few-layer (2D) MoS_2 flakes exhibited similar spectral shapes to the as-deposited films, and that the 2D films retained the same absorption edge as the 2D dispersions rather than reverting to the bulk-like film absorption edge. This suggests the retention of the quantum confined properties of the 2D building blocks (Figure 4-4A). The exciton absorption peaks of MoS_2 provide useful indicators of the degree of quantum confinement in these films[21-23], and the blue-shifted exciton A peak of the 2D MoS_2 film as compared to the bulk-like flakes (Figure 4-4A, inset) confirms the retention of quantum confinement.

We further probed the dependence of quantum confinement on flake-to-flake interlayer distance by performing photoluminescence measurements on films of nBuLi-exfoliated monolayer MoS_2 under an applied pressure. The monolayer photoluminescence (PL) peak of MoS_2 is known to quench and slightly red-shift when two flakes are brought into direct contact[24-26], indicative of the increase in interlayer electronic coupling as the flake thickness increases. By measuring the PL peak of monolayer MoS_2 under pressure, we can obtain a quantitative measure of the quantum confinement of our 2D material films and compare it directly to the conductivity studies under unilateral pressure.

An MoS_2 film was created via Langmuir-Blodgett assembly on a silicone substrate with five sequential depositions and the pressure was applied using a diamond anvil cell. The pressure was measured in-situ by monitoring the Ruby R_1 fluorescence peak and comparing to known calibration curves[27]. At 0 GPa pressure (Figure 4-4B), we observe a PL peak at ~664 nm, consistent with previous reports of monolayer and bilayer photoluminescence[27-30]. With applied pressure, the PL peak is quenched and blue-shifted with respect to the peak at 0 GPa but returns to its original position upon pressure release. This pressure-induced blue-shift and quenching has been previously observed for monolayer and bilayer flakes of MoS_2[31], suggesting that our assemblies of monolayer flakes are acting independently despite the applied pressure and are, in fact, not coupled. This agrees well with the pressure–conductivity and activation energy measurements that suggest that the increase in conductivity is due to the improved percolation network with compression rather than a decrease in flake-to-flake distance.

The A_{1g} and E^1_{2g} Raman modes of MoS_2 provide further evidence that the flakes remain confined under compression (Figure 4-4C). The peak frequency difference (cm^{-1}) of the A_{1g} and E^1_{2g} phonon modes is known to widen with increased flake thickness as a result of interlayer

coupling[32-34], with frequency differences of 19-20 cm^{-1} for the monolayer and ~25 cm^{-1} in bulk. The peak frequency differences for our sample (Figure 4-4D) at 0 GPa agree well with the reported values for monolayer and bilayer flakes of MoS_2. Under applied pressure, the peak frequency difference for our MoS_2 film increases slightly, but returns to the 0 GPa value after pressure release. The peak frequency differences at 0 and 2.70 GPa are both within the range of observed peak frequency differences for monolayer and bilayer flakes, and suggests that the flakes are not strongly coupled.

The slight widening of the peak frequency differences of the A_{1g} and E^1_{2g} modes with pressure could also be attributed to a pressure-induced effect on an individual crystal[31, 34-36] rather than interlayer flake-to-flake coupling. We can test this theory by examining the direction of peak shift for the phonon modes. For individual crystals of MoS_2, the A_{1g} mode stiffens (blue-shifts) and the E^1_{2g} softens (red-shifts) during the transition from monolayer to bulk. Under pressure, however, both of the Raman modes are known to stiffen and the peak frequency difference would widen. The data in Figure 4-4C clearly shows a stiffening of both the A_{1g} and E^1_{2g} modes for our MoS_2 films, allowing us to attribute the observed peak frequency widening to a pressure-induced effect of an individual flake. The collective results from the absorbance, photoluminescence, and Raman data unequivocally confirm that the MoS_2 flakes remain quantum confined when assembled as a thick film, despite being electronically coupled.

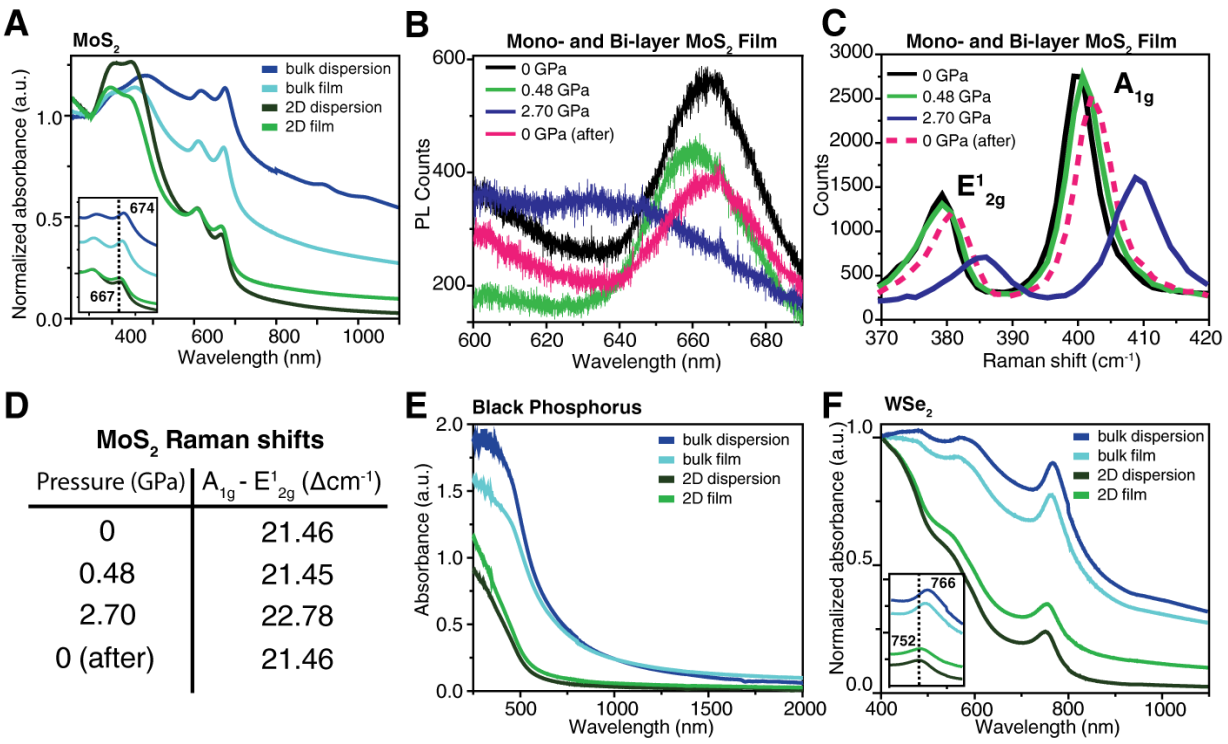

Figure 4-4. Quantum confinement of 2D material films. (A) Absorbance spectra of bulk-like and 2D MoS_2 dispersions and corresponding films. Inset: blue-shift of exciton A with decrease in flake thickness. **(B–C)** Photoluminescence (B) and Raman shifts (C) of monolayer MoS_2 films as a function of unilateral pressure. **(D)** Peak frequency difference as a function of pressure for the Raman spectra in (C). **(E), (F)** Absorbance spectra of bulk-like and 2D Black Phosphorus (E) and WSe_2 (F) dispersions and corresponding films. Inset (F): blue-shift of exciton with decrease in flake thickness demonstrates retention of quantum confinement.

Based on this new understanding of the quantum confinement of MoS_2 flakes deposited as films, we wondered whether we could extend our findings to films of other 2D materials. To test this, we deposited films of bulk and 2D black phosphorus (Figure 4E) and tungsten diselenide (Figure 4F) and measured the absorbance spectra of the dispersions and films. In each case, the dispersions and films of the 2D flakes are both blue-shifted as compared to the bulk-like flakes, indicating the retention of the quantum confined properties of the 2D building blocks.

Our successful demonstration that films of 2D materials can be designed to retain their quantum confined properties while remaining electronically coupled provides a new strategy for

the design of 3D materials whose properties can be tuned based on the underlying building blocks. This would allow the creation of 3D materials with arbitrary combinations of absorption, conductivity, metallic, and insulating characteristics and will advance development, not only for semiconductors but other 2D materials and their mixtures.

REFERENCES

1. Ahn, S. I.; Kim, K.; Jung, J.; Choi, K. C., Large and pristine films of reduced graphene oxide. *Sci Rep* **2015,** *5*, 18799.

2. Benito, J.; Fenero, M.; Sorribas, S.; Zornoza, B.; Msayib, K. J.; McKeown, N. B.; Téllez, C.; Coronas, J.; Gascón, I., Fabrication of ultrathin films containing the metal organic framework Fe-MIL-88B-NH2 by the Langmuir–Blodgett technique. *Colloids and Surfaces A: Physicochemical and Engineering Aspects* **2015,** *470*, 161-170.

3. Nie, H. L.; Dou, X.; Tang, Z.; Jang, H. D.; Huang, J., High-Yield Spreading of Water-Miscible Solvents on Water for Langmuir-Blodgett Assembly. *J Am Chem Soc* **2015,** *137* (33), 10683-8.

4. Yang, T.; Yang, J.; Shi, L.; Mäder, E.; Zheng, Q., Highly flexible transparent conductive graphene/single-walled carbon nanotube nanocomposite films produced by Langmuir–Blodgett assembly. *RSC Adv.* **2015,** *5* (30), 23650-23657.

5. Kaur, H.; Yadav, S.; Srivastava, A. K.; Singh, N.; Schneider, J. J.; Sinha, O. P.; Agrawal, V. V.; Srivastava, R., Large Area Fabrication of Semiconducting Phosphorene by Langmuir-Blodgett Assembly. *Sci Rep* **2016,** *6*, 34095.

6. Tomašević-Ilić, T.; Pešić, J.; Milošević, I.; Vujin, J.; Matković, A.; Spasenović, M.; Gajić, R., Transparent and conductive films from liquid phase exfoliated graphene. *Optical and Quantum Electronics* **2016,** *48* (6).

7. Zhang, H.; Jeon, K. W.; Seo, D. K., Equipment-Free Deposition of Graphene-Based Molybdenum Oxide Nanohybrid Langmuir-Blodgett Films for Flexible Electrochromic Panel Application. *ACS Appl Mater Interfaces* **2016,** *8* (33), 21539-44.

8. Silverberg, G. J.; McClelland, A. A.; Griesse-Nascimento, S.; Girabawe, C.; Kadow, J. P.; Mahadevan, L.; Vecitis, C. D., Controlling the Roughness of Langmuir-Blodgett Monolayers. *J Phys Chem B* **2017,** *121* (19), 5078-5085.

9. Zhang, Y.; Xu, L.; Walker, W. R.; Tittle, C. M.; Backhouse, C. J.; Pope, M. A., Langmuir films and uniform, large area, transparent coatings of chemically exfoliated MoS2 single layers. *J. Mater. Chem. C{Zhang, 2017 #1747}* **2017**.

10. Ariga, K.; Yamauchi, Y.; Mori, T.; Hill, J. P., 25th anniversary article: what can be done with the Langmuir-Blodgett method? Recent developments and its critical role in materials science. *Adv Mater* **2013,** *25* (45), 6477-512.

11. Li, X.; Zhang, G.; Bai, X.; Sun, X.; Wang, X.; Wang, E.; Dai, H., Highly conducting graphene sheets and Langmuir-Blodgett films. *Nat Nanotechnol* **2008,** *3* (9), 538-42.

12. Zhu, Y.; Cai, W.; Piner, R. D.; Velamakanni, A.; Ruoff, R. S., Transparent self-assembled films of reduced graphene oxide platelets. *Applied Physics Letters* **2009,** *95* (10), 103104.

13. Zheng, Q.; Ip, W. H.; Lin, X.; Yousefi, N.; Yeung, K. K.; Li, Z.; Kim, J.-K., Transparent conductive films consisting of ultralarge graphene sheets produced by Langmuir-Blodgett Assembly. *ACS Nano* **2011,** *5* (7), 6039-6051.

14. Zheng, Q.-b.; Shi, L.-f.; Yang, J.-h., Langmuir-Blodgett assembly of ultra-large graphene oxide films for transparent electrodes. *Transactions of Nonferrous Metals Society of China* **2012,** *22* (10), 2504-2511.

15. Eda, G.; Yamaguchi, H.; Voiry, D.; Fujita, T.; Chen, M.; Chhowalla, M., Photoluminescence from chemically exfoliated MoS2. *Nano letters* **2011,** *11* (12), 5111-5116.

16. Taguchi, Y.; Kimura, R.; Azumi, R.; Tachibana, H.; Koshizaki, N.; Shimomura, M.; Momozawa, N.; Sakai, H.; Abe, M.; Matsumoto, M., Fabrication of hybrid layered films of MoS2 and an amphiphilic ammonium cation using the Langmuir− Blodgett technique. *Langmuir* **1998,** *14* (22), 6550-6555.

17. Kelly, A. G.; Hallam, T.; Backes, C.; Harvey, A.; Esmaeily, A. S.; Godwin, I.; Coelho, J.; Nicolosi, V.; Lauth, J.; Kulkarni, A.; Kinge, S.; Siebbeles, L. D. A.; Duesberg, G. S.; Coleman, J. N., All-printed thin-film transistors from networks of liquid-exfoliated nanosheets. *Science* **2017,** *356* (6333), 69.

18. Akatsuka, K.; Haga, M.-a.; Ebina, Y.; Osada, M.; Fukuda, K.; Sasaki, T., Construction of highly ordered lamellar nanostructures through Langmuir-Blodgett deposition of molecularly thin titania nanosheets tens of micrometers wide and their excellent dielectric properties. *ACS Nano* **2009,** *3* (5), 1097-1106.

19. Muramatsu, M.; Akatsuka, K.; Ebina, Y.; Wang, K.; Sasaki, T.; Ishida, T.; Miyake, K.; Haga, M.-a., Fabrication of Densely Packed Titania Nanosheet Films on Solid Surface by

Use of Langmuir− Blodgett Deposition Method without Amphiphilic Additives. *Langmuir* **2005,** *21* (14), 6590-6595.

20. El-Mahalawy, S.; Evans, B., Pressure dependence of the electrical conductivity in 2H-MoS2 and 2H-WSe2. *physica status solidi (b)* **1978,** *86* (1), 151-157.

21. Afsar-Siddiqui, A. B.; Luckham, P. F.; Matar, O. K., The spreading of surfactant solutions on thin liquid films. *Advances in Colloid and Interface Science* **2003,** *106* (1-3), 183-236.

22. von Bahr, M.; Tiberg, F.; Zhmud, B. V., Spreading dynamics of surfactant solutions. *Langmuir* **1999,** *15* (20), 7069-7075.

23. Dussaud, A. D.; Troian, S. M., Dynamics of spontaneous spreading with evaporation on a deep fluid layer. *Physics of Fluids* **1998,** *10* (1), 23-38.

24. Liu, K.; Zhang, L.; Cao, T.; Jin, C.; Qiu, D.; Zhou, Q.; Zettl, A.; Yang, P.; Louie, S. G.; Wang, F., Evolution of interlayer coupling in twisted molybdenum disulfide bilayers. *Nature communications* **2014,** *5*, 4966.

25. Huang, S.; Ling, X.; Liang, L.; Kong, J.; Terrones, H.; Meunier, V.; Dresselhaus, M. S., Probing the interlayer coupling of twisted bilayer MoS2 using photoluminescence spectroscopy. *Nano letters* **2014,** *14* (10), 5500-5508.

26. Castellanos-Gomez, A.; van der Zant, H. S.; Steele, G. A., Folded MoS 2 layers with reduced interlayer coupling. *Nano Research* **2014,** *7* (4), 572-578.

27. Coleman, J. N.; Lotya, M.; O'Neill, A.; Bergin, S. D.; King, P. J.; Khan, U.; Young, K.; Gaucher, A.; De, S.; Smith, R. J.; Shvets, I. V.; Arora, S. K.; Stanton, G.; Kim, H. Y.; Lee, K.; Kim, G. T.; Duesberg, G. S.; Hallam, T.; Boland, J. J.; Wang, J. J.; Donegan, J. F.; Grunlan, J. C.; Moriarty, G.; Shmeliov, A.; Nicholls, R. J.; Perkins, J. M.; Grieveson, E. M.; Theuwissen, K.; McComb, D. W.; Nellist, P. D.; Nicolosi, V., Two-dimensional nanosheets produced by liquid exfoliation of layered materials. *Science* **2011,** *331* (6017), 568-71.

28. Eda, G.; Yamaguchi, H.; Voiry, D.; Fujita, T.; Chen, M.; Chhowalla, M., Photoluminescence from chemically exfoliated MoS_2. *Nano Letters* **2011,** *11* (12), 5111-6.

29. Mak, K. F.; Lee, C.; Hone, J.; Shan, J.; Heinz, T. F., Atomically thin MoS 2: a new direct-gap semiconductor. *Physical review letters* **2010,** *105* (13), 136805.

30. Paul, W.; Warschauer, D. M., *Solids under pressure*. McGraw-Hill: New York, 1963.

31. Holzapfiel, W. B.; Isaacs, N. S., *High pressure techniques in chemistry and physics: a practical approach*. Oxford University Press: Oxford; New York, 1997.

32. Ferraro, J. R., *Vibrational spectroscopy at high external pressures: the diamond anvil cell*. Academic Press: New York, 1984.

33. Hazen, R. M.; Finger, L. W., *Comparative crystal chemistry: temperature, pressure, composition, and the variation of crystal structure*. Wiley: Chichester; New York, 1982.

34. Sherman, W. F.; Stadtmuller, A. A., *Experimental techniques in high-pressure research research*. Wiley: Chichester; New York, 1987.

35. Tsiklis, D. S., *Handbook of techniques in high-pressure research and engineering*. Plenum Press: New York, 1968.

36. MacDonald, W., Diamond anvil, preparing the gasket. YouTube: https://youtu.be/XxIGoJ-fJro, 2015.

CHAPTER FIVE – BEYOND VAN DER WAALS FORCES: MASSIVE CHARGE TRANSFER AND QUASI-BOND FORMATION IN COULOMBIC HETEROSTRUCTURES

*Adam H. Woomer[1], Daniel L. Druffel[1], Jack D. Sundberg[1], Scott C. Warren[1,2]**

[1]Department of Chemistry and [2]Department of Applied Physical Sciences, University of North Carolina at Chapel Hill, Chapel Hill, North Carolina 27599, USA. *sw@unc.edu

5.1 Introduction

Nearly every material property, from color to conductivity to chemical reactivity, is influenced by the distance between atoms. As atoms approach, orbitals overlap, bonds form, and wavefunctions delocalize. Even in materials where interatomic distances are difficult to change, many theoretical approaches—Pauling's bond orders and resonance[1], Mulliken's overlap populations[2], or Hückel and Hoffmann's linear combination of atomic orbitals[3-4]—guide understanding and motivate the search for improved control. One such material system for which control of interatomic distances has been elusive are stacks of 2D materials, often called van der Waals heterostructures[5]. These heterostructures have attracted intense study because 2D materials can be assembled in virtually any sequence, encoding functions into the stack one 2D layer at a time. Adjacent layers are usually separated by 3 to 4 Å—a distance 1 to 2 Å longer than covalent or ionic bonds—and therefore the dispersion force, a type of van der Waals force, is the primary interaction between layers. As such, 2D heterostructures with reduced interlayer distances, strong interlayer interactions, and radically different properties, have been rarely explored.

Here we explore a strategy to reduce the distance between 2D materials by creating heterostructures with strong Coulombic attractions between layers. When two neutrally charged 2D materials are stacked, electrons transfer between layers to equilibrate the Fermi level. This results in one layer with net positive charge and one layer with net negative charge, which, in principle, could provide an electrostatic attractive force that could reduce the interlayer distance. In 2D materials explored so far, however, it has not been possible to reduce the interlayer distance. For example, in heterostructures that seem well-suited for charge transfer, such as those made from n-type MoS_2 and p-type WSe_2, the amount of charge transfer is, in fact, less than 0.01 electron per atom of MoS_2[6]. This amount of charge transfer is insufficient to achieve a measurable reduction in interlayer distance[7]. Recently, however, we introduced a new class of 2D materials, called electrenes[8-9], that may be poised to address this challenge. Electrenes are electron-rich 2D materials that are derived from electrides, a type of ionic solid in which the lattice sites that would ordinarily hold an anion instead holds just a bare electron[10-20]. In layered electrides, the electrons lie in planes, and the process of exfoliation exposes these electrons on the surface (Figure 1b). It has recently been shown experimentally[21] and computationally[22-23] that these surface-exposed electrons can be donated to adjacent 2D materials. For example, in the case of a 30-nm thick electride flake next to MoTe2, 0.11 electrons per atom were transferred to $MoTe_2$[21]. The potential use of electrenes as an electron donor to form bonds between 2D materials is, however, entirely unexplored.

To provide insight into the proposed electrene-2D heterostructures, we consider an analogous process: the electron transfer reaction that occurs when metallic sodium reacts with chlorine gas to yield insulating table salt. Although this example is familiar, it demonstrates the ways in which structure and properties can be radically transformed by electron transfer. Thus,

by using an electrene to donate electrons to other 2D materials, Coulombic forces will attract each layer together, yielding a heterostructure that may have radically different properties. To distinguish this class of layered solids from van der Waals (vdW) heterostructures, we introduce the name Coulombic heterostructures.

5.2 Interlayer Distance and Charge Transfer in Coulombic Heterostructures

We calculate from first principles (see Section 2.5.1 for full details) the structure of common layered materials, the layered electrides, and Coulombic heterostructures. We show a qualitative representation of our result for a graphene/electrene heterostructure in Figure 5-1. As expected for van der Waals forces, the interlayer distance of bilayer graphene is 3.4 Å (Figure 5-1a). The layered electrides have formula unit M_2N (M: Ca, Sr, Ba) or M_2C (M: Y, Gd) and have a much larger interlayer distances (average: 3.8 Å) that are occupied by an anionic 2D electron gas (Figure 1b). When assembled as a heterostructure, we find a decrease in interlayer distance to 2.7 Å and the loss of the electron gas at the interface of the heterostructure. This distance is *ca*. 1.0 Å less than a typical van der Waals interaction, yet 1.0 Å larger than covalent and ionic bond distances. Given the charge transferred from electride to 2DM and the atypical interlayer (as well as interatomic) distances, this raises questions about the nature of interlayer bonding in these materials.

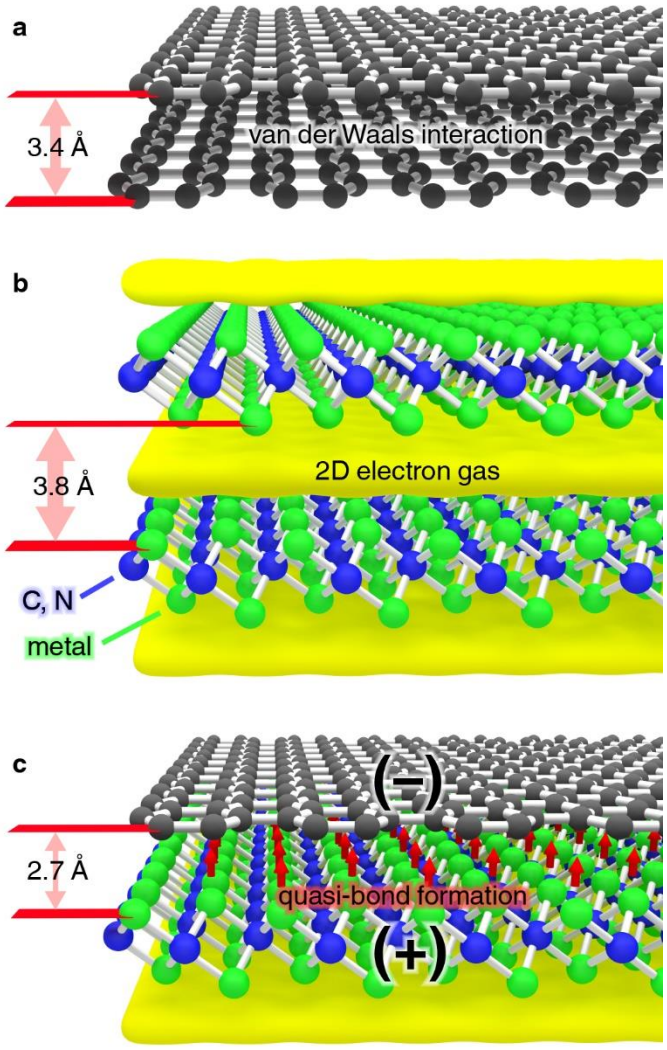

Figure 5-1. Achieving high degrees of charge transfer by combining 2D electrenes with other 2D materials: (A) Bilayer graphene with interlayer distance *ca.* 3.4 Å **(B)** Bilayer electrides with structure M_2N (M: Ca, Sr, or Ba) or M_2C (M: Y, Gd). **(C)** A 2DM/Electrene heterostrcture with interlayer distance of 2.7 Å and donation of the electron gas into the 2DM.

One instructive method to classify bonding is to plot the covalent, ionic, metallic, and van der Waals character of a compound with a bonding tetrahedron (Figure 5-2A). Here, we focus on the covalent-ionic-van der Waals triangle (Figure 5-2B), as these parameters can be readily quantified in electrene heterostructures. In our plot, we quantify the covalent-to-ionic (left-to-right) direction based on the degree of charge transfer between donor and acceptor atoms in the material, as calculated by a Bader integration of electron density. For example, the C-C bond of

diamond has no net electron transfer between atoms, so the compound lies on the left side of the plot, while in NaCl, 0.83 e^- are transferred from Na to Cl, so it appears on the right side. The extent of van der Waals character is calculated by dividing the observed bond distance by the van der Waals distance. For example, the B-N bond length in borane-ammonia (H_3B-NH_3) is 47% of the van der Waals radii of B + N, while the distance between C atoms is adjacent layers of graphite is exactly 100% of the van der Waals distance.

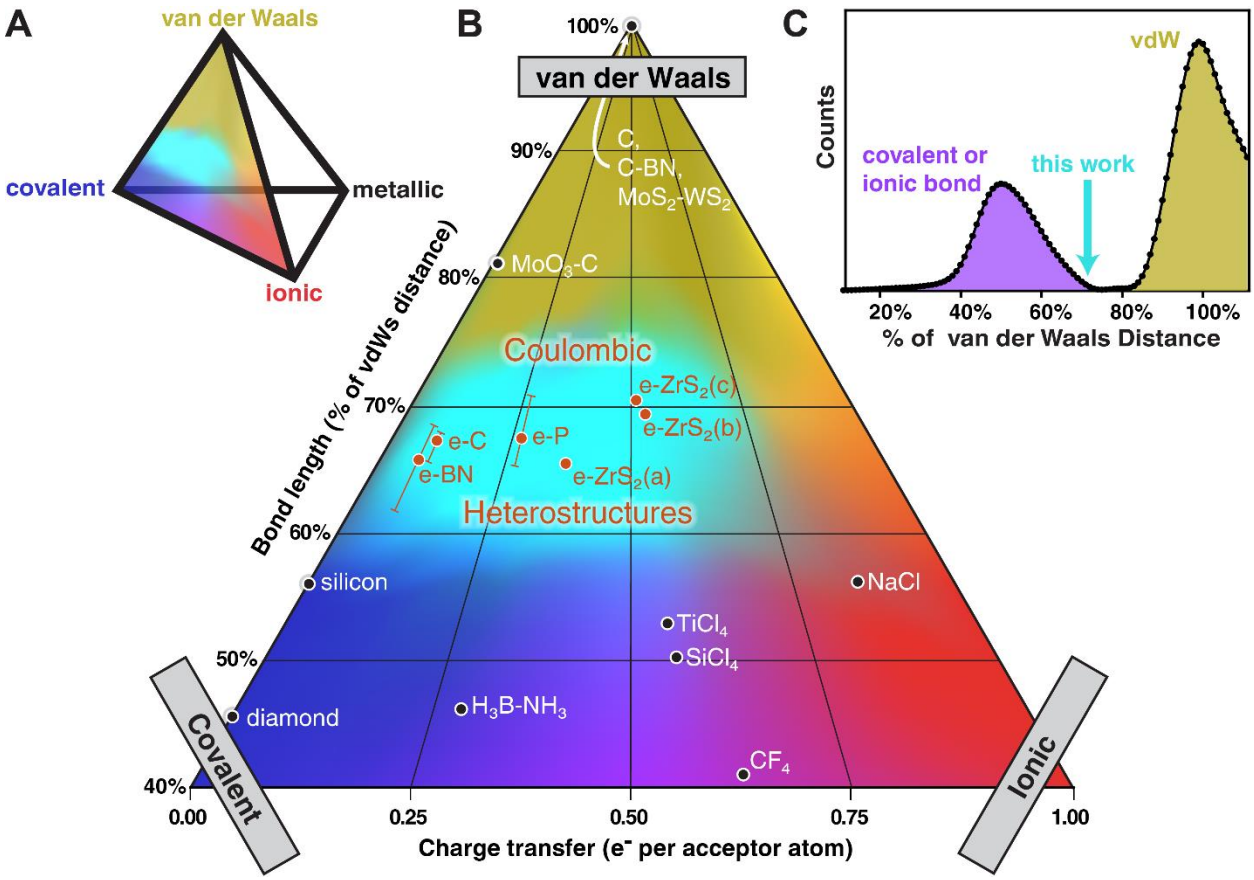

Figure 5-2. Bonding and charge transfer in Molecular compounds, van der Waals materials, and Coulombic heterostructures: (A) A traditional representation of bonding types including vdW, ionic, covalent, and metallic. **(B)** Bonding interactions between van der Waals, covalent, and ionic compounds as described by bond length (% of vdWs distance) and charge transfer per acceptor atom. **(C)** Examination of the prevalence of bond length is a subset of crystals from the Materials Project. Peaks represent covalent or ionic interactions (purple) or vdW interactions (yellow).

In the above example of a electrene-graphene (e-C) heterostructure, the interlayer distance of 2.7 Å corresponded to a bond length of 68%. A Bader analysis determined that, on average, 0.12 e^- was transferred per acceptor atom (in this case, graphene is the acceptor). To explore whether other Coulombic heterostructures were similarly unusual, we examined three other compositions: Sr_2N and hBN (e-BN), Ca_2N and black phosphorus (e-BP) and Ca_2N and ZrS_2 (e-ZrS_2). In general, we find that Coulombic heterostructures have 0.1 e^- to 0.5 e^- transferred per acceptor atom with distances approximately 65 to 70% of the sum of their vdW radii. To show that these bond lengths are distinctive, we quantified bond distances in a subset of compounds from the Materials Project[24] and plotted nearest-neighbor bond distances and van der Waals distances (Figure 5-2C). The analysis shows that covalent and ionic bonds fall largely between 40 and 65%, while van der Waals interactions are usually >85%. The region between 65 and 85% has been called the van der Waals gap—a range of interatomic distances where bonding is rarely observed. The observation of bond distances between 65 and 70% therefore indicates that Coulombic heterostructures have a distinctive type of bonding that has been largely unexplored. In general, we find that these bond distances are about 1 Å longer than ordinary covalent or ionic bonds and about 1 Å shorter than van der Waals interactions.

5.3 Binding Energy and Orbital Projections in Coulombic Heterostrucutres

To visualize the charge transfer in a Coulombic Heterostructures, we use orbital projections and electron density deformation. In Figure 5-3A and 5-3B, we plot the orbital projection of the electronic states within thermal energy (kT) of the Fermi level. The conduction bands of graphene are composed of p_z orbitals, while that of Sr_2N is a 2D electron gas with some orbital mixing with Sr *d* and N *p* states. When the two materials are assembled as a

heterostructure (Figure 3C) there is loss of the electronic states for the 2D electron gas at the interface and an increase in electron density for the C p_z orbitals. The band structure of e-C shows that the Dirac cone of graphene remains largely unperturbed, with a large upward shift of the Fermi level of 1.4 eV (see supporting information). While these orbital projections give a qualitative depiction of the charge transfer, they cannot be directly compared due to the changes in the Fermi level. Because the optimized structure is relatively unchanged compared to the individual components, we instead calculate the electron density deformation, n_{edd}, of e-C as:

$$n_{edd} = n_{e-C} - (n_{graphene} + n_{Sr_2N}) \quad (5.1)$$

where $n_{e\text{-}C}$ is the total electron density for the heterostructure, $n_{graphene}$ is the electron density of graphene in the e-C supercell without Sr_2N and n_{Sr2N} is the electron density of Sr_2N in the e-C supercell without graphene. We find that the assembly of an e-C heterostructure has no effect on the 2D electron gas on the surface of Sr_2N, a loss of electron density at the interface, and a gain in electron density into p_z shaped regions on the graphene sheet.

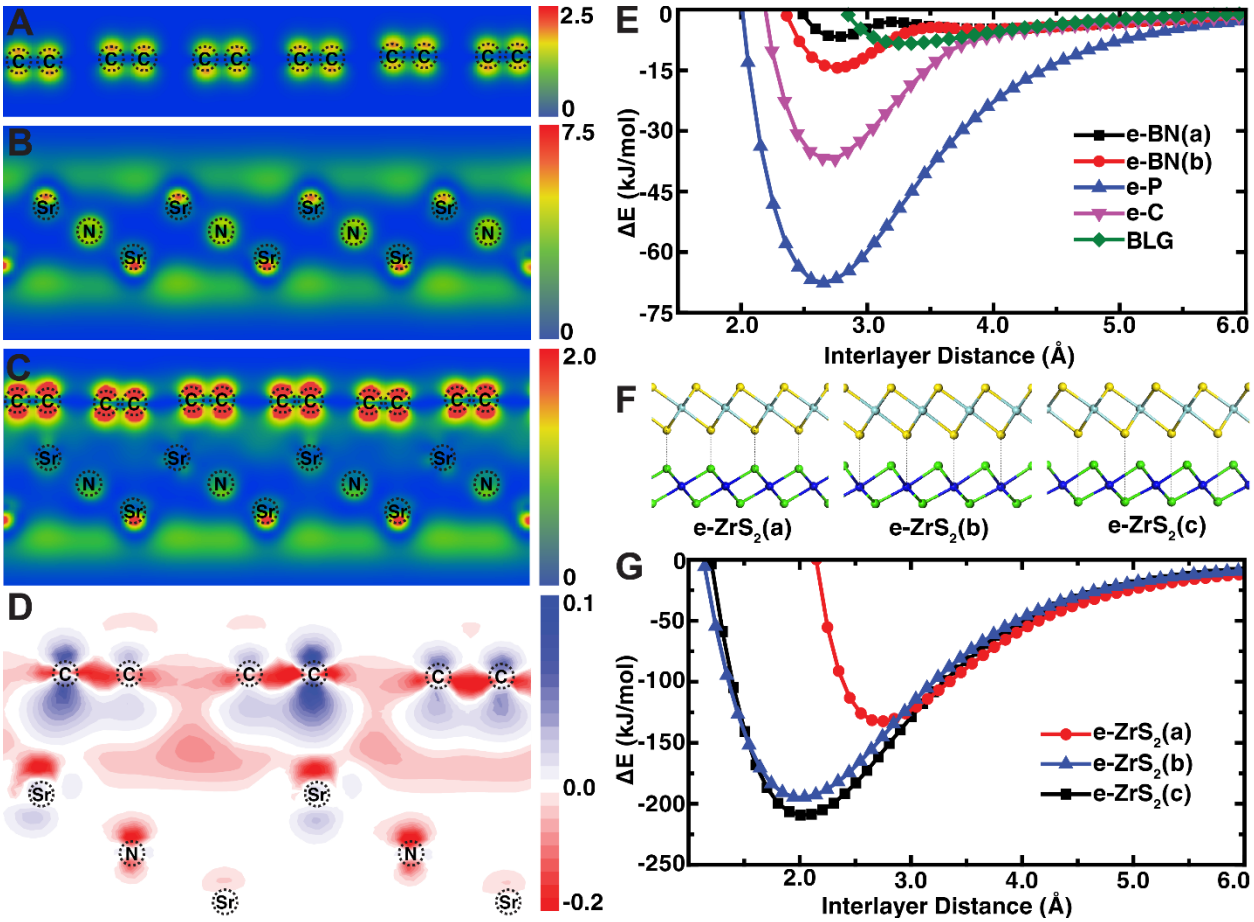

Figure 5-3: Orbital projections, electron density, and interlayer interaction energies in Coulombic heterostructures: Orbital projection of the electronic states within thermal energy of the Fermi level for (**A**) graphene, (**B**) Sr_2N, and **(C)** the e-C heterostructure. **(D)** Electron density deformation in the e-C, showing a loss of electron density (red) in the interlayer region and a gain of electron density (blue) to graphene p_z orbitals. **(E)** Interlayer binding energies for Coulombic heterostructures and bilayer graphene (green). **(F)** Three structural orientations for e-ZrS_2. **(G)** Interlayer binding energies for the e-ZrS_2 structures in (F).

Given the charge transfer and small interlayer distance, we expect an increased interlayer interaction for Coulombic heterostructures. We calculate an interlayer binding energy, E_{BE}, with Equation 5.2 for various Coulombic heterostructures and bilayer graphene:

$$E_{BE} = \frac{(E_{ild} - E_{\infty})}{n_{inter}} \qquad (5.2)$$

where E_{ild} is the total energy of the heterostructure at a given interlayer distance and E_{∞} is the total energy of the heterostructure with a 12.0 Å separation, and n_{inter} is the number of atoms at

the interface. Treating the 2D material as the adsorbed species, the interaction energy per interfacial atom of 2DM is similar to weak chemisorption, *ca.* 40.0 kj/mol (Figure 5-3E). We note the interaction energy for two orientations of e-BN is significantly lower compared to other Coulombic heterostructures. Given the position of the hBN conduction band relative to the Fermi level of electrenes, we expect that this is due to an activation energy for charge transfer. While the other heterostructures have a strong chemisorptive interaction that dominates the potential energy curve, e-BN(a) and e-BN(b) (Figure 5-3E, red and black) have a competing metastable phase at *ca*. 4.0 Å. Interestingly, this metastable phase is equivalent to the sum of van der Waals radii of hBN and the distance the electron gas extends out from an electron monolayer, and we therefore conclude that this phase is the physisorption of hBN to an electrene. For comparison, we plot the interlayer interaction of bilayer graphene (Figure 3E, green). With no favorable interactions at distances smaller than the van der Waals distance of 3.4 Å, the potential energy curve is entirely physisorptive in character.

The e-ZrS_2 heterostructures are an interesting example of the influence of crystal symmetry and lattice matching. We examined three orientations for this heterostructure (Figure 3F) in which the lattices are eclipsed (e-ZrS_2(a)) or staggered with the sulfur atom occupying the octahedral site in which the electron gas has the highest electron density (e-ZrS_2(b) and e-ZrS_2(c)). In the energy evolution of e-ZrS_2(a) with distance (Figure 3G, red) we can see the influence of Pauli exclusion: Ca and S atoms are directly aligned such that the repulsion of the atomic nuclei results in a larger interlayer distance of 2.75 Å and a charge transfer to ZrS_2 of 0.37 e- per formula unit of electrene. When there is a better lattice matching between ZrS_2 and the electrene, as seen in e-ZrS_2(b) and e-ZrS_2(c), these heterostructures exhibit increased charge transfer and smaller distances of *ca* 0.50 e- per formula unit of electrene and 2.0 Å, respectively.

With the largest charge transfer and smallest interlayer distances of the Coulombic heterostructures, we observe the strongest interlayer binding energies for these systems (Figure 5-3G). From these calculations of E_{BE}, we conclude that Coulombic heterostructures can be quantitatively distinguished from the van der Waals heterostructures and materials larger interaction energies and smaller interlayer distances.

5.4 Quasi-bonding interactions in Coulombic Heterostructures

We further investigate the quasi-bonding in Coulombic heterostructures using electron density difference *vs* atomic orbitals (Figure 5-4). Electron density difference (EDD) can be used to depict the perturbation (or lack thereof) of atomic orbitals as a result of bonding interactions, however, they often depend on a careful analysis coupled with chemical intuition to draw quantitative conclusions on the system. Here we use electron density difference to qualitatively investigate the perturbation of atomic orbitals within the interlayer space of Coulombic heterostructures and compare them to simple covalent, ionic, and van der Waals systems.

We start by investigating the EDD of the vertices of the vdW, covalent, and ionic bonding triangle (Figure 5-4A). For a MoS_2 and WS_2 vdW heterostructure, we find no positive or negative shifts of electron density across the interface (Figure 5-4B), as is expected for weak van der Waals with a negligible degree of charge transfer. At the covalent vertex of the binding triangle, a H_2 molecule has a positive shift in electron density towards the internuclear space of hydrogen atoms (Figure 5-4F). Given the simplicity of this particular system, the EDD takes on the shape of the highest occupied molecular orbital. Similarly, the EDD of NaCl is easily interpreted: because of the charge transfer from Na to Cl, positive (negative) shifts in electron density with spherical shape surround each Cl (Na) atom (Figure 5-4H).

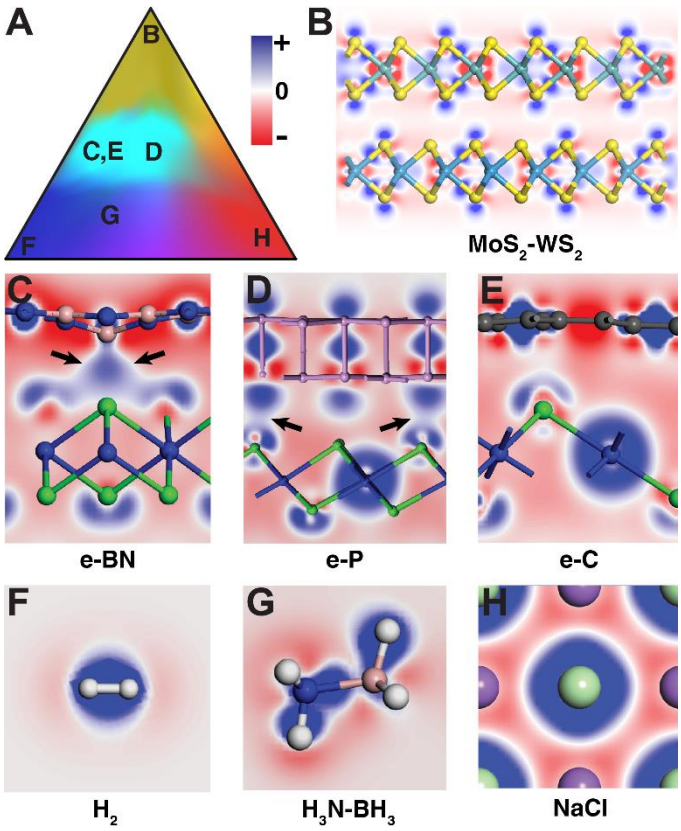

Figure 5-4. Electron Density Difference of Different Bonding for Coulombic Heterostructures and vdW, Ionic, and Covalent compounds: **(A)** The vdW, Ionic, and Covalent bonding triangle from Figure 5-2B. Letters within triangle place the following figure components on the bonding triangle with regard to bonding type: **(B)** MoS_2-WS_2 heterostructure **(C)** e-BN **(D)** e-P **(E)** e-C **(F)** H_2 **(G)** NH_3-BH_3 **(H)** NaCl.

The EDD of e-C (Figure 5-4E) shows little to no change in electron density across the interlayer space, in a manner like the MoS_2/WS_2 vdW heterostructure. Given this result, as well as the charge transfer, interlayer distance, interaction energy, and band structure of e-C, we conclude the interaction between graphene and electrenes is analogous to defect-free doping: the charge transfer of the electron gas will dope graphene n-type and is accompanied by strong electrostatic interactions between the negatively charged graphene and positively charge metal ions on the surface of the electrene. Interestingly, the EDD of e-BP (Figure 5-4D) and e-BN(b) (Figure 5-4C) do show a positive shift in electron density *vs* atomic orbitals into the interlayer

space, implying a profound change in the chemical nature and electronic structure of these materials.

Of the Coulombic heterostructures, e-BN is perhaps the most interesting from the perspective of quasi-bonding interactions. With over a 2.0 eV difference between the Fermi level of Sr_2N and the conduction band of hBN, it was unexpected that there would be charge transfer of the electron gas to the 2DM. Furthermore, as mentioned previously in section 5-3, e-BN is the only heterostructure that shows a competitive physisorption phase, in which no charge is transferred. To understand why this favorable quasi-bonding occurs for e-BN, we turn to an analogous molecular system: the donor-acceptor adduct NH_3-BH_3 (Figure 5-5). In this system,

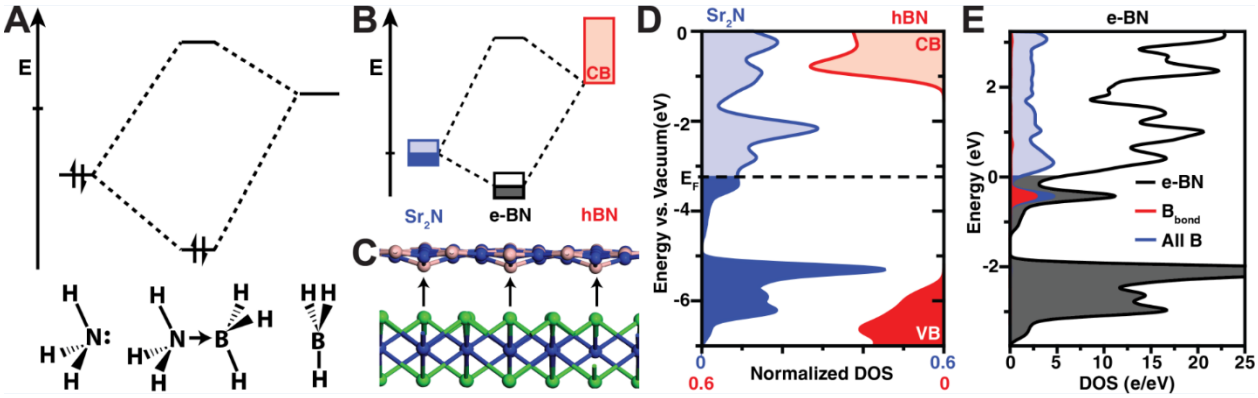

Figure 5-5. Donor-acceptor analogy to rationalize charge transfer in hBN case: (A) Molecular orbital diagram of NH_3-BH_3 **(B)** Molecular orbital diagram of Sr_2N (blue), hBN (red), and e-BN (black) suggesting the creation of a quasi-bonding state **(C)** Supercell of e-BN(b), showing the displacement of boron atoms into the interlayer space. Arrows depict the charge transfer of the electron gas and formation of a donor-acceptor adduct. **(D)** Density of states (DOS) of Sr_2N (blue) and hBN (red) relative to one another and **(E)** The DOS and of e-BN (black) and partial DOS for displaced B atoms (red) and all B atoms (blue)

two electrons from the highest occupied molecular orbital of NH_3, the lone electron pair on nitrogen, are donated to the lowest unoccupied molecular orbital of BH_3, the B *p* orbital, and form a new bonding orbital (Figure 5-5A). The BH_3 molecule will change from trigonal planar to

tetrahedral to accommodate the increased electron density around boron from the new bonding state.

We hypothesize that the quasi-bonding in e-BN proceeds *via* a similar mechanism (Figure 5-5B). The conduction band of hBN is composed of B p_z oribtals such that when it is adjacent to an appropriate donor material, a new donor-acceptor state can be formed. We observe structural similarities between e-BN and NH_3-BH_3; there is a periodic displacement of boron atoms towards the electrene such that they assume a tetrahedral bonding configuration (Figure 5-5C). Furthermore, we find evidence for the formation of a new donor-acceptor state in the electronic structure of e-BN. First, we calculate the electronic structure of Sr_2N and hBN in the same supercell with a 12 Å vacuum space. We find that the band structure of this system is the superposition of a monolayer Sr_2N and hBN (see supporting information). The Fermi level resides within the electron gas band of Sr_2N and there is a *ca*. 2.0 eV difference between the conduction band states of hBN and the electron gas band of Sr_2N (Figure 5-5D). When assembled as e-BN, we find the formation of a new electronic state at -0.5 eV relative to the Fermi level (Figure 5-5E). From the partial density of states of e-BN, we find that this state is comprised of the previously unfilled boron orbitals, 66% of which is originating from the displaced boron atoms (Figure 5-5E red). We conclude that the charge transfer from electrene to hBN is favorable upon the formation of a donor-acceptor state with the unfilled $\underline{p_z}$ orbitals of boron. This type of interaction between layered materials has never been seen before for stacked 2DM or van der Waals heterostructures and is a feature exclusive to Coulombic heterostructures.

5.5 Unexpected properties of Coulombic Heterostructures

We now highlight some of the most interesting properties and applications that result from Coulombic heterostructures. The already low work function of electrenes can be further decreased by the donation of electron density to the 2D material. Because of the accumulation of negative charge, an electric field towards the 2DM is established across the interlayer distance that will decrease the work function of the electride (Figure 5-6A). Compared to the work function of an electrene (Figure 5-6B, dashed blue line), we find that work function can be tuned from 2.6 to 3.5 eV depending on the Coloumbic heterostructure.

We also calculate the potential energy surface for sliding 2DMs and electrenes (Figure 5-6 C-E). It has been previously predicted that the sliding energy of misfit layered compounds is virtually zero because of the charged slabs. Here we find that sliding the energy for Coulombic heterostructures can span three orders of magnitude, from hundreds to just a few meV per supercell. The activation energy for sliding depends on two factors (i) how commensurate the lattice matching is and (ii) the distribution of charge across the surface of the material. For example, e-ZrS_2 has the largest activation energy of 725 meV/supercell for sliding because of the conformity of the ZrS_2 and electride lattice (Figure 5-6C). Lateral translations of the 2DM require a perpendicular displacement to avoid coloumbic repulsion of atomic nuclei. e-BN presents an intermediate case for sliding energies, with a value of 55 meV/supercell. While the hBN is planar, charge is distributed unevenly across the material and is localized on boron atoms to form quasi-bonds (see section 5.4). Finally, we find extremely small activation energies for sliding in e-C, with a maximum value of 6.8 meV/supercell, because of the planar, distributed charged across carbon atoms. Since the quasi-bonding interaction in e-C is primarily electrostatic, it is an ideal candidate for applications requiring superlubricity.

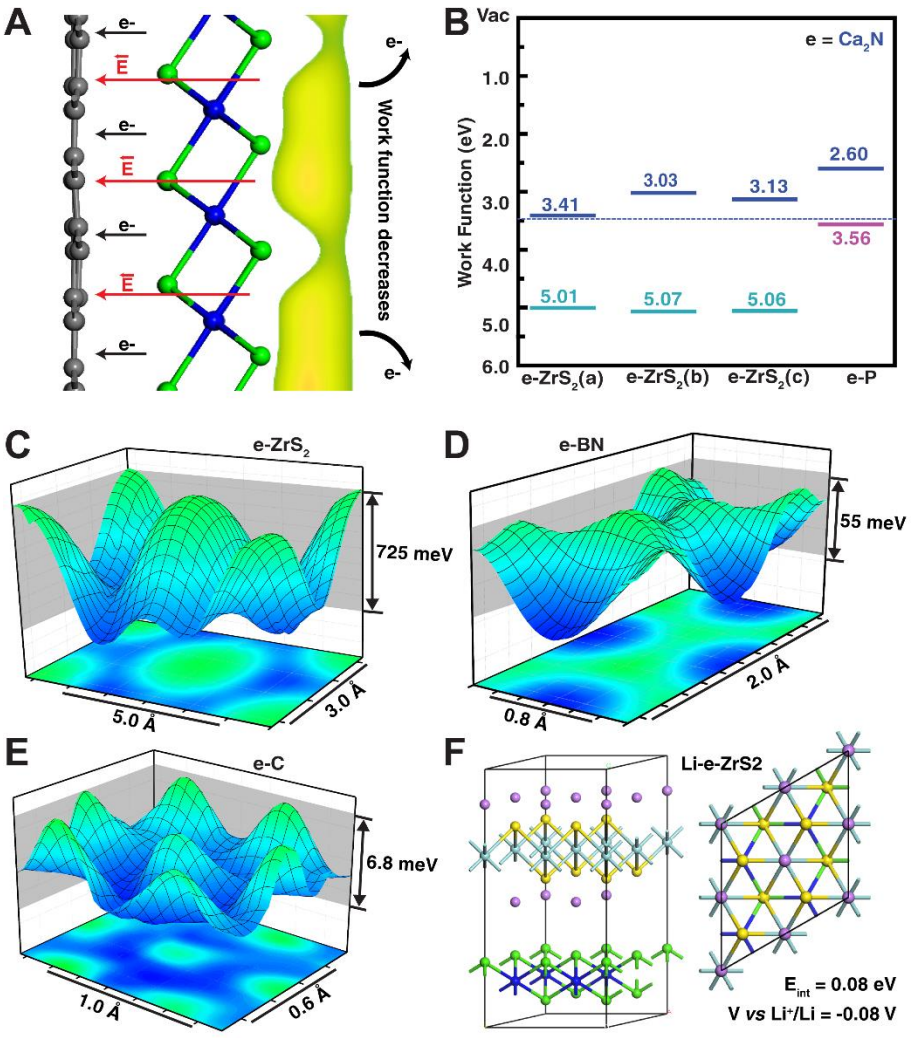

Figure 5-6. Work function tailoring, superlubricity and Li ion intercalation of Coulombic Heterostructures: (**A**) Depiction of electron transfer and the resulting electric field in a Coulombic heterostructure bilayer that leads to the lowering of the work function on both graphene and electrene surfaces. (**B**) Work functions of four Coulombic heterostructures for the electrene (dark blue, lower work function) and adjacent 2D material (higher work function). For reference, the work function of an electrene monolayer is shown as a dashed line. Sliding energies of e-ZrS_2 (**C**), e-BN (**D**), and e-C (**E**). (**F**) Structure of a lithium-intercalated electrene-ZrS_2 heterostructure.

Finally, we investigate the application of Coulombic heterostructures as an electrode in lithium ion batteries. ZrS_2 is known to be extremely favorable for the intercalation of Li, with a voltage of 1.9 V vs Li^+/Li. We calculate the energy for the intercalation, E_{int}, of Li into e-ZrS_2 with the following Equation 5.3:

$$E_{int} = E(Li.eZrS_2) - [E(e.ZrS2) + E(Li)]$$

where E(Li-e-ZrS_2) is the total energy of a periodic e-ZrS2 heterostructure with one equivalent Li atom per formula unit, E(e.ZrS_2) is the total energy of a periodic e-ZrS_2 heterostructure, and E(Li) is the total energy of bcc-Lithium metal. We find that the energy for intercalation is just slightly unfavorable, at a value of +0.08 eV and a corresponding voltage of -0.08 V vs Li^+/Li (Figure 5-6F). This case is an extreme example of tailoring the intercalation voltages of a layered material by almost 2.0 V upon assembly as a Coulombic heterostructures. One can imagine that alternate stacking sequences, selection of 2DM and electrene, or structural modification of the starting materials would afford greater control over intercalation energy for highly designed properties.

5.6 Conclusions

To conclude, we have described a remarkable class of 2D materials in which the interatomic distances can be shifted into a little-explored region. We observe clear evidence for quasi-bond formation between layers: a shift in electron density from electrene to the adjacent 2D material that leads to varying degrees of covalency or ionicity between layers. In this sense, Coulombic heterostructures are the 2D analogue of the donor-acceptor motif that has found great use throughout chemistry, materials science, and physics. The discovery of 2D acceptor-donor materials with quasi-bond formation while, in some cases, also achieving superlubricity, is a remarkable combination of properties. Moreover, these heterostructures have a set of extraordinary properties and may show potential use as electron emitters or in battery electrodes. Given the multitude of possible building blocks that could be used in Coulombic heterostructures, many more unusual properties are likely to be discovered.

REFERENCES

1. Pauling, L., *The nature of the chemical bond : and the structure of molecules and crystals; an introduction to modern structural chemistry*. 3d ed. ed.; Cornell University Press: Ithaca, N.Y., 1960.

2. Mulliken, R. S., Electronic Population Analysis on LCAO–MO Molecular Wave Functions. I. *J. Chem. Phys.* **1955,** *23* (10), 1833-1840.

3. Hückel, E., Zur Quantentheorie der Doppelbindung. *Zeitschrift für Physik* **1930,** *60* (7), 423-456.

4. Hoffmann, R., An Extended Hückel Theory. I. Hydrocarbons. *J. Chem. Phys.* **1963,** *39* (6), 1397-1412.

5. Geim, A. K.; Grigorieva, I. V., Van der Waals heterostructures. *Nature* **2013,** *499* (7459), 419.

6. Fang, H.; Battaglia, C.; Carraro, C.; Nemsak, S.; Ozdol, B.; Kang, J. S.; Bechtel, H. A.; Desai, S. B.; Kronast, F.; Unal, A. A., Strong interlayer coupling in van der Waals heterostructures built from single-layer chalcogenides. *Proceedings of the National Academy of Sciences* **2014,** *111* (17), 6198-6202.

7. Withers, F.; Del Pozo-Zamudio, O.; Mishchenko, A.; Rooney, A.; Gholinia, A.; Watanabe, K.; Taniguchi, T.; Haigh, S.; Geim, A.; Tartakovskii, A., Light-emitting diodes by band-structure engineering in van der Waals heterostructures. *Nature materials* **2015,** *14* (3), 301.

8. Druffel, D. L.; Kuntz, K. L.; Woomer, A. H.; Alcorn, F. M.; Hu, J.; Donley, C. L.; Warren, S. C., Experimental Demonstration of an Electride as a 2D Material. *Journal of the American Chemical Society* **2016,** *138* (49), 16089-16094.

9. Druffel, D. L.; Woomer, A. H.; Kuntz, K. L.; Pawlik, J. T.; Warren, S. C., Electrons on the surface of 2D materials: from layered electrides to 2D electrenes. *Journal of Materials Chemistry C* **2017,** *5* (43), 11196-11213.

10. Kim, S. W.; Shimoyama, T.; Hosono, H., Solvated Electrons in High-Temperature Melts and Glasses of the Room-Temperature Stable Electride [Ca24Al28O64] 4+· 4e−. *Science* **2011,** *333* (6038), 71-74.

11. Lee, K.; Kim, S. W.; Toda, Y.; Matsuishi, S.; Hosono, H., Dicalcium nitride as a two-dimensional electride with an anionic electron layer. *Nature* **2013,** *494* (7437), 336.

12. Matsuishi, S.; Toda, Y.; Miyakawa, M.; Hayashi, K.; Kamiya, T.; Hirano, M.; Tanaka, I.; Hosono, H., High-density electron anions in a nanoporous single crystal:[Ca24Al28O64] 4+(4e-). *Science* **2003,** *301* (5633), 626-629.

13. Zhang, Y.; Xiao, Z.; Kamiya, T.; Hosono, H., Electron confinement in channel spaces for one-dimensional electride. *The journal of physical chemistry letters* **2015,** *6* (24), 4966-4971.

14. Dye, J. L., Recent developments in the synthesis of alkalides and electrides. *The Journal of Physical Chemistry* **1984,** *88* (17), 3842-3846.

15. Dye, J. L.; Yemen, M. R.; DaGue, M. G.; Lehn, J. M., Optical spectra of alkali metal anion and''electride''films. *The Journal of Chemical Physics* **1978,** *68* (4), 1665-1670.

16. Issa, D.; Ellaboudy, A.; Janakiraman, R.; Dye, J. L., Magnetic susceptibilities and electron paramagnetic resonance spectra of a ceside and an electride. *The Journal of Physical Chemistry* **1984,** *88* (17), 3847-3851.

17. Le, L. D.; Issa, D.; Van Eck, B.; Dye, J. L., Preparation of alkalide and electride films by direct vapor deposition. *The Journal of Physical Chemistry* **1982,** *86* (1), 7-9.

18. de Boer, J. H.; Verwey, E. J., Semi-conductors with partially and with completely filled 3d-lattice bands. *Proceedings of the Physical Society* **1937,** *49* (4S), 59.

19. Landau, L. D., Electron motion in crystal lattices. *Phys. Z. Sowjet.* **1933,** *3*, 664.

20. Mott, N. F., The basis of the electron theory of metals, with special reference to the transition metals. *Proceedings of the Physical Society. Section A* **1949,** *62* (7), 416.

21. Kim, S.; Song, S.; Park, J.; Yu, H. S.; Cho, S.; Kim, D.; Baik, J.; Choe, D.-H.; Chang, K. J.; Lee, Y. H., Long-Range Lattice Engineering of MoTe2 by a 2D Electride. *Nano letters* **2017,** *17* (6), 3363-3368.

22. Inoshita, T.; Tsukada, M.; Saito, S.; Hosono, H., Probing a divergent van Hove singularity of graphene with a Ca 2 N support: A layered electride as a solid-state dopant. *Physical Review B* **2017,** *96* (24), 245303.

23. Zhao, S.; Li, Z.; Yang, J., Obtaining two-dimensional electron gas in free space without resorting to electron doping: an electride based design. *Journal of the American Chemical Society* **2014,** *136* (38), 13313-13318.

24. Jain, A.; Ong, S. P.; Hautier, G.; Chen, W.; Richards, W. D.; Dacek, S.; Cholia, S.; Gunter, D.; Skinner, D.; Ceder, G., Commentary: The Materials Project: A materials genome approach to accelerating materials innovation. *Apl Materials* **2013,** *1* (1), 011002.

APPENDIX: SUPPORTING INFORMATION FOR CHAPTER FIVE

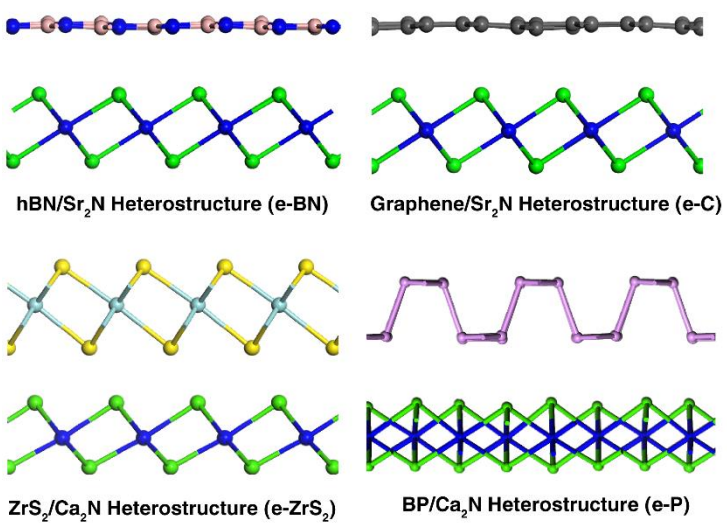

Figure A1-1. Coulombic heterostructures studied by DFT

Table A1-1: Summary of optimized heterostructure lattice constants and interlayer distance.

STRUCTURE	SUPERCELL OF 2DM	SUPERCELL OF ELECTRIDE	LATTICE CONSTANTS (Å)	ILD (Å)
SR_2N/GRAPHENE (E-C)	3x3	2x2	a=b=7.448264	2.754
CA_2N/BLACK PHOSPHORUS (E-BP)	2x2	n/a	a=6.382972 b=9.604992	2.624
SR_2N/BORON NITRIDE (E-BN)	3x3	2x2	a=b=7.56458	2.861
CA_2N/ZRS_2 - A (E-ZRS2A)	1x1	1x1	a=b=3.611331	2.750
CA_2N/ZRS_2 -B (E-ZRS2B)	1x1	1x1	a=b=3.594225	2.044
CA_2N/ZRS_2 -C (E-ZRS2C)	1x1	1x1	a=b=3.601243	2.105

Table A1-2: Bader analysis results for Coulombic Heterostructures

Structure	q_t (e)	q_t/electride formula unit (e)	Interaction energy (kj/mol)
e-C	1.51	0.38	36.96
e-BP	2.13	0.43	135.27
e-BN	1.17	0.29	6.73
e-ZRS2A	0.37	0.37	130.39
e-ZRS2B	0.53	0.53	190.68
e-ZRS2C	0.51	0.51	209.27

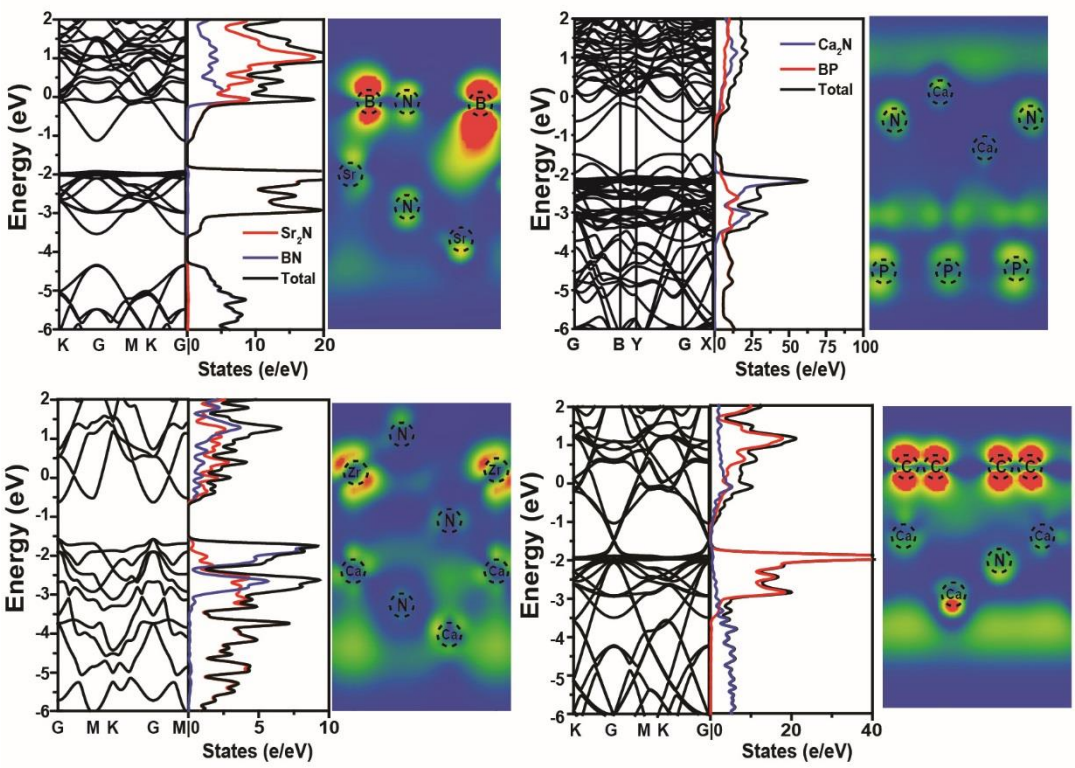

Figure A1-2. Band Structure, DOS, and Orbital projections around Fermi Level for CH: (A) e-BN (B) e-P (C) e-ZrS2 (D) e-C

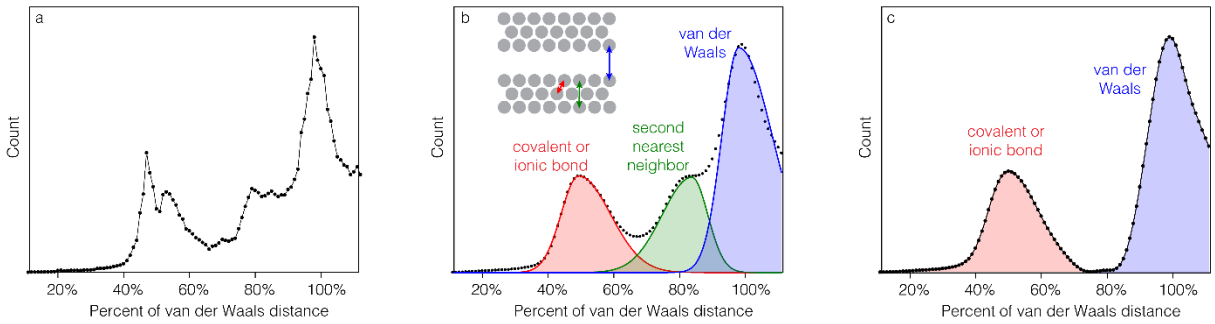

Figure A1-3. Bond length analysis for all crystalline solids: (A) Raw data from the integration of bond lengths for a subset of crystals. **(B)** Smoothed data with Gaussian fit for covalent and ionic bonds (red), artificial "bonds" between second nearest neighbors (green), and van der waals distances (blue). Inset: diagram depicting bond length distances and their assignment. **(C)** Removal of second nearest neighbors